Characterization of Coronary Atherosclerotic Plaques by Dual Energy Computed Tomography

by

Didem Yamak

A Dissertation Presented in Partial Fulfillment
of the Requirements for the Degree
Doctor of Philosophy

Approved April 2013 by the
Graduate Supervisory Committee:

Metin Akay, Co-chair
Jit Muthuswamy, Co-chair
Yasemin Akay
William Pavlicek
Brent Vernon

ARIZONA STATE UNIVERSITY

May 2013

ABSTRACT

Coronary heart disease (CHD) is the most prevalent cause of death worldwide. Atherosclerosis which is the condition of plaque buildup on the inside of the coronary artery wall is the main cause of CHD. Rupture of unstable atherosclerotic coronary plaque is known to be the cause of acute coronary syndrome. The composition of plaque is important for detection of plaque vulnerability. Due to prognostic importance of early stage identification, non-invasive assessment of plaque characterization is necessary. Computed tomography (CT) has emerged as a non-invasive alternative to coronary angiography. Recently, dual energy CT (DECT) coronary angiography has been performed clinically. DECT scanners use two different X-ray energies in order to determine the energy dependency of tissue attenuation values for each voxel. They generate virtual monochromatic energy images, as well as material basis pair images. The characterization of plaque components by DECT is still an active research topic since overlap between the CT attenuations measured in plaque components and contrast material shows that the single mean density might not be an appropriate measure for characterization. This dissertation proposes feature extraction, feature selection and learning strategies for supervised characterization of coronary atherosclerotic plaques. In my first study, I proposed an approach for calcium quantification in contrast-enhanced examinations of the coronary arteries, potentially eliminating the need for an extra non-contrast X-ray acquisition. The ambiguity of separation of calcium from contrast material was solved by using virtual non-contrast images. Additional attenuation data provided by DECT provides valuable information for separation of lipid from fibrous plaque since the change of their attenuation as the energy level changes is different. My second study proposed these as the input to supervised learners for a more precise classification of lipid and fibrous plaques. My last study aimed at automatic segmentation of coronary arteries characterizing plaque components and lumen on contrast enhanced monochromatic X-ray images. This required extraction of features from regions of interests. This study

proposed feature extraction strategies and selection of important ones. The results show that supervised learning on the proposed features provides promising results for automatic characterization of coronary atherosclerotic plaques by DECT.

To my family

ACKNOWLEDGMENTS

I wish to express my sincere gratitude to my adviser Dr. Metin Akay for his support and guidance throughout my study at ASU. Without his guidance, I could not stand as a researcher on my own feet. He also offered me his trust which I could not finish this work without. I thank Dr. Yasemin Akay for her support and kindness. I would like to convey special thanks to Dr. William Pavlicek who gave me the opportunity to work in Mayo Clinic. His guidance in this field contributed to this work a lot. I also thank Thomas Boltz who was there whenever I needed him.

I am deeply indebted to Dr. Vincent Pizziconi who is the most understanding person I have ever met. His kindness and support always gave me the courage to focus on my work. I also thank Nathan Baldwin who is the best person to work with. Teaching capstone could not be any better without him.

I thank my friends Aysegul Demirtas, Kerem Demirtas, Ahmet Cemal Durgun, Pinar Cay Durgun, Filiz Kula, Irfan Kula and Tulin Inkaya. They made my life wonderful in Arizona. I thank my friends Pinar Kanlikilicer, Gunsu Bagci and Pamir Cirdi. They made my life wonderful in Houston. I would also convey my thanks to my friends in Turkey; Ceren Ertas, Yasemin Deringol, Duygu Karaoglan, Muge Ozerten and Bike Kilic for their support through the course of this dissertation.

I am mostly grateful to my father Yusuf Ziya Yamak, my mother Fatma Gulen Yamak, my brother Mustafa Ayberk Yamak for their endless love and support. Thanks for giving me a shoulder to lean whenever I need. Without them, this work could not have been completed.

No one walks alone on the journey of life. Mustafa Gokce Baydogan, I am grateful that you were the partner of my journey in Arizona. Arizona has not been the place that I only pursued my doctoral studies but it is also the place where I met you. I cannot thank you enough for your love, trust, understanding, moral support, encouragement and guidance. I am looking forward to our journey ahead.

TABLE OF CONTENTS

CHAPTER Page

CHAPTER Page

CHAPTER Page

LIST OF TABLES

LIST OF FIGURES

Figure Page

Figure Page

CHAPTER 1

INTRODUCTION

Cardiovascular diseases (CVDs) are the leading cause of death globally. In 2008, 17.3 million people died from CVDs and it is stated that by 2030, 23.6 million people will die. CVD is the abnormal function of heart and blood vessels and it includes high blood pressure, coronary heart disease, heart failure and stroke. Almost half of the deaths from CVDs are due to the coronary heart disease which is also known as coronary artery disease (CAD) [1, 2]. Coronary artery disease is the narrowing of the blood vessels that nourish the heart muscle. A serious reduction of blood flow to the heart muscle is the situation when a coronary artery is narrowed to less than 30% of its original size [3].

Atherosclerosis is the condition of plaque buildup on the inside of the vessel wall and narrowing of the vessel [4]. Complicated morphology of atherosclerosis, which is the leading cause to acute coronary syndrome and myocardial infarction, made the development of diagnostic methods to detect it essential. Complete diagnosis of atherosclerosis requires entire imaging of coronary artery tree, characterization of the plaque including its morphology and major tissue components, remodeling of the vessel and inflammation. As of today, there is no diagnostic modality providing that comprehensive imaging. Currently available diagnostic modalities include both invasive and non-invasive imaging techniques. Invasive coronary angiography has been accepted as the routine procedure to detect coronary obstructions. However, non-obstructive plaques might be missed by invasive angiography until the late stages of the disease due to vessel remodeling [5, 6]. Intravascular ultrasound (IVUS) is now accepted as the reference for detection of non-obstructive plaques [7–9]. However, its invasive nature is associated with considerable procedural risks. Furthermore, its restriction to proximal and medial vessel segments and high costs prevent widespread acceptance of the procedure.

Computed tomography (CT) is a promising noninvasive modality for CAD assessment. CT imaging uses the differences of x-ray attenuation of body tissue to reconstruct the images. It has been shown that contrast enhanced CT imaging allows the visualization of coronary arteries with a reliable assessment of coronary artery stenosis [10, 11]. Furthermore the detection and quantification of large calcium deposits in coronary arteries is also possible due to the larger prevalence of MSCT and its high correlation with electron beam CT (EBCT) [12–16]. The recently developed technology of MSCT has the potential to identify and characterize the noncalcified coronary atherosclerotic plaques [17–27]. Tissue differentiation by CT is limited due to the overlap of the attenuation values of the plaque components, especially the lipid core and the fibrous cap. Differentiation of plaque components by MSCT which would be beneficial to identify patients with an increased likelihood of plaque rupture or erosion leading to acute coronary events is still an active research topic requiring prospective clinical trials.

Recently, dual energy CT (DECT) coronary angiography has been performed clinically. Its ability to characterize coronary artery plaques has also been studied [28–32]. Additional attenuation data provided by DECT looks appealing to characterize coronary artery plaques. DECT scanners have the ability to generate virtual monochromatic energy images, as well as material basis pair images by using two different X-ray energies in order to determine the energy dependency of tissue attenuation values for each voxel. This dissertation proposes feature extraction, feature selection and learning strategies for supervised characterization of coronary atherosclerotic plaques by using DECT. In my first study, I propose an approach for calcium quantification in contrast-enhanced examinations of the coronary arteries, potentially eliminating the need for an extra non-contrast X-ray acquisition. Clin-

ically used Agatston and Volume scores in the assessment of risk in terms of calcification are currently obtained using single energy acquisitions without iodine contrast. Calcium scores from non-contrast conventional and contrast-enhanced conventional scans did not demonstrate sufficient correlation for calcium quantification on CT coronary angiograms, likely due to the poor separation of calcium and iodine. The ambiguity of separation of calcium from contrast material was solved by using virtual non-contrast images provided by DECT. A measure of calcium plaque burden that is comparable to true non-contrast CAC scoring using DECT material basis pair images is the aim of this study. The study proposes a new threshold CT number to detect the calcium carrying potential risk for adverse coronary events on virtual non-contrast images. Using that threshold, the calcium scores obtained by contrast enhanced DECT and non-contrast single energy CT scans are compared. My second study explores the use of additional attenuation data provided by DECT for non-calcified plaque characterization. I propose to train supervised learners on pixel values recorded from DECT monochromatic X-ray and material basis pairs images, for more precise classification of fibrous and lipid coronary plaques. The interaction of the pixel values from different image types is taken into consideration, as single pixel value might not be informative enough to separate fibrous from lipid. Organic phantom plaques scanned in a fabricated beating heart phantom are used as ground truth to train the learners. My last study proposes automatic segmentation of coronary arteries characterizing plaque components and lumen on contrast enhanced monochromatic X-ray images. This study aims relevant feature extraction from region of interests on patient cardiac images. The extracted features include pixel and region based features. Feature selection is employed as a preprocessing step by using the feature importance measure from the random forest model.

The rest of this dissertation is organized as follows. Chapter 2 introduces atherosclerosis and current medical imaging modalities in assisting atherosclerosis. Fundamentals of X-ray physics and computed tomography are also covered in Chapter 2. Chapter 3 introduces DECT by discussing its evaluation, decomposition algorithms for it and by comparing it with single energy CT. Chapter 3 also introduces supervised learning approaches which have been used in this dissertation. Chapter 4 proposes an approach for calcium quantification in contrast-enhanced examinations of the coronary arteries. Chapter 5 proposes to train supervised learners on pixel values recorded from DECT monochromatic X-ray and material basis pairs images for more precise classification of fibrous and lipid coronary plaques. Chapter 6 proposes automatic segmentation of coronary arteries characterizing plaque components and lumen on contrast enhanced monochromatic X-ray images. Chapter 7 concludes and discusses several directions for future study.

CHAPTER 2

BACKGROUND

1. Atherosclerosis

Atherosclerosis is the condition of plaque buildup on the inside of the vessel wall and narrowing of the vessel [4]. Defined layers of a vessel wall are intima, media and adventitia as shown in Figure 1. The intima consists of endothelial cells and is separated from media by dense elastic membrane called internal elastic membrane. The media consists smooth muscle cells and is separated from adventitia by the external elastic membrane [33].

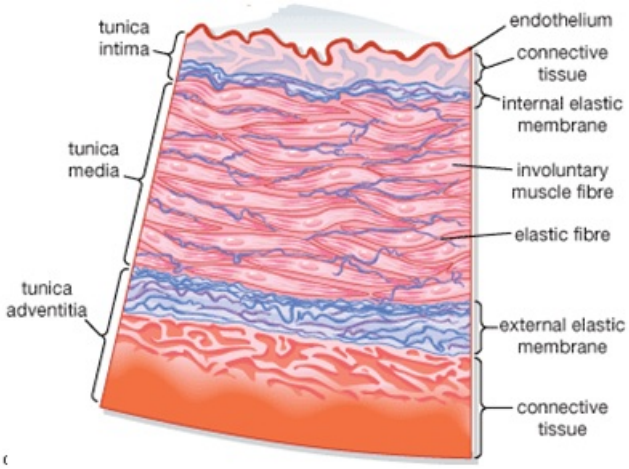

Figure 1. Schematic representation of arterial wall layers [33]

An atherosclerotic plaque raises a focal lesion within the intima by the deposition of fat, cholesterol, calcium and other substances as shown in Figure 2. When endothelium is infiltrated by fatty materials, macrophages are sent to the site to scavenge the materials and they form the foam cells which then die and also accumulate within the intima. This lesion is separated from the lumen by fibrous cap which can easily rupture [34].

When atherosclerotic lesions affect the coronary arteries, it may cause coronary occlusions and occlusions decrease the blood supply to the heart muscle hence result in death of some tissue of the heart muscle. Death of heart muscle tissue is called myocardial is-

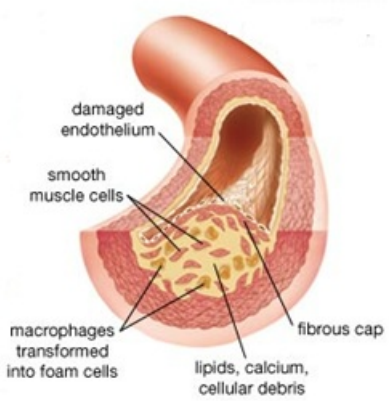

Figure 2. Illustrated artery narrowed by atherosclerosis plaque [34]

chemia which causes chest pains known as angina pectoris [35]. Decrease in blood flow also causes severe tissue damage which may result in formation of a blood clot known as coronary thrombosis at the side of the plaque [34]. Coronary thrombosis may lead to complete occlusion of one or two arteries and may cause the death of a section of the heart muscle resulting in myocardial infarction known as heart attack [34, 35].

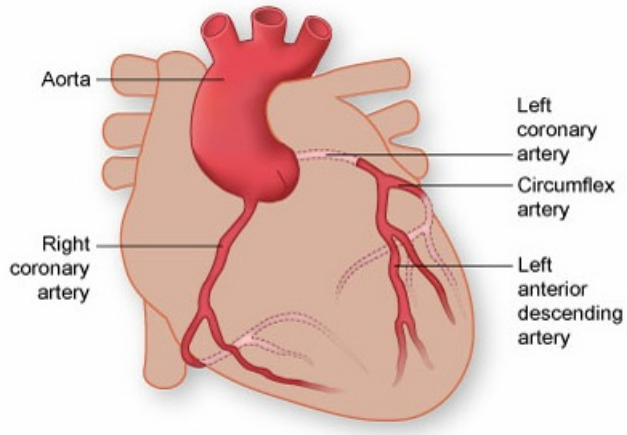

Figure 3. Illustrated anatomy of human coronary arteries [36]

The heart muscle needs oxygen rich blood to function properly. The blood supplied to the heart is carried by two main coronary arteries branching from aorta which are right and left coronary arteries as shown in Figure 3. Right coronary artery (RCA) supplies blood to the right side of the heart which pumps blood to the lungs. Left coronary artery supplies blood to the left side of the heart and it branches into the left anterior descending artery (LAD) and the circumflex artery (LCX). The left side of the heart is larger than the right side since it pumps blood to the rest of the body [36]. RCA, LAD and LCX are the three arteries affected by atherosclerosis. Partial or complete occlusion of these three arteries is the major cause of the coronary artery disease and the heart attacks.

Certain drugs that reduce the level of cholesterol in the blood or prevent formation of blood cloths can reduce the risk associated with atherosclerosis. In the case of occluded arteries, coronary bypass surgery is one option that routes the blood flow around the occluded area by using sections of blood vessels from other parts of the body. Balloon angioplasty is applied to dilate the artery and flatten the plaque. Dilated artery can get narrowed overtime therefore expandable wire mesh stents are inserted as a part of the angioplasty procedure [34].

According to American Heart Association 2013 statistical report 1 of 6 deaths was due to coronary heart disease in 2009 and mortality was 386,324. It is estimated that 635,000 Americans will have a new coronary attack and 280,000 will have a recurrent attack each year [37]. It is essential to diagnose the early stages of atherosclerosis development in coronary arteries and to apply necessary medication as well as the surgical procedures.

2. Medical Imaging in Assisting Atherosclerosis

2.1. *Invasive Imaging Techniques*

Angiography: Coronary angiography has been the gold standard for assessing the lumen boundaries [6]. The spatial resolution of coronary angiography provides spatial resolution from 0.13 to 0.20 mm with a temporal resolution up to 12.5 frames / sec [38]. Angiography is beneficial while assessing advanced coronary lesions (greater than 70%) but it does not provide reliable information about the content of the plaques. Since content of the plaque carries out valuable information to assess the risk of myocardial infarction, coronary angiography is a poor predictor for myocardial infarction. Furthermore it has been shown that majority of acute coronary occlusions occur at sites that were normal at angiography [39]. These limitations of coronary angiography promoted interest in alternative catheter based techniques to visualize the content of the plaques.

Angioscopy: Angioscopy is based on fiber optic transmission of visible light [40]. It provides colorful and three dimensional visualization of intraluminal structures. Furthermore it is a sensitive detector of intracoronary thrombosis [38]. The color of the plaque which is assessed by angioscopy is a good predictor of vulnerability of the plaque. Plaques are categorized as yellow or white by angioscopy and yellow plaques are more prone to rupture than white plaques. Yellow plaques are observed more often at the site of culprit lesion which is thought to be causing myocardial damage and increase the likelihood of an acute coronary event [41]. Although the technology of angioscopy is available and less expensive, it has many disadvantages. It does not provide information regarding plaque characterization and the size of the catheter (3.0 to 5.0 F) does not allow visualization of small vessels ($<$ 2 mm) and severe stenotic lesions. The technique is difficult to perform and depends on

the skills of the person performing the test therefore there is always the chance of injury of the vessel. The main disadvantage of this technique is the need of a blood-free field. For clear visualization of the vessel wall, the blood needs to be flushed away with saline which thereby may increase the risk of ischemia [42].

Intravascular Ultrasound (IVUS): IVUS produces real time images at 20 to 30 frames / sec with 100 to 200 μm axial resolution and 200 to 300 μm lateral resolutions [38]. Images provided by IVUS are more accurate and detailed than those obtained by angioscopy and angiography. IVUS images give information about the content of the plaque and information regarding remodeling of the vessel due to its high penetration depth (10 mm) [40, 43]. It has been shown that vascular remodeling by IVUS might help to assess plaques which are prone to rupture [44]. Current IVUS catheters range in size from 2.9 to 3.5 F and can be used to visualize small arteries and severe stenotic lesions [38]. One of the limitations of IVUS is the blind area behind the calcified regions. Because calcium does not allow the transmission of the ultrasonic beam thereby deeper structures are seen as black shadows on IVUS images [40]. Furthermore, the resolution of IVUS is not high enough to detect thin fibrous caps which are prone to rupture [38].

Intravascular Elastography: This technique is combined with ultrasound to measure the mechanical properties of tissue. It is based on differences in deformability of plaque components after the application of defined pressure. The radiofrequency data of IVUS are acquired under two levels of pressure. Soft plaques are expected to deform more and have higher strain level than hard plaques. Palpography which is a derivative of elastography uses one strain value per angle and color-coded contour at the lumen vessel boundary is plotted [6, 38]. In vitro studies have shown that there are differences between measured

strain levels of fibrous, fibro-fatty and fatty components of coronary plaques [45]. Intravascular elastography is a very sensitive technique thereby subject to significant artifacts. It is a catheter based technique and quality of the images are depended on the motion of the catheter.

Intravascular Thermography: Intense inflammation is discovered on plaques sites which are prone to rupture [46]. This inflammation results in temperature elevations that can be detected by catheter based thermistor that has a temperature accuracy of 0.05 °C and a spatial resolution of 0.5 mm [6]. Measurement of temperature is an easy and inexpensive technique however blood temperature can influence the findings. Thermography also does not provide information about the plaques without inflammation. Even though temperature might be used as a valid indicator of vulnerable plaques, this technique should be combined with another imaging modality for full plaque characterization.

Spectroscopy : Spectroscopy is a technique based on differences in absorbed energy at different wavelengths by different chemical compounds. Raman spectroscopy and near-infrared spectroscopy are the most validated ones [40].

- Raman spectroscopy (RS): Raman spectroscopy is based on the fact that when incident light with a wavelength 750 to 850 nm excites molecules in a tissue sample, light is scattered with changing the wavelength and intensity. Change in intensity and wavelength of scattered light is unique to the molecule and it needs to be processed to detect chemical compounds of coronary plaques. A Raman spectrum is presented as the Raman intensity on the Y axis and the wave length shift on the X axis [38]. The main limitation of RS is the poor penetration depth (1 - 1.5 mm) and absorbance

of light by blood. Furthermore RS does not provide geometric information about the plaques [6].

- Near-infrared spectroscopy (NIRS): Near-infrared spectroscopy uses a wavelength of 750 to 2500 nm and it has a larger penetration depth (2 mm) than RS [6]. A near-infrared spectrum is presented as absorbency extent of light by molecules on the Y axis and wavelength on the X axis [38]. Capability of NIRS to identify individual components is less than RS and it requires the use of pattern recognition algorithms for further classification [42]. Sensitivity and specificity rates for histological features of lipid pool, thin cap and inflammatory cells obtained by NIRS are promising according to a study accomplished by Moreno and his colleagues [47]. NIRS has been used to measure pH for further assessment of atherosclerotic plaque. The risk of plaque rupture or thrombosis is found to be correlated with decreasing pH [40]. Lack of structural information is the main limitation of NIRS. Both NIRS and RS can provide valuable information when they are combined with another imaging modality such as IVUS.

Optical Coherence Tomography (OCT): Optical coherence tomography is the intravascular imaging modality providing the highest resolution images of arterial wall with an axial resolution of 15 to 20 μm and lateral resolution of 20 to 40 μm. It is similar to IVUS except it uses infrared light with 1.3 μm wavelength instead of ultrasound. Images are generated by measuring the scattered light from the structures in the tissue. It provides real time imaging with 15 to 20 frames / sec. Its excellent resolution permits the detection of thin fibrous caps which are prone to rupture however limited penetration depth (1 -1.5 mm) does not allow to study vessel remodeling [43]. Imaging through the blood requires continuous flush

of normal saline with or without a proximal occlusion balloon thereby long acquisition time needed for complete visualization of coronary artery tree is not be possible [42].

2.2. *Non-invasive Imaging Techniques*

Magnetic Resonance Imaging (MRI): Magnetic resonance imaging is based on the differences in biophysical response of the tissue to an electromagnetic radiofrequency (RF) pulse application within a strong, static magnetic field. Application of magnetic field leads to alignment of proton spins within the body along the magnetic field direction and protons absorb energy when a short RF pulse is applied. The excited photons return to their equilibrium while the RF energy is released. RF signal decays with an exponential curve characterized by T1 which is called spin-lattice relaxation time. In addition to T1, the rate that transverse component of magnetization vector decays at is called spin-spin relaxation time known as T2. Images are constructed based on controlled contributions of T1 and T2 which are tissue composition dependent. In addition to T1 and T2 weighted images, proton density weighted images are constructed. This way only the signal changes coming from differences in the amount of available spins are used [48]. Several pulse sequences have been used to characterize the atherosclerosis plaque using a combination of T1, T2, proton density and three dimensional time of flight [40]. To improve the diagnostic accuracy of MRI for detection of vulnerable plaques, a number of novel targeted agents have been produced. These agents bind to target region and help imaging of very small components of plaques [49, 50].

MRI is a diagnostic imaging modality with excellent soft tissue contrast therefore able to analyze the components of atherosclerosis plaque components. It has been shown that MRI is applicable for visualization of atherosclerotic lesions in peripheral arteries [51, 52].

Coronary artery imaging for identification of coronary plaques and assessment of coronary artery size has also been shown to be possible [53,54]. However it is not clinically available due to required high spatial and temporal resolution that would be necessary for visualization of smaller dimension of the coronary arterial wall and its tortuous course.

Nuclear Imaging: Nuclear imaging uses radiolabeled tracers which are conjugated with gamma-emitting radionuclides. Radiolabeled tracers bind to or are taken up by the constituents of the atherosclerotic plaque. Single photon emission computed tomography (SPECT) and positron emission tomography (PET) are the two nuclear imaging modalities [55]. PET has greater spatial resolution (4 - 5 mm) than SPECT (1 - 1.6 cm) [17]. Several radiolabeled tracers that would provide diagnostic information regarding atherosclerosis plaque have been developed. The most commonly used tracer is 18F-fluorodeoxyglucose (FDG) in PET [17, 56]. FDG competes with glucose for uptake into inflammatory cells such as activated macrophages that have high metabolic activity at atherosclerotic site of the vessel [55]. FDT-PET imaging has shown to be useful to detect the plaque inflammation in carotid lesions [57]. However imaging coronary artery atherosclerosis is still a challenge for nuclear imaging due to insufficient temporal and spatial resolution of PET. Furthermore FDG-PET is limited due to lack of cellular specificity. FDG is also taken up by metabolically active myocardium [17].

Electron Beam Computed Tomography (EBCT): EBCT was first introduced in 1984 for the study of coronary artery disease [58]. An electron beam is emitted from an electron gun and is focused onto the target rings by magnetic deflection. Target rings are arranged in a half circle around the patient thus generating an X-ray source that rotates around the patient. The X-ray is measured with a stationary detector ring [59]. Unlike conventional CT,

the X-ray does not rotate around the patient thereby providing high temporal resolution (50 - 100 ms) [5]. Contrast enhanced EBCT has high specificity and sensitivity values for the visualization of significant coronary stenosis when compared to invasive coronary angiography. However 80% of the proximal and midcoronary segments have insufficient image quality for the assessment of stenosis [5, 38]. EBCT without contrast injection allows sensitive and accurate detection of coronary artery calcification [5, 59]. Calcium is a definitive marker of atherosclerosis and a prognostic indicator of adverse coronary events however the absence of calcium does not exclude coronary atherosclerosis. Moreover the presence of calcium does not predict the vulnerability of the plaque (non-calcified) and EBCT does not permit the detection of non-calcified plaque or the distinction between non-calcified and calcified plaque [5, 38]. The detection of calcium by EBCT provides obstructive coronary disease predication sensitivity up to 90% but the specificity is as low as 40% [38]. The low specificity and not adequate longitudinal resolution (3 mm) for visualization of small sized coronary arteries do not permit EBCT to be the routine imaging modality for coronary artery disease [59].

3. FUNDAMENTALS OF X-RAY PHYSICS

3.1. *Production of X-Rays*

X-rays for medical diagnostic purposes are produced by accelerating electrons and making them to collide with a metal target. Fast moving electrons lose their energy in the form of electromagnetic radiation when they collide with the target. The acceleration of the electrons is gained by the electrical potential difference between two electrodes called anode and cathode found in the x-ray tube, see Figure 4. X-ray tube acts as an energy converter, receiving electrical energy and converting it into x-radiation and heat. The quantity and the

quality of the x-radiation produced are controlled by adjusting the voltage applied to the tube, electrical current that flows through the tube and the exposure time [60, 61].

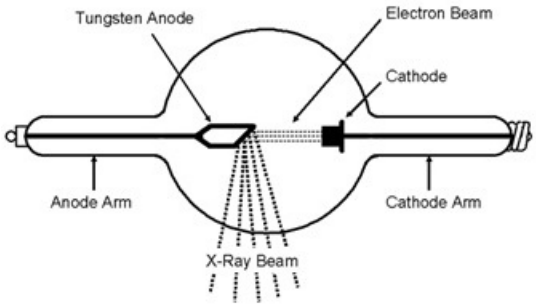

Figure 4. Simple diagram of the x-ray tube

Cathode: Cathode is the source of the electrons and is a helical filament made of tungsten connected to an electrical source which produces electric current. While this current heats the filament causing liberation of electrons, it controls the number of the electrons liberated. The cathode is surrounded by a focusing cap for the purpose of shaping the electron beam width. The voltage applied to the focusing cap determines the size of the focal spot on the anode. For example application of negative bias voltage to the focusing cap increases the repelling electric fields surrounding the filament and reduces the spread of the beam resulting in a smaller focal spot width. The other factor affecting the focal spot is the filament length which determines the focal spot length. Smaller the focal spot produces better visibility of the detail in the image however has a less heat dissipating capacity [60, 61].

Anode: Anode is the target of the electrons and made of tungsten or some alloy of tungsten due to its high melting point and high atomic number. It is at positive side of the electrical circuit and has two main purposes which are x-ray production and prevention of heat damage to the x-ray tube. As mentioned above, the area exposed to striking electrons on the

anode is called focal spot. These electrons deposit their energy either as heat or emitted x-rays. Prevention of the heat damage is achieved by rotating disk shaped anode. Anode angle is the factor affecting the effective focal spot size which is defined as the length and width of the focal spot as projected down the central ray in the x-ray field, see Figure 5. As anode angle gets larger, the effective focal spot gets larger resulting in a worse spatial resolution. The optimal anode angle is decided depending on the clinical application [60, 61].

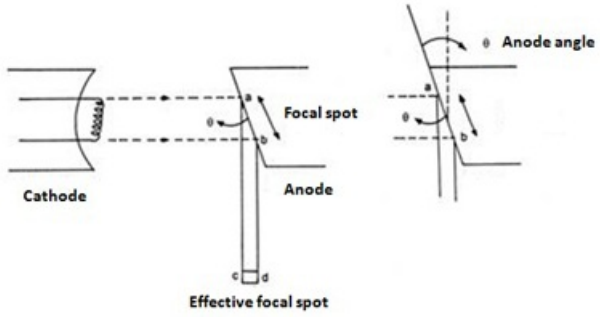

Figure 5. Effective focal spot is the focal spot area projected down the central ray in the x-ray field. As anode angle increases, the effective focal spot gets larger.

Electrons emitted from cathode accelerate through to the anode creating a kinetic energy. As they travel, their velocity increase and as the time they reach to the surface of the anode, all kinetic energy is converted to the potential energy. When electrons strike to the surface of the anode, all the kinetic energy is converted to x-radiation and heat. The strike of the electrons results in two types of interactions with individual atoms of the anode material called Bremsstrahlung and characteristic radiation, see Figure 6 [60, 61].

Bremsstrahlung Radiation: Bremsstrahlung radiation which is also known as the 'breaking radiation' happens when the electrons interact with the atomic nucleus. Electrons passing near proximity of the positively charged nucleus decelerate rapidly by the attractive force from the nucleus resulting in loss of kinetic energy which appears in the form of x-ray

photon. The energy of the x-ray photon depends on the distance between striking electron and the nucleus. As the distance gets shorter, the energy loss of the electron increases producing higher x-ray energies. To lose all the energy of an electron, a direct impact to the nucleus is needed which is a low probability therefore; most of the photons produced by this interaction have lower energies than the electrons [60, 61].

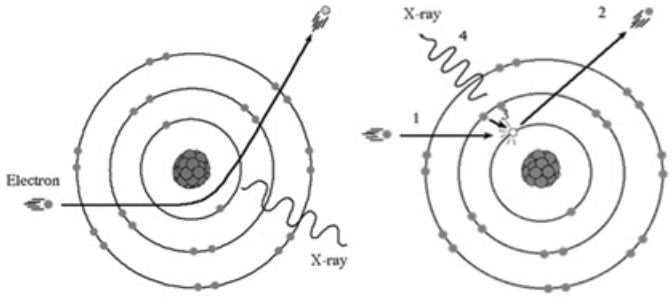

Figure 6. Left: Demonstration of Bremsstrahlung radiation, Right: Demonstration of Characteristic radiation

Characteristic Radiation: Characteristic radiation appears when the striking electron ejects one of the electrons of the target atom. For such an interaction, the energy of the striking electron must be larger than the binding energy of the electron of the target atom. When the electron is ejected, it leaves a vacancy and this vacancy is filled by an outer shell electron with less binding energy. As this vacancy is filled by the outer shell electron, x-ray photon with energy equal to the difference between the binding energies of the electron shells is released. K-shell (highest binding energy) vacancies filled by outer shells are the characteristic x-rays used in diagnostic imaging since other characteristics x-rays are mostly attenuated or filtered [60, 61].

3.2. *Interaction of X-Radiation with Matter*

While x-rays photons interact with the matter, they will either penetrate without interacting, scatter from their original direction or be absorbed by depositing their all energy. Rayleigh scattering, Compton scattering and photoelectric absorption are the three main interactions when diagnostic radiology is the subject matter.

Rayleigh Scattering: This scattering is also known as coherent, Thompson, elastic or classical scattering. This scattering occurs when the incident photon energy is not enough to create ionization in the atom. When incident photon interacts with the atom, the atom emits a photon of the same energy but not in the same direction. This type of scattering occurs with a low probability for x-ray interaction above 70 keV therefore in medical imaging it does not have much effect on image quality [60–62].

Compton Scattering: This scattering is also known as inelastic or non-classical scattering. When the incident photon interacts with the atom, photon with less energy is scattered and an electron is ejected from the atom. The energy of the incident photon is equal to the sum of the energy of the scattered photon and the binding energy of the ejected electron. The scattered photon and ejected electron can move in different direction than the incident photon. They move toward the forward direction as the energy of the incident photon increases resulting in detection by the image receptor. For a fixed scattering angle, increasing incident photon energy decreases the energy of the scattering photon, transferring most of the energy to the ejected electron however when medical imaging is the case, most of the energy of the incident photon is transferred to the scattered photon which might be detected by the image receptor. Detection of the scattered photon by the image receptor decreases the quality of the image by reducing the contrast. This type of scattering is significant in

medical imaging since the energy of the incident photon is mostly greater than the binding energy of the electron. Also the Compton scattering is directly proportional with the density of the material [60–62].

Photoelectric Absorption: In this interaction the energy of the incident photon is transferred to the electron of the interacted atom and the electron is ejected from the atom. While the ejected electron moves short distance in the matter, its energy is deposited in the matter. The ejected electron leaves a vacancy for the electrons with a lower binding energy and the vacancy is filled by an electron from outer shell. The difference between binding energies of these electrons is released as characteristic x-rays. The probability of the photoelectric absorption depends on the atomic number and the energy of the incident photon. As the atomic number of the absorbing material decreases, the probability of the photoelectric absorption decreases thus making photon interaction with the soft tissue difficult in medical imaging. Increasing the incident photon energy decreases the probability of the photoelectric absorption. The role of the atomic number in the probability of the photoelectric absorption is used to amplify differences in attenuation of tissues thus creating a better image contrast. While the atomic number has a large effect on the probability of the photoelectric absorption, Compton scattering is nearly independent of the atomic number. When lower energy incident photons are interacted with the high atomic number elements such as calcium or contrast material, photoelectric absorption dominates the interaction whereas in case of interaction with the soft tissue, Compton scattering does [60–62].

3.3. *Attenuation of the X-Rays*

As photons go through the matter some of them interact with the matter, some of them pass on through the matter. Both photoelectric absorption and Compton scattering cause some of the photons to be removed from the beam which is defined as attenuation.

Linear Attenuation Coefficient: The linear attenuation coefficient of a material is defined as the fraction of the photons removed from the x-ray beam per unit of thickness of the material. The other way, this coefficient is the indication of the rate of photon interaction and it is the sum of the individual linear coefficients for each type of interactions. The number of photons leaving the beam increases as the distance photons traveling increases. However this relation is not linear. The relation between the number of incident photons and the ones that are transmitted is as:

$$N = N_0 e^{-\mu x} \tag{2.1}$$

where N is the number of the photons that are transmitted , N_0 is the number of the incident photons, μ is the linear attenuation coefficient and x is the path length. The linear attenuation coefficient is depended on the energy of the incident photons and the atomic number and the density of the material. The attenuation coefficient decreases as the incident photon energy increases except the absorption edges of the material. At the absorption edges the attenuation increases due to the increasing interactions. Number of the atoms affect the interactions such as increasing number of atoms in the material increases the probability of the interaction. Since increasing density means increased number of atoms, attenuation is directly proportional with the density of the material [61, 62].

Mass Attenuation Coefficient: Mass attenuation coefficient is the expression of the attenuation in terms of unit mass and the relation with linear attenuation coefficient. It is

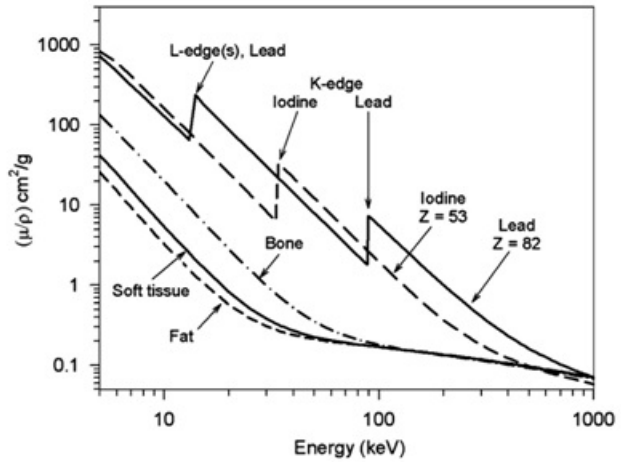

Figure 7. Mass attenuation coefficients of several materials used in diagnostic x-ray imaging versus photon energy (Adapted from [62])

expressed as:

$$\text{Mass Attenuation Coefficient}(cm^2/g) = \frac{\text{Linear Attenuation Coefficient}(cm^{-1})}{\text{Density of the Material}(g/cm^3)} \quad (2.2)$$

Mass attenuation coefficient is not dependent on the density of the material. The relation between the photon energy and the mass attenuation coefficient of several materials used in diagnostic x-ray imaging can be seen in Figure 7 [61, 62].

4. FUNDAMENTALS OF COMPUTED TOMOGRAPHY

The mathematical principles of computed tomography (CT) were first developed by Radon in 1917 proving that an image can be reconstructed if infinite number of the projections through the object is obtained. In 1979, Godfrey Hounsfield and Allan Cormack won the Nobel price by the invention of the CT scanner [61, 63]. During the history of CT, there have been several generations of CT. In this section I will be discussing the latest one.

4.1. *System Overview*

CT scanners have four major components which are gantry including x-ray tube and x-ray detector positioned with 180 degree angle, table, the high voltage generator and image generation system as seen in Figure 8. When the operator initiates a scan, series of commands are sent to the gantry which hosts the x-ray tube and the x-ray generator. Since the gantry needs to reach and maintain a stable velocity, mostly it is the first component responding to the operators command. The table reaches to the starting scan location and maintains a constant speed during the whole scan procedure. The voltage generator generates the desired voltage to the x-ray tube and keeps it constant at requested level during the scan. The x-ray tube generates the x-ray photons which are detected by the x-ray detector to produce electrical signals. The detector outputs are sampled at a uniform sampling rate to convert analog signals to digital signals. Image generation system which includes high speed computers and digital signal processing chips uses digital signals to preprocess, construct and enhance the images before they are displayed for clinical purposes [61, 63].

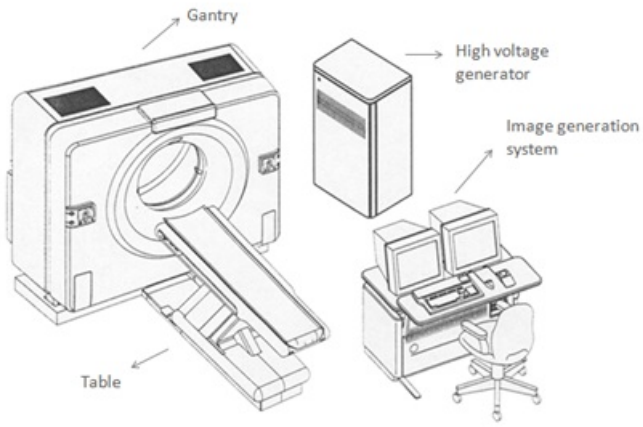

Figure 8. CT scanner system schematic

4.2. *X-Ray Detector Arrays*

Basics of x-ray tube were mentioned in production of x-rays sections therefore I will be skipping to x-ray detector which is equally important in image quality as x-ray tube. Opening the collimator which is the part narrowing the beam of the x-rays increases the usage of the x-rays produced by the x-ray tube in producing image data. With the single detector array scanners as collimator spacing gets wider, slice thickness increases thus improving the utilization of the x-ray beam but it reduces the spatial resolution. With the introduction of multiple arrays, instead of the collimator, detector size determined the slice thickness. Multiple detector arrays are composed of several linear detector arrays. Slice thickness is made adjustable by grouping one or more detector units together. Individual detector unit size changes depending on the manufacturer. Some manufacturers keep the detector unit size as 1.25 mm and constant for all, some keep the size smaller in the center four detector units such 0.5 mm and 1 mm for the others, some use increasing width size going away from the center. Detectors will be more discussed in the next section [61, 63].

4.3. *Data Acquisition and Parameters*

Modern CT scanner acquires data in two modes which are sequential, also called axial or spiral also called helical. In sequential scanning, data is acquired while the table is stationary. Table is moved to the next step in increments of the collimated detector width and the next slice data is acquired. X-ray tube is on only for the time data is being acquired thus saving radiation dose. In spiral scanning, the x-ray tube is on until the scanning is over and it rotates around the patient while the table is moving with a constant speed. During spiral scanning, radiation dose applied to the patient increases due to the continuous x-

ray exposure, however the time for the scan procedure decreases thus reducing the motion artifact due to the respiration [61, 63].

Tube Voltage: Tube voltage is the potential difference applied between anode and cathode of the x-ray tube. Increasing tube voltage increases the energy of the produced x-rays. In CT imaging tube voltage is used as x-ray energy and it is in unit of kilovolts (kV). Although the voltage across the tube can fluctuate, radiographic contrast is controlled by the peak voltage of the tube voltage and it is measured in peak kilovolts (kVp). Increased x-ray energy increases the photon reaching to the detector (penetrability) increasing the signal to noise ratio however the contrast resolution decreases due to the diminished photoelectric interactions. Increased energy of X-ray also increases the radiation dose which is proportional to the square of the tube voltage [61].

Rotation Time: Rotation time is the time period needed for x-ray detector to have a complete 360° rotation around the patient. Rotation time affects the scanning time. For a helical scanning with a short rotation time, a longer scan can be achieved. It is advantageous in terms of motion artifacts and usage of contrast material. Less motion is detected and less contrast material is needed since the scan time is shorter with a shorter rotation time [61].

Tube Current: Tube current is the other factor determining the radiation dose. Increasing the tube current increases the radiation dose. Tube current is the number of the photons traveling from cathode to anode and its unit is milliAmpers (mA). Increasing the tube current decreases the image noise making lower contrast detectability easier [61].

Pitch: Pitch is the used parameter when the helical scanning is the subject matter. If one single detector CT scanner is being used, pitch is defined as table feed per rotation divided by collimator width. When multi-detector CT scanner is the subject matter, the definition

for pitch changes since collimator width is not the one determining slice thickness. In this case, pitch is defined as table feed per rotation divided by one detector array width multiplied by the number of detector arrays. Pitch is an important parameter since it affects the radiation dose to the patient, the scan time and the image quality. Scans with smaller pitch (<1) produce better image quality however the radiation dose is increased. In clinical studies pitches up to 1.5 are used with partial scanning thus providing faster scan time, less radiation exposure and less patient motion [61].

4.4. *Image Reconstruction Parameters*

Increment and Slice Thickness: Increment determines the distance between images that are reconstructed. In axial scanning collimation spacing determines the slice thickness and if the table is moved between two sequences by a distance smaller than the collimated slice thickness, overlapping images can be obtained. Obtaining overlapping images provides less noisy images and better diagnosis for small structures. In helical scanning, with any increment selection overlapping images can be obtained in reconstruction process. In multiple detector array CT scanners, slice thickness is determined by the width of detectors which can be changed by combining different numbers of detector units. If scanning is axial, the center arrays determine the slice thickness while in helical scanning several slices are acquired simultaneously. In single detector CT scanners, collimators placed right in front of the x-ray tube determine the slice thickness. As the spacing of the collimation widens, the slice thickness increases. However the width of the single detector is the upper limit of the slice thickness. Larger the slice thickness better the contrast resolution is due to the increase in the number of detected x-ray photons but the spatial resolution decreases. Increasing the

x-ray tube current to compensate for the loss of contrast resolution is usually the case for protocols [61].

Scan Field of View: Scan field of view is defined as the largest area that can be scanned. As the reconstruction parameter, field of view (FOV) means the scanned area chosen for display. FOV is mostly composed of 512 X 512 pixels. The size of the pixel which is calculated as FOV (one side length) /512 defines the pixel resolution [61].

4.5. *Image Reconstruction*

Sinogram: Sinogram is the display of the data acquired by CT scanner before reconstruction of the images. In Figure 9, the sinogram on the left corresponding to the reconstructed image on the right is shown. The horizontal axis of the sinogram corresponds to the different x-rays in each projection and the views (angles) of the x-rays are shown on the vertical axis. The product of the view number and x-ray number per view gives the pixel number in the sonogram image. It is also the number of raw data points. Both the number of the views and the number of x-rays per view affect the resolution. Reducing the number of x-rays causes blurring and reducing the number of the views causes aliasing [61].

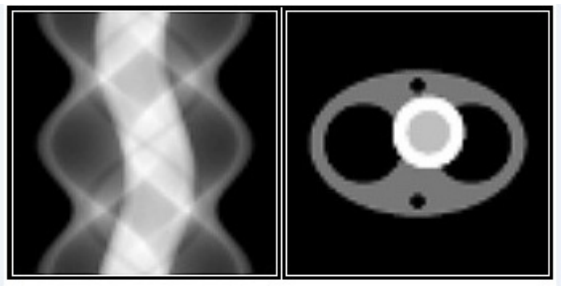

Figure 9. Left image is the display (sinogram) of the raw data for the reconstructed image on the right. The horizontal axis of the sinogram corresponds to the different x-rays in each projection and the views (angles) of the x-rays are shown on the vertical axis. (Taken from http://www.rmdinc.com/research/imagingtech-appreq.html on April 2nd, 2012)

Preprocessing Data: The attenuation of the x-ray is being measured by the CT imaging after passing through the material. The attenuation is quantified as a linear attenuation coefficient and computed as:

$$ln(I_0/I_t) = \mu x \tag{2.3}$$

where I_0 is the intensity of the source x-ray, I_t is the intensity of the x-ray recorded by the detector, x is the length of the path along the x-ray and μ is the linear attenuation coefficient. The linear attenuation coefficient is determined by the composition and density of the material for each voxel. The linear attenuation coefficient used in Eqn. (2.3) is the total attenuation coefficient for each x-ray and it is quantified as the integral over the x-ray path for every projection data. This equation holds under the assumption that x-ray beam consists of monoenergetic photons. Otherwise linear attenuation coefficient is not determined by only the material type, also the energy of the x-ray [61, 64].

Interpolation: Interpolation is only involved in helical scanning. During helical scanning, data are acquired in a helical path around the patient. The acquired data are interpolated into series planar image data sets. This step requires extra computation compared to axial scanning however it has the advantage of reconstructing the images at any position. The slice thickness defined by the detector width in multislice scanners and by the collimation spacing with single detectors determines the actual spatial resolution. Although images smaller than the slice thickness can be reconstructed, it does not mean that spatial resolution of the reconstructed slice thickness is achieved [61].

Backprojection Reconstruction: In CT imaging, reconstructed value in each pixel is the linear attenuation coefficient for the corresponding voxel. Once the raw data is obtained, planar projections are used to reconstruct the images. Several algorithms are used for the

reconstruction technique. Filtered backprojection is the algorithm mostly used for clinical CT imaging. Every ray in each view represents an individual measurement of linear attenuation coefficient. In addition to the linear attenuation coefficient, the acquisition angle and the position in the detector array corresponding to each x-ray are known. Before backprojecting the linear attenuation coefficients from each ray in all views onto the image matrix, the raw data is filtered to prevent blurring. Filtering step is the convolution of the projection data with a convolution kernel which refers to the shape of the filter function in spatial domain. Each projection data at a given angle which is a horizontal line from a sinogram is convolved with the convolution kernel [61, 65].

Reconstruction Kernels: There are different convolution kernels used depending on clinical applications. For clinical application where contrast resolution is more important than spatial resolution such as soft tissue imaging, the convolution filter is chosen to suppress the high frequency components therefore reducing the noise but lowering the spatial resolution resulting in loss of edges. On the contrary, in imaging of high attenuating materials such as bone edges become important therefore convolution kernels are selected those suppressing less high frequency components. Although the image becomes noisier, sharper edges are obtained [61, 65].

CT Number: It is said that in reconstructed CT image each pixel values are the linear attenuation coefficients of the corresponding voxel, however they are actually the normalized values of the linear attenuation coefficients based on following expression:

$$\text{CT number} = \frac{\mu - \mu_{water}}{\mu_{water}} * 1000 \tag{2.4}$$

where μ is the attenuation coefficient of the material, μ_{water} is the attenuation coefficient of water. CT numbers range between -1000 and 3000 and they are named as

Hounsfield units (HU). CT number of -1000 corresponds to air of which attenuation coefficient is 0, CT number of 0 corresponds to water and dense bone can have a CT number up to 3000 [61, 64].

4.6. *Image Display*

Once the image is reconstructed it is important to display it to physician with the best contrast for better diagnosis. Windowing and leveling are the basic procedures applied to CT images.

Windowing and Leveling: Reconstructed CT images are 12 bits of gray scale and the computer monitors can display 8 bits. Since human eye is not capable of resolving 256 shades of gray, reducing the number of shades of gray will give better contrast. Adjusting the image contrast is done by changing the window width and the level which is the CT number at the center of the window. The level and the window width together decide the slope of the window determining the range of the CT numbers displayed. Narrowing the window width results in greater contrast in the image. CT numbers lower than the smallest CT number in the window are displayed as black whereas CT numbers higher than the highest CT number in the window displayed as white in the image [61].

4.7. *Image Quality*

The measure of quality in clinic images is the utility of an accurate diagnosis and this utility lies in its spatial and contrast resolution. There is a trade-off between the contrast resolution and the spatial resolution. This trade-off will be discussed in the rest of this section.

Contrast Resolution: The primary advantage of CT is its contrast resolution compared to other clinical x-ray modalities. Contrast is the difference between closely adjacent regions in the image in gray scale and contrast resolution is the essence of visualizing the low-contrast objects in the image. Contrast to noise ratio (CNR) is used for assessing the contrast in images. CNR is calculated as:

$$CNR = \frac{A - B}{\sigma} \tag{2.5}$$

where A is the average density of a small region and B is the average density of an adjacent small region and σ is the standard deviation of the image noise. Increased noise reduces the visibility of low contrast objects. Noise in CT image is defined as the variation of the attenuation coefficients between individual pixels of the same material. Noise quantification is most commonly performed by scanning a container of water which is homogenous and has a CT number of zero. Distribution of the CT numbers of pixels within a region of interest would be a bell shaped curve. Determination of the standard deviation is mostly the way of quantifying the amount of noise in CT image. Contrast resolution is very much related to signal to noise ratio (SNR) which is measured as:

$$SNR = \frac{N}{\sigma} \tag{2.6}$$

where N is the mean number of photons per unit area which is defined as the pixel area and σ is the standard deviation or the noise. As the number of photons per unit area increases, noise increases by the square root resulting in overall increase in SNR. This type of noise is called quantum noise. Quantum is defined as something that can be counted or measured. In case of CT, measured quanta are x-rays, electron, ions or photons. Increasing SNR ratio can be achieved by increasing the photons which would also increase the radi-

ation dose applied to the patient. The factors that are affecting the contrast resolution are listed below [60, 61, 66].

- The applied tube current directly affects the number of photons. If the tube current is increased holding the rotation time fixed, number of photons increases thus increasing the SNR ratio thereby improving the contrast resolution. With the same logic, if every acquisition parameters are hold fixed except the rotation time, increasing rotation time increases the number of photons thus improving the contrast resolution.

- Thicker slices use more photons thus producing a higher SNR ratio. The slice thickness and the number of photons are linearly related thereby doubling slice thickness increases the SNR by $\sqrt{2}$.

- Increasing the field of view increases the pixel size thereby increasing the number of photons per pixel, the SNR ratio and consequently improving the contrast resolution.

- Depending on application, contrast might be more important than keeping the edge information. In that case, reconstruction kernels are chosen to produce higher contrast resolution by decreasing the noise.

- As the patient size increases, the attenuation of the x-rays increases resulting less x-rays being detected by the detector therefore reducing the SNR ratio and the contrast resolution.

Spatial Resolution: Spatial resolution can be defined as the ability to detect two very small objects which are very close to each other. Measuring the spatial resolution is done by stimulating the detector system with a single point input and observing the image produced

which is called *point spread function (PSF)*. For CT imaging a very thin metal wire is used to produce point spread function. Resulting point spread function should be same for every position for the system to be stationary. *PSF* also determines the blurring properties of the imaging system. Increased blurring reduces the visibility of small objects. The factors that are affecting blurring also affect the spatial resolution. These factors are discussed in the next section [61].

Blurring: Blurring in image can be caused both in scanning and reconstruction stages. The factors that are affecting the blurring in scanning stage are the size of the focal spot and the effective size of the detector. The cross sectional dimension of a ray, segment of an x-ray beam depends on the distance from both the focal spot and the detector. If the cross sectional dimension is larger than the object being imaged, the image will be blurred. Better visibility of details can be obtained by smaller focal spot or smaller effective detector size. The factors that are affecting the blurring in reconstruction stage are the voxel dimension and the reconstruction filter. Voxel dimension is controlled by three parameters which are field of view, matrix size and the slice thickness. Increased slice thickness increasingly blurs the image if the high density objects traverses through the patient with an angle. Field of view decides the dimension of the pixel with the matrix size. Smaller pixel dimension produces better visibility of details. Reconstruction filter is the other factor controlling the amount of blurring. Depending on the reconstruction filter chosen, the image can be blurred or the edges can be sharpened which would improve the spatial resolution [61, 66].

4.8. *Artifacts*

Beam Hardening: As the polyenergetic x-ray beam passes through the patient, lower energy x-rays are attenuated more than the higher energy x-rays resulting in beam hardening.

The beam hardening causes two types of artifacts which are cupping artifact and streak and dark bands. It is best to explain cupping artifact with a uniform cylindrical phantom scanning. As the x-ray beam passes through the middle of the phantom, they are passing through more material therefore x-ray beam is more attenuated than the x-ray beam passing through the edges. Hardened beam starts to attenuate less and when it reaches to the detector it is denser compared to the beam propagating from the edges, see Figure 10 .

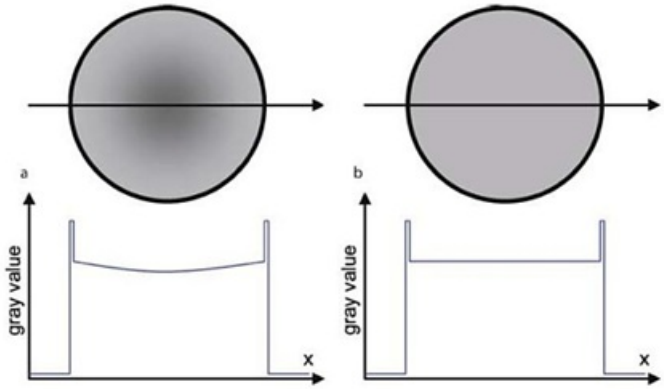

Figure 10. a. Attenuation profile with beam hardening b. Ideal attenuation profile

The beam hardening effect is also observed as streaks and dark bands due to the difference in attenuations of different materials. Attenuation of bone is greater than soft tissue attenuation thereby for the equivalent thickness, bones cause more beam hardening. Due to the heterogeneity, x-ray beam coming from different projection angles are hardened to a differing extent creating confusion during the reconstruction. Reducing the beam hardening effect can be done by filtering out the lower energy components to pre-harden the beam. Another filter is also used to further harden the edges of the beam. Using different size of phantoms to mimic the patient body, scanners are calibrated by the manufacturers. Beam hardening effect is also reduced during the reconstruction stage by the software [61, 67].

Partial Volume Averaging: The average of the attenuation coefficient of each voxel is what we see as the CT number in each pixel. When the voxel is composed of more than one tissue type, the CT number might be misleading. Partial volume artifacts can lead to misdiagnosis when the adjacent anatomic structures are not known. The best way to avoid partial volume artifact is to use thin slice acquisition [61].

Photon Starvation: The highly attenuating areas result in insufficient photon reaching to the detectors. Insufficient photons produce noisy projection data resulting in streaks in the reconstructed image. Photon starvation effect is mostly seen while the x-ray beam is traveling horizontally. On same scanners the tube current is automatically increased to supply sufficient photons for the scanning (horizontally scanning) duration of highly attenuating parts [67].

Aliasing: Aliasing effect can be caused by either undersampling within a projection or not having enough projections to reconstruct the image. If the interval between the projections is kept too large, small objects or sharp edges can be misregistered. Aliasing does not often lead to misdiagnosis however when fine details are concern, it should be avoided. Aliasing can be reduced by increasing the number of projections per rotation to decrease the interval between the projections. Undersampling within a projection can be avoided by quarter-detector shift or flying focal spot technique increasing the number of samples per projection [67].

Patient Motion: Patient motion can cause migregistration artifacts appearing as shading or streaking or blurring. The best way to avoid patient motion artifacts is to keep the acquisition time as short as possible. Respiratory motion which is unavoidable can be minimized if the patients can hold their breaths during the acquisition. During cardiac imaging, to mini-

mize the effect of the heart images are reconstructed by the projection data obtained when there is least cardiac motion. This is achieved by electrocardiographic gating techniques either by retrospectively triggered scans or prospectively triggered scans. With retrospective gating, modulated tube current is on during the entire scan whereas with prospective gating tube current is on only during the R to R interval of heart motion, see Figure 11 [61,67,68].

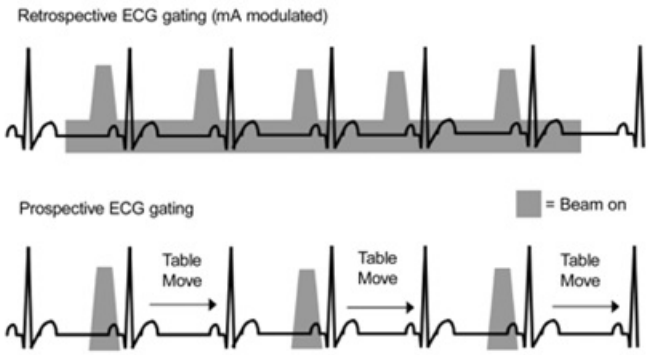

Figure 11. Retrospective gating versus prospective gating: With retrospective gating, modulated tube current is on during the entire scan whereas with prospective gating tube current is on only during the R to R interval of the heart motion [68].

Cone Beam Effect: Cone beam effect is caused by the divergence nature of the x-ray beam emitted by the x-ray tube. The z-axis of the x-ray beam gets wider as it travels through the patient. Due to the divergence of the x-ray beam, the data collected by the detectors are not consistent for each direction leading to streak artifacts on the image. The cone beam effect gets worse for the outer detector rows and increasing number of detector rows. Cone beam effect is prevented by cone beam reconstruction instead of standard reconstruction [67,69].

Helical Scanning Artifact: In helical scanning due the continuous table movement, the data collected for each slice is not sufficient for reconstruction. Missing data are estimated by interpolating between data collected from the nearest slice position. If the anatomy of the

patient changes significantly within the distance of interpolation, interpolated data might be inaccurate leading to streak and shading artifacts which is called ”windmill” artifact. The severity of the helical artifacts increases with increasing helical pitch [67, 69].

CHAPTER 3

MATERIALS AND METHODS

1. DUAL ENERGY COMPUTED TOMOGRAPHY

1.1. *Evaluation of Dual Energy Computed Tomography (DECT)*

The idea of dual energy computed tomography was first explored in the 1970's [70, 71]. Early studies demonstrated improved tissue characterization and less spectral artifacts on images. The use of dual energy was proposed for quantification of fat content in liver, calcium in pulmonary modules and bone mineral density [70–78]. However its utility was critical for clinical applications due to inadequacy in CT technology. Sufficient tube current at low tube voltages could not be provided by the x-ray tube and as a consequence low energy images were noisy. Another major limitation was the amount of time required for data acquisition leading to migregistration artifacts.

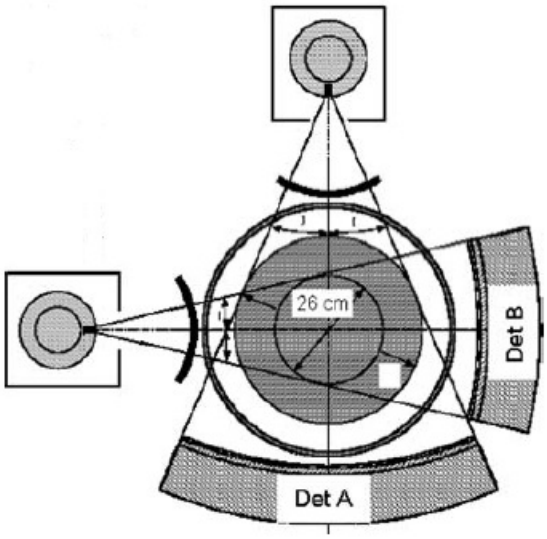

Figure 12. Schematic of first dual source CT, introduced by Siemens in 2006. Detector A covers the full scan field, detector B covers smaller field due to space limitation in the gantry [79].

Data acquired by dual energy can be obtained in several ways such as scanning twice, using energy discrimination detectors, using fast kV-switching x-ray tube or using dual x-ray source. The advantages and disadvantages of four different data acquisition ways are discussed in Y. Zou and M.D. Silver's paper [80].

First dual energy CT was introduced by Siemens in 2006 (SOMATOM Definition, Siemens Medical Solutions, Forchheim, Germany). The introduced dual energy CT system was equipped with two x-ray tubes and two detectors mounted with a 90° angle offset onto the rotation gantry. Both x-ray tubes can be operated independently at different voltage and current settings. One of the detectors covers the full scan field which has 50 cm diameter whereas the other detector covers a field of view with a 26 cm diameter due to the space limitations in the gantry, see Figure 12 [79].

After a while, GE introduced Discovery CT750 HD (GE Healthcare, Milwaukee, WI, USA). Discovery CT750 HD acquired dual energy scans with a single X-ray tube which utilizes static kVp alterations switching between low and high preset values within a period less than 1 ms. The raw data obtained by low and high energy scans are used to decompose into two materials density maps. Basis material pair images are then processed to obtain monochromatic attenuation coefficients at any desired energy [81, 82].

Dual energy CT has shown its immediate usefulness in clinical applications. Abdominal applications focus on detection of fat or iron deposition in liver, distinction of metastases and normal liver tissue [76, 83, 84]. Urinary applications focus on uric acid and cystine stones, renal masses characterization and detection of urinary stones in contrast-enhanced CT [85–87]. Thorax applications focus on lung perfusion imaging and detection of pulmonary embolism [88–90]. Cardiac applications focus on diagnosis of coronary artery

stenosis and myocardial ischemia. Several articles reported about specificity and sensitivity on detection of myocardial infarction and characterization of plaques, removal of calcified plaques to evaluate coronary stents [28, 91–93]. Vascular applications use the calcium subtraction, bone and plaque subtraction techniques to better visualize the vessels; also the ability of calcium removal makes iodine administration useful to enhance the attenuation of the vessels. In addition to calcium subtraction techniques in vascular application, virtual unenhanced images obtained by dual energy CT are used for imaging protocol applied on patients who had abdominal aortic aneurysm [94, 95]. M. Karcaaltincaba and A. Aktas compare fast kVp switching dual energy CT and dual source CT in some of the application areas in their paper [96].

1.2. *Dual Energy CT versus Single Energy CT*

Major tissues of the body have CT numbers ranged between -100 to 100 HU except the bone and the lung tissue. Small differences of the CT numbers make it hard to differentiate soft tissues on CT images. Therefore contrast agents such as Omnipaque, Visipaque or Ultravist are used in routine CT imaging to enhance the contrast for better differentiability. The radiation dose exposed to the patients when routine tests both include contrast and non-contrast CT scans can be decreased by eliminating the need for non-contrast CT scan since virtual non-enhanced images can be reconstructed by DECT.

The other limitation of CT imaging is that two different materials can have similar CT numbers thus resulting in misdiagnosis or uncertainty. DECT has been introduced for better differentiation of materials that have similar CT numbers by using additional spectral information of tissue attenuations. Figure 7 shows the mass attenuation coefficients over x-ray energy ranges. DECT aims to utilize the energy dependency of tissue attenuation.

The tendency of decrease of X-ray attenuation of different materials is the key point for better tissue characterization. Mostly used low and high X-ray tube voltages for DECT are 80 kVp and 140kVp of which effective energies are about 53 keV and 72 keV while the conventional single energy CT X-ray tube voltage, 120kVp is about 67keV [97].

In a single source conventional CT system, the reconstructed image approximates the linear X-ray attenuation coefficient of the scanned object at an effective energy of the incident X-ray beam. Polychromatic nature of X-ray results in beam hardening artifact. Spectral calibration is applied by clinical CT scanners to reduce the beam hardening affect. This process converts the measured projection data into line integrals through the patient by water precorrection algorithm which is based on energy dependence of water [98]. Although this correction algorithm forces water and water-like material attenuation to be constant, this artifact still limits the accuracy of the attenuation measurement of materials standing near high attenuating materials such as bone and contrast agents. In dual energy CT systems, measured projection pairs are decomposed into the density integrals of two basis materials and these images are further processed to obtain monochromatic attenuation coefficients of the object at any desired energy levels which are called virtual monochromatic images. The monochromatic images have more accurate CT values and do not suffer from the beam hardening affect [99].

1.3. *Decomposition Algorithms for Dual Energy CT*

In dual energy systems, the object is scanned at two distinct energy spectra. Once the dual energy data is acquired, decomposition can take place using sinogram data which is called pre-reconstruction technique or using the reconstructed image which is called post-reconstruction technique. Post reconstruction techniques utilize the reconstructed image at

low and high energy and get the weighted average of the two images to obtain best image quality. Pre-reconstruction techniques are superior to post-reconstruction techniques in terms of image accuracy however they require knowledge of the system's spectral response.

Pre-reconstruction decomposition initially was proposed by Alvarez and Macovski as modeling the linear attenuation coefficient of an unknown material into the components of photoelectric effect $\mu_p(E)$ and Compton scatter $\mu_c(E)$ as:

$$\mu(E) = c_1\mu_p(E) + c_2\mu_c(E) \tag{3.1}$$

where c_1 and c_2 are the unknown coefficients representing the fraction of photoelectric effect and Compton scattering [71]. The linear attenuation due to the Compton scattering is described by Kein-Nishna equation as:

$$\mu_c(E) = \frac{1+\alpha}{\alpha^2}\left[\frac{2(1+\alpha)}{1+2\alpha} - \frac{1}{\alpha}ln(1+2\alpha)\right] + \frac{1}{2\alpha}ln(1+2\alpha) - \frac{(1+3\alpha)}{(1+2\alpha)^2} \tag{3.2}$$

where $\alpha = E/510.975$ keV. The linear attenuation due to the photoelectric effect is described based on empirical models as [100, 101]:

$$\mu_p(E) = \frac{\rho}{A}Z^nE^{-r} \tag{3.3}$$

where ρ is the mass density, A is the atomic weight, Z is the atomic number of the material and effective energy is represented by E. The value of n has been approximated between 3.3 and 4.0 and the value of r has been approximated between 3.0 and 3.2.

The linear attenuation coefficient of an unknown material was then remodeled by Lehman and his coworkers inserting mass attenuation coefficients of two known materials that have different X-ray energy dependency as [100]:

$$\mu(E,x,y) = c_1(x,y)\mu_1(E,x,y) + c_2(x,y)\mu_2(E,x,y) \tag{3.4}$$

where c_1 and c_2 represent the amount of the basis material 1 and 2 in the voxel at x, y and μ_1, μ_2 are the mass attenuation coefficients of the basis material 1 and 2. In CT imaging, X-ray source is polychromatic and the target material is inhomogeneous so the X-ray intensity, I at the detector is modeled as:

$$I = \int \left[I_0(E,x,y) exp\left(- \int \mu(E,x,y) dl \right) \right] dE \tag{3.5}$$

where $I_0(E,x,y)$ is the source X-ray intensity and $\mu(E,x,y)$ is the line integral over the X-ray path. The projection measurement, p is defined as the minus log ratio of the source and the measured intensity, $p = -log(I/I_0)$. Linear attenuation coefficient model based on mass attenuation coefficients of two known materials requires two equations since there are two unknowns, $c_1(x,y)$ and $c_2(x,y)$. Therefore we need two intensity measurements obtained at high (H) and low (L) kVp such as:

$$\begin{aligned} I_H &= \textstyle\int I_{0H}(E) exp\left[-\mu_1(E) \int c_1(x,y) dl - \mu_2(E) \int c_2(x,y) dl \right] \\ I_L &= \textstyle\int I_{0L}(E) exp\left[-\mu_1(E) \int c_1(x,y) dl - \mu_2(E) \int c_2(x,y) dl \right] \end{aligned} \tag{3.6}$$

Projection data is obtained by taking the logs and the system equations become as:

$$\begin{aligned} p_H &= -log\left[\textstyle\int I_{0H}(E) exp[-\mu_1(E) L_1(l) - \mu_2(E) L_2(l)]\, dE / \int I_{0H}(E) dE \right] \\ p_L &= -log\left[\textstyle\int I_{0L}(E) exp[-\mu_1(E) L_1(l) - \mu_2(E) L_2(l)] dE / \int I_{0L}(E) dE \right] \end{aligned} \tag{3.7}$$

where $L_{1,2}(l) = \int c_{1,2}(x,y) dl$. The goal of DECT is to solve two equations in (3.7) for $L_{1,2}(l)$ and reconstruct $c_{1,2}(x,y)$. The reconstructed material basis images, $c_{1,2}(x,y)$ are not in Hounsfield Units (HU) instead they are in density units (mg/cm^3). Once the material basis images are reconstructed, monochromatic representation for any energy can be computed as [81]:

$$\mu_{Mono}(E,x,y) = \frac{c_1(x,y)\mu_1(E,x,y) + c_2(x,y)\mu_2(E,x,y)}{\mu_{water}(E)} \tag{3.8}$$

where $\mu_{water}(E)$ is the linear attenuation coefficient of water. Choosing the first basis material water Eqn. (3.8) simplifies to:

$$\mu_{Mono}(E,x,y) = c_1(x,y) + c_2(x,y)\frac{\mu_2(E,x,y)}{\mu_{water}(E)} \tag{3.9}$$

and the corresponding HU representation is $(\mu_{Mono}(E,x,y) - 1)1000$.

The advantage of two-material decomposition over Compton scattering and photoelectric effect decomposition is the knowledge of the mass attenuation coefficients of the two basis materials which can be obtained through NIST as a look-up table. Therefore, two-material decomposition is practically preferred over Compton scattering and photoelectric effect decomposition.

2. REGRESSION AND CLASSIFICATION

2.1. *Linear and Logistic Regression*

Linear regression is the most widely used of all statistical techniques and it tries to find the linear relationship between variables. A linear regression model has an input vector, $X^T = (x_1, x_2, \ldots, x_n)$ and tries to predict a real valued output vector $Y^T = (y_1, y_2, \ldots, y_n)$. The simple linear regression model has the form:

$$f(X) = \beta_0 + \beta_1 X \tag{3.10}$$

where $f(X)$ is the vector of expected values of the observation vector, Y and β_0, β_1 are the regression coefficients. The regression coefficients are unknown and estimated using the vectors, X and Y. The most popular estimation method is least squares in which regression coefficients are selected to minimize the residual sum of squares defined as:

$$\sum_{i=1}^{n} e_i = \sum_{i=1}^{n} \{\beta_0 + \beta_1 x_i - y_i\} \tag{3.11}$$

There are two important assumptions concerning the residuals. First one assumes that residuals are independent meaning that residual for one case does not give any information regarding another case. Secondly, residuals are assumed to be normally distributed. Details of linear regression can be found in [102].

Logistic regression is a prediction approach and it predicts a discrete outcome from set of variables, $X^T = (x_1, x_2, \ldots, x_n)$ that may be continuous, discrete, and dichotomous or any mix of these. Generally, the response or dependent variable, $Y^T = (y_1, y_2, \ldots, y_n)$ is dichotomous taking the value 1 with a probability of p or the value 0 with a probability of $1 - p$. The dependent variable can be more than two classes however linear regression is used in application where two classes occur such as presence/absence or success/failure. The discussion from now on is based on two class occurrence.

In logistic regression, the relationship between the predictor and the response variable is not assumed to be linear instead expected probability of the response variable, 1 for a given value of X is calculated as:

$$p_i = \frac{exp\left(\beta_0 + \beta_1 x_i\right)}{1 + exp\left(\beta_0 + \beta_1 x_i\right)} \tag{3.12}$$

Logistic regression model coefficients β_0 and β_1 are found by maximum likelihood estimation (MLE) instead of minimizing the squared residuals as in linear regression. The likelihood function (L) measures the probability of observing the dependent variable values that occur in the sample. MLE provides the coefficients of the logistic regression model by maximizing the log-likelihood function (LL) which can be defined as:

$$LL = \sum_{i=1}^{n} \{y_i log\left(p_i\right) + \left(1 - y_i\right) log\left(1 - p_i\right)\} \tag{3.13}$$

Performance of the model can be evaluated by correctly classified known samples. Details of logistic regression can be found in [102].

2.2. *Classification*

Classification is a supervised learning problem in which the input consists of a set of training examples and associated class labels, where each example is formed by one or more features (variables).

2.2.1. *Support Vector Machine.* Support vector machine (SVM) is a learning algorithm which produces nonlinear boundaries where the classes overlap (not linearly separable) by constructing a linear boundary in transformed version of features space. This transformation is applied by using kernel functions. Kernel functions project data from a low-dimensional space to a space of higher dimension in which the data become separable. The most popular kernels are Gaussian, polynomial and sigmoid kernel functions. The details of transformation of the data by kernel functions can be found [102]. Here I will be discussing the introductory information on SVM algorithm.

The basic idea of SVM is to find a hyperplane that would separate the data. Linearly separable data in two dimensions can be separated by a line however for higher dimensions a hyperplane is needed. The training data consists n pairs, $X^T = (x_1, x_2, \ldots, x_n)$ with D dimensions and each is in one of the two classes y_i=+1 or -1. A hyperplane can be defined such as:

$$x^T\beta + \beta_0 = 0 \tag{3.14}$$

The aim of the SVM is to orientate this hyperplane in such a way that make it as far as possible from the closest members of both classes. Chosen closest members of the both

classes are defined as support vectors and they would change the position of hyperplane if removed. The distance between the hyperplane and support vectors of both classes is equal and $\frac{1}{||\beta||}$. The total distance from the hyperplane on either side is $\frac{2}{||\beta||}$ and is called the *margin* , see Figure 13.

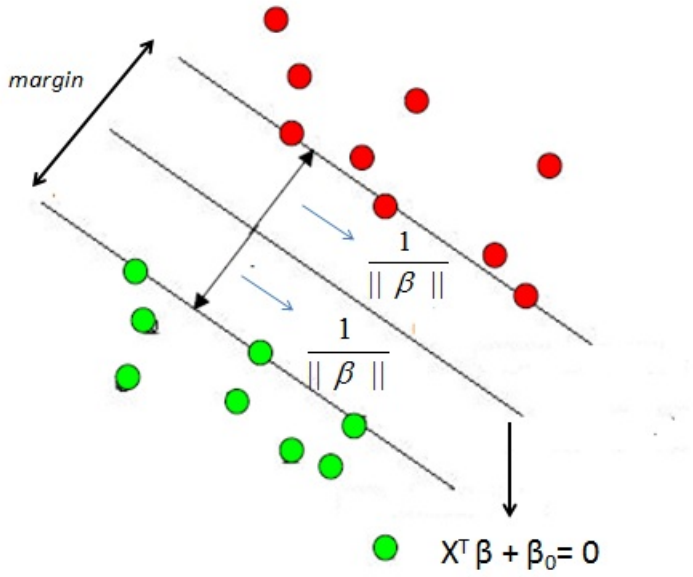

Figure 13. Hyperplane through two linearly separable classes

SVM selects the hyperplane that would create the maximum margin. In order to maximize the margin, β needs to be minimized which is an optimization problem solved by Lagrangian multiplier method. The details of SVM can be found in [102].

2.2.2. *Artificial Neural Network.* An Artificial Neural Network (ANN) is an information processing paradigm that is inspired by how biological nervous systems process information. An ANN is configured through a learning process for a specific application, such as pattern recognition or data classification. A typical neural network is represented by a network diagram as in Figure 14.

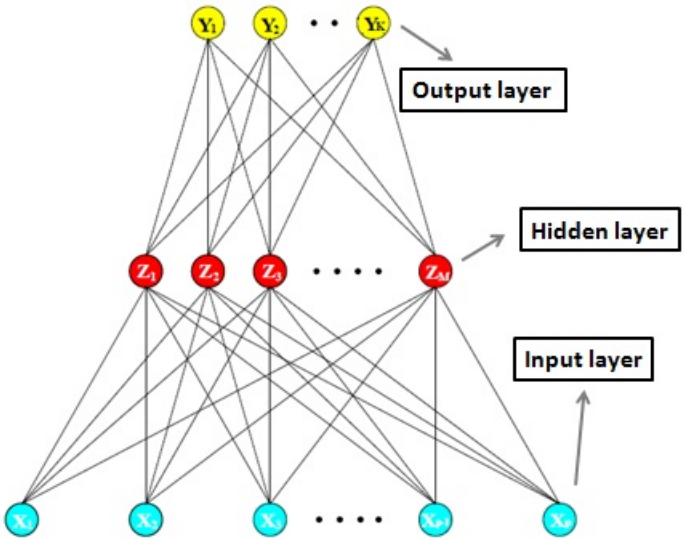

Figure 14. The basic architecture of neural network

For K class classification, there are K target measurements $Y_k = (Y_1, Y_2, \ldots, Y_K)$ at the top each being coded as 0 or 1 for the kth class. Target measurements are modeled as linear combination of the Z_m which are called hidden units. The values of Z_m are not directly observed and they are created from linear combinations of the inputs, X_p. There can be more than one hidden layer and hidden unit. Overall network model can be defined as:

$$\begin{aligned} Z_m &= \sigma(\alpha_{0m} + \alpha_m^T X), m = 1, 2, ..., M \\ Y_k &= \beta_{0k} + \beta_k^T Z, k = 1, 2, ...K \\ f_k(x) &= \rho(Y_k) \end{aligned} \tag{3.15}$$

where α_{0m} and β_{0k} are the bias units feeding into every unit in hidden and output layers, α_m and β_k are the unknown parameters and they are called weights, σ is the input function and ρ is the output function and they can be defined as ramp, step, sigmoid or Gaussian.

The neural network model seeks for the values of weights that make the model fit the training data. This is done by minimizing the performance function which can be defined as sum of squared errors, squared errors or cross entropy. Global minimizer of performance function is not the optimal solution since results an overfit solution.

The generic approach to minimize the performance function is called back-propagation and it uses gradient descent. This is done by a forward and backward pass over the network. In the forward pass, the current weights are fixed and the predicted values are computed. In the backward pass, the error between the target and the predicted values are computed and then back-propagated to compute the error for the hidden units. To compute the error for a hidden unit in the layer just before the output layer, all the weights between that hidden unit and the output units to which it is connected are identified. Then those weights are multiplied by the errors of those output units and summed up. This sum is the error for the chosen hidden unit. All the errors are then used to find the error derivates with respect to the weights. The details of ANN can be found in [102].

2.2.3. *Random Forest.* Random forest (RF) algorithm which is an ensemble of tree classifiers built on the random feature subspace based on the bagging idea [103]. RF grows B classification trees, $\{T_b, b = 1, \ldots, B\}$ and averages them. Each tree is grown on a different random subsample of the training data. This random subsample is composed from two-third of the training data (bootstrap sample) and left is not used for the construction of trees. The instances that are not used for the construction are available to test single tree and called out-of-bag (OOB) samples. The estimates computed from OOB predictions are easily obtained and have been shown to be good estimates of generalization error [103].

There are several impurity measures used to define the best way to split the instances such as classification error, entropy and Gini measure. RF uses the Gini measure to determine the split variable in the tree construction process. Let $p(i|t)$ denote the fractions of instances belonging to class i at a given node t. Gini impurity measure is computed as:

$$Gini(t) = 1 - \sum_{1}^{c} [p(i|t)]^2 \tag{3.16}$$

where c is the number of the classes. The effectiveness of a variable in classifying the training data is measured by *information gain*. Information gain is the expected reduction in impurity caused by partitioning the instances according to that variable. Information gain for a variable V at a given node t is calculated as:

$$IG(t, V) = Gini(t) - [\frac{N(L)}{N} Gini(t, L) + \frac{N(R)}{N} Gini(t, R)] \tag{3.17}$$

where $Gini(t, L)$ and $Gini(t, R)$ are the Gini measures of left and right child nodes of node t after being split based on a split value in variable V, N is the number of instances at parent node t, $N(L)$ and $N(R)$ are the number of instances in left and right child nodes. Splitting continues until there is no information gain for any split value of any variable.

While growing a tree, T_b for each node, $\sqrt{K}$ variables are selected randomly where K is the total number of variables, the best variable/split-point among the selected variables is picked and the node is split into two daughter nodes. Each tree is grown out to maximum size and left unpruned. To make a prediction for a new instance, x, let $C_b(x)$ be the class prediction of the bth tree. Then final decision for the instance would be $C_r f(x) =$ *majority vote* $\{C_b(x)\}_1^B$.

Variable Importance: Every time a split is made on, the Gini impurity measure for the two child nodes is less than the parent node. Adding up the Gini decreases, which is also

defined as information gain for each variable, over all trees gives a variable importance. Gini variable importance for variable V is computed as:

$$GVI(V) = \frac{1}{B}\sum_{b=1}^{B}(\sum_{t\in S_b} IG_b(t,V)I_b(t,V)) \tag{3.18}$$

where B is the number of classification trees, S_b is the set of split nodes of the tree b and $I_b(t,V)$ is an indicator variable for whether variable V was used to split node t of tree b.

CHAPTER 4

CORONARY CALCIUM QUANTIFICATION USING CONTRAST ENHANCED DUAL ENERGY COMPUTED TOMOGRAPHY SCANS

1. Introduction

Large amounts of calcium plaque in the coronary arteries is a known independent risk factor for adverse coronary events [104–106]. Conversely, a negative coronary calcium scan has a high predictive value for reduced risk of death from coronary artery disease (CAD). Non-contrast CT is the established and routine test for non-invasive detection of coronary artery calcium (CAC). Multidetector computed tomography (MDCT) at 120kVp, axial mode, and FOV 25 cm is widely used for coronary calcium scoring due to the high correlation between MDCT and the original method of electron beam CT (EBCT) [13–15,107]. MDCT with thin (2.5 to 3.0 mm) slices is commonly obtained using prospective gating, a technique that briefly irradiates (175 msec) during ventricular diastole of the R-to-R interval to decrease patient dose. In order to assess vessel patency, a second scan with iodinated contrast material is performed to delineate vessels and separate blood from myocardial tissue. Both acquisitions are obtained axially with thin slices and prospective gating. Image data are post-processed to create curvilinear plane images that follow coronary vessel curvature and aid visualization of the entire vessel.

Agatston score and Volume score are both used clinically in the assessment of risk in terms of calcification. Agatston scores are currently obtained using 120kVp CT acquisitions without iodine contrast. Computation of the score uses a threshold whereby pixels greater than 130 Hounsfield Units (HU) are classified as calcified tissue. For a given 'plaque' (composed of pixels more than 130 HU), the total area (mm^2) is multiplied by a weighting factor that depends upon the 'peak' CT HU contained in the plaque region [108]. Computing a

conventional Agatston score, S:

$$S = (w)(\text{Area of plaque}) \tag{4.1}$$

with weighting factor (w) given by:

$$w = \begin{cases} 0 & \text{if } CT^{max} < \text{ 130 HU} \\ 1 & \text{if 130 HU } \leq CT^{max} < \text{ 200 HU} \\ 2 & \text{if 200 HU } \leq CT^{max} < \text{ 300 HU} \\ 3 & \text{if 300 HU } \leq CT^{max} < \text{ 400 HU} \\ 4 & \text{if 400 HU} \leq CT^{max} \end{cases}$$

Plaque scores from all vessels are summed to calculate at a composite score. A total CAC score from all major arteries in the heart describes the extent of coronary artery disease. If the total CAC score is 0, there is no identifiable disease. If total CAC score is 1 to 99, mild disease is present. If the total CAC score is 100 to 399, moderate disease is present. If the total CAC score is greater than 400, severe disease is present. Alternatively, a Volume score, V is computed as:

$$V = (Volume_{Voxel})(Number_{Voxel}) \tag{4.2}$$

where $Number_{Voxel}$ is the number of calcified voxels. Volume scores use the 130HU threshold for calcium identification and attempt to quantify the total volume of calcification in the coronary vasculature [109–111].

Recently, DECT coronary angiography has been performed clinically [112]. DECT has the ability to generate virtual monochromatic energy images as well as material basis pairs

images. DECT derived monochromatic x-ray images suffer far less from the blooming artifact so that large calcium plaques may not interfere with assessment of residual lumen. However they may not sufficiently separate calcium from iodine [12]. Dual energy CT material basis pairs images display mass density (mg/cm^3) as the CT number [80]. DECT acquisitions enable the reconstruction of material basis pair images chosen by the operator [71]. Reconstructing the material basis pair images Calcium(Iodine) or Water(Iodine) produces virtual non-contrast images from the iodine contrast enhanced portion of a fast-switched DECT. We selected calcium and iodine as basis materials to allow for the creation of 'virtual' non-contrast calcium images in which calcium content is preserved in the image. This approach may provide a measure of calcium plaque burden that is comparable to true non-contrast CAC scoring [14]. The purpose of this study is to evaluate a direct measure of calcium burden by using DECT during contrast enhanced coronary imaging, potentially eliminating the need for an extra non-contrast x-ray acquisition. However, concern may exist for added radiation dose with DECT. A conventional CCTA coupled with non-contrast CACs is about 2.8mSv. A single fast-switched DECT is approximately the same at 2.7mSv without the extra non-contrast acquisition [112]. Therefore, dose neutral DECT total exam can possibly be achieved if the non-contrast exam can be eliminated.

2. Materials and Methods

Both dual energy and conventional single energy coronary imaging were performed using a General Electric (GE) Discovery HDCT750 (Waukasha, WI). This unit was equipped with fast voltage switching and Gemstone Spectral Imaging (GSI) cardiac protocols. All conventional CT coronary acquisitions were 120kVp, while DECT switched between nominal 80kVp and 140kVp during each projection. Post-processing of conventional and GSI

data was performed using a GE Advantage Windows (AW Waukesha, Wisconsin) workstation equipped with standard Agatston and volume scoring tools. No software tools are commercially available that support Agatston and volume scoring using source data from dual energy acquisition. An in house MATLAB (Natick, Massachusetts) program was utilized for volume and calcium mass scoring with DECT data sets. For consistency, conventional CT calcium scores were also generated using a MATLAB program. The AW provides a suite of GSI processing tools for generation of monochromatic energy image data and also provides operator selectable material basis pairs for material basis image creation and clinical viewing (DICOM compatible). Material basis pair images were created for Water(Iodine), Iodine(Water), Calcium(Water), Water(Calcium), Calcium(Iodine), and Iodine(Calcium). By convention, an image identified as Calcium(Iodine) displays the calcium content from a calcium and iodine basis pair. Calcium and iodine were compelling choices as basis materials since those materials provide a meaningful description of the materials present when attempting to evaluate calcium during the peak enhancement phase of coronary artery imaging.

In order to calibrate DECT iodine enhanced data, several determinations were necessary. Firstly, the equivalent 130 HU threshold must be specified in equivalent material density units for Calcium(Iodine) image. Secondly, using the specified threshold, the calcium mass and volume scores were calculated on virtual non-contrast images and correlated to the Agatston and volume scores obtained by true non-contrast scans.

2.1. *Equivalent 130 HU Threshold Determination for Calcium(Iodine) Image*

Two different methods were performed to find the equivalent 130 HU threshold for DECT scoring.

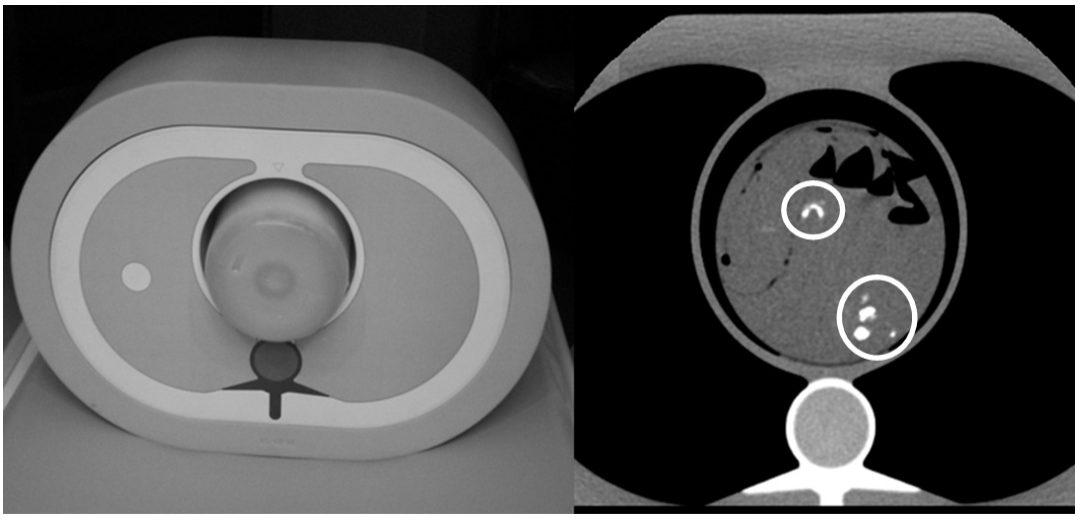

Figure 15. Left - Phantom containing endarterectomy tissue samples in 4% iodine:saline. Right - Axial slice at 120kVp with circles around calcium plaque samples. All 29 calcium plaques from six patients were imaged.

The first method aimed to correlate DECT calcium density values with 120kVp HU values using the pixel values recorded from Calcium(Iodine) and 120kVp images of six anonymous ex-vivo patient tissue samples (endarterectomy surgery specimens) which provided 29 calcified plaques. Six bags filled with patient plaques were surrounded by saline solution and inserted into a cardiac CT calibration phantom [109]. The phantom, shown in Figure 15, consists of an anthropomorphic chest section with artificial lung that mimics human tissue in density and attenuation characteristics. All 29 patient calcium plaques were scanned with prospective ECG triggering, 16x2.5mm collimation, 0.35sec rotation, and pitch of 1. The plaques were scanned at the conventional 120 kVp and with fast switched DECT 80kVp and 140kVp. Images were reconstructed with a field of view (FOV) of 25cm using cardiac standard kernel and image thickness and increment of 2.5mm. Region of Interest (ROI) was determined according to the edges of the calcium plaques in 120 kVp

images and ROI locations were co-registered between conventional images and DECT images. Each pixel value (mg/cm^3 or HU value) within each plaque was recorded for both image types. Linear regression analysis was performed between conventional CT HU and Calcium(Iodine) mg/cm^3 data.

The second method applied was logistic regression, which is generally used to predict the occurrence probability of an event. Defining calcium burden within a contrast material containing coronary artery can be considered as a two class classification problem whereby one class is calcium and the other class is iodine enhanced blood. Predictor variables were chosen as the pixel values collected from Calcium(Iodine) images of calcified plaques and iodine enhanced blood. Previously mentioned 29 calcified plaques obtained from six anonymous ex-vivo patients were used to define the predictor variables of calcium class. Note that the pixels corresponding to the pixels equal or higher than 130 HU on 120 kVp images were collected since 130 HU threshold specifying in equivalent material density units for Calcium(Iodine) image needed to be defined. The pixels to define the predictor variables of iodine enhanced blood class were collected from six patients whose Institutional Review Board (IRB) and Health Insurance Portability and Accountability (HIPAA) approvals and patient written informed consents were obtained. All six patients received both conventional and non-contrast single energy CT scan coupled with contrast enhanced fast-switched DECT scan of the coronary arteries. Non-contrast scans were prospectively triggered using 120kVp, 750mA, 0.35sec rotation, 1.0 pitch, and 16x2.5mm detector configuration. DECT scans were prospectively triggered using 80kVp/140kVp, 715mA, 0.35sec rotation, 1.0 pitch, and 64x0.625mm detector configuration. DECT protocols were adjusted for two patients and acquired with 765mA and 0.6sec rotation. Three patients received contrast en-

hancement with Omnipaque 350 (GE Princeton, New Jersey) at 5 cm^3/sec, and the other patients received Visipaque 320 (GE Princeton, New Jersey) at 4 cm^3/sec. Axial images were constructed at 75% of the R-to-R interval using a FOV of 25 cm and 'standard' kernel with image thickness and increment of 2.5mm.

2.2. *Preliminary Patient Examinations: Calcium Scoring*

A total of 92 images obtained from six patients mentioned previously were used to extract the coronary arteries and the aorta. Both non-contrast single energy and contrast enhanced DECT, acquisitions covered all calcified areas in the vessels, as given in Figure 16. Agatston and volume scores were calculated for conventional CT data, volume and calcium mass scores were calculated for Calcium(Iodine) DECT image data. Calcium mass scores, S_{Mass} were computed as:

$$S_{Mass} = \text{(CT Value)}(Volume_{Voxel})(Number_{Voxel}) \tag{4.3}$$

where $Volume_{Voxel}$ is the volume of one pixel, $Number_{Voxel}$ is the number of calcified pixels and CT value is recorded mean CT value of calcified area. Pixels having a CT value higher than the specified equivalent 130 HU threshold in material density units for Calcium(Iodine) image for DECT image data were averaged to find the mean CT value of the calcified area. Correlation was checked between volume scores obtained by 120 kVp and DECT Calcium(Iodine) image data, also between calcium mass scores obtained by DECT Calcium(Iodine) image data and Agatston scores obtained by 120 kVp image data.

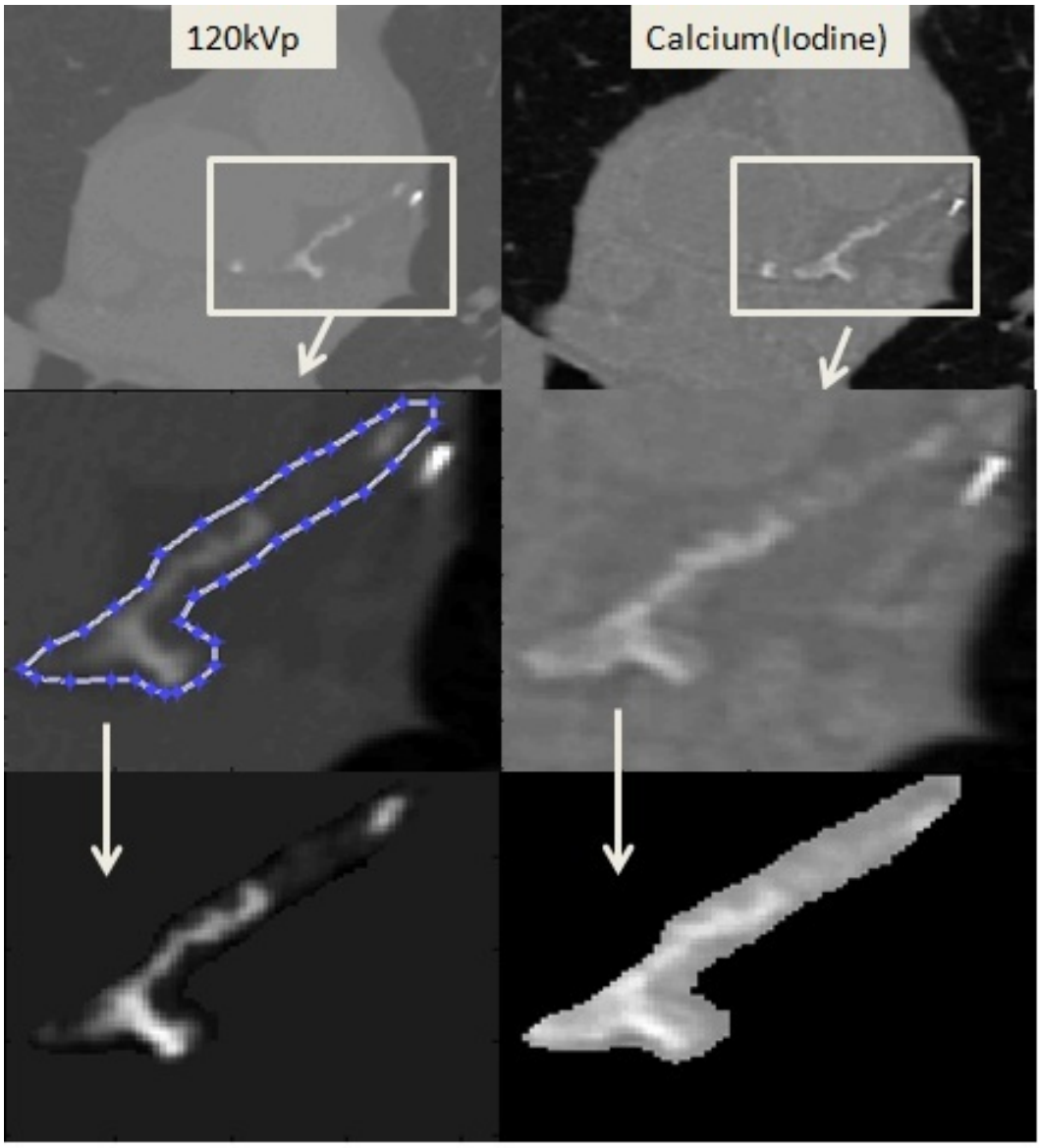

Figure 16. Same Plaque in 2 images. First Row: Left - Conventional 120kVp non-contrast protocol. Right - Calcium(Iodine) DECT with iodine contrast administered (virtual non-contrast), Second Row: Demonstration of vessel extraction (same boundaries are used while extraction is being done on Calcium(Iodine) images), Third Row: Extracted vessels

3. Results

3.1. *Equivalent 130 HU Threshold Determination for Calcium(Iodine) Image*

In the first method the 29 ex-vivo calcium plaques shown in Figure 15 were used to compare conventional 120kVp HU values with DECT calcium density measurements. The

linear regression analysis applied between 8924 pixel values obtained from 120 kVp and DECT Calcium (Iodine) images (see Figure 17) gave the 120kVp threshold of 130HU as 1611 mg/cm^3 for Calcium(Iodine) images. ($p < 0.0001$, $R_{sq} = 81.1\%$)

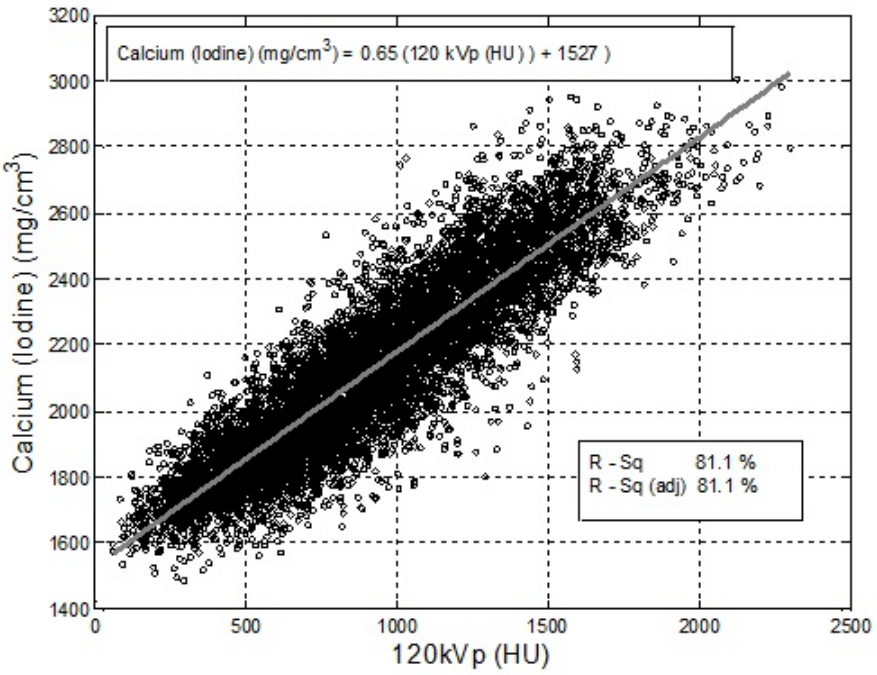

Figure 17. Calcium(Iodine) density measurements with 4% iodine contrast are correlated with 120 kVp for calcium plaque specimens. Based on the output equation of the model 120kVp threshold of 130HU as 1611 mg/cm^3 for Calcium(Iodine) images.

Linear regression model is based on the mean of the pixel values however mean of the pixel values were not the complete description of our data. Figure 18 shows that corresponding Calcium(Iodine) pixel values for 500 HU varies approximately between 1600 mg/cm3 and 2200mg/cm3. For further analysis, the assumption of the residuals being normally distributed was checked by plotting the histogram and the normal probability of the residuals in Fig. 18. The assumption of residuals being normally distributed is essential for the validity of the model. The histogram showed that residuals are distributed normally.

Next step to confirm the normality is to check the normal probability plot of the residuals. If the plot is an approximate straight line, then the assumption of residuals being normally distributed is valid. Normal probability of residuals was plotted versus cumulative normal percentile for a qualitative analysis to determine if the residuals were normally distributed (see Fig. 18). The normal probability plot of residuals showed a reasonably linear pattern in the center of the data; however, the tails showed departure from the fitted line. Although the histogram showed normally distributed residuals, the tails showing departure from the fitted line on normal probability plot concluded that normal distribution of the residuals was not an adequate fit for this dataset and the model was not valid. Therefore, the threshold found by linear regression model could not be used.

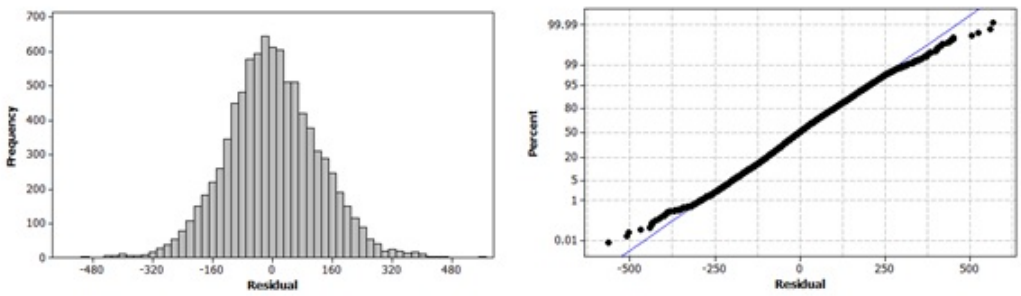

Figure 18. Left - Histogram of the residuals obtained by linear regression analysis performed between conventional CT HU and Calcium(Iodine) mg/cm3 data. Right - Normal Probability Plot of the residuals obtained by linear regression analysis performed between conventional CT HU and Calcium(Iodine) mg/cm^3 data.

The second method was based on a two class classification problem using pixel values recorded from Calcium(Iodine) images. A logistic regression model was trained to predict the class of pixels. Discrimination capacity of logistic regression model was measured by ten fold cross validation. Logistic regression model parameters that fit the data were

found to be -76.45 for the intercept and 0.045 for the pixel value. The output of the logistic function was the probability of pixel being calcium. Pixel value that would make the logistic regression model equal to zero gave the result of logistic function (probability of being calcium) as 0.5. The equivalent 130 HU threshold value for Calcium(Iodine) image was chosen to be the pixel value, 1699 mg/cm^3 that gave the probability as 0.5 according to the logistic regression model. Assessment of agreement between predictions and actual classes was shown in the classification table with class error rates, see Table 1. Total error rate was found to be 2.45%.

	Calcium	**Iodine**	**Class Error Rate**
Calcium	8609	296	3.32%
Iodine	139	8686	1.57%

TABLE 1. The classification table describing the agreement between actual and the predicted classes of the pixels. The sum of rows is equal to the recorded calcium plaque and iodine enhanced blood pixels, whereas the sum of columns is equal to the predicted calcium plaque and iodine enhanced blood pixels, respectively. Incorrectly classified pixels are 2.45 % of the total.

Further assessment of the logistic regression model was performed by creating the relative operating characteristic curve (ROC) relating relative proportions of correctly and incorrectly classified pixels over a continuous range of probability threshold levels (see Figure 19). Varying the probability threshold incrementally across the predicted probability range of the logistic regression model, true positive rates (sensitivity) and false positive rates were generated. Sensitivity and false positive rates were generated as in Eqns. 4.4 and 4.5. Positive instances are displayed as the calcium pixels on Calcium(Iodine) image.

$$\text{Sensitivity} = \frac{\text{Number of positive instances correctly predicted}}{\text{Total number of positive instances}} \tag{4.4}$$

$$\text{False positive rate} = \frac{\text{Number of positive instances incorrectly predicted}}{\text{Total number of negative instances}} \tag{4.5}$$

Discrimination capacity is described as the area under the ROC curve. A model that has no discrimination capacity will generate a ROC curve that followed the 45° line and the perfect discrimination is indicated when ROC curve follows the left hand and top axes of the unit square. The area under the ROC curve of our logistic regression model was higher than 0.9, indicating a very good discrimination which shows the sensitivity rate being high relative to the false positive rate. The area can also be interpreted as the probability that the model will correctly distinguish between calcium plaque pixels and iodine enhanced blood pixels.

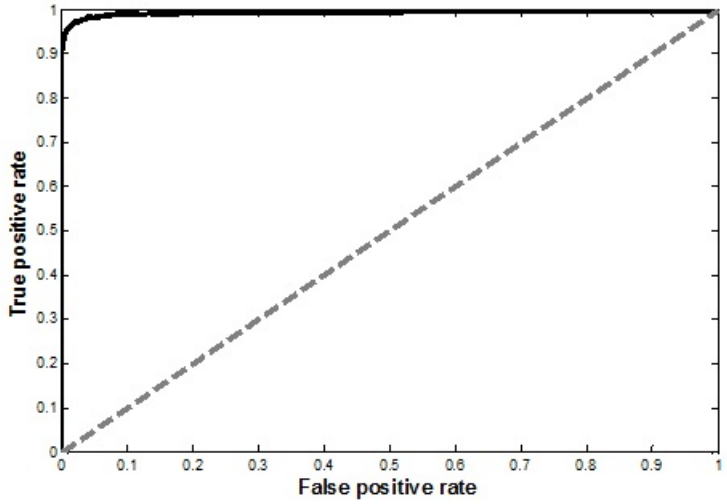

Figure 19. The ROC curve of the logistic regression model. The area under the ROC curve was higher than 0.9 indicating a very good discrimination. This shows the sensitivity rate being high relative to the false positive rate.

3.2. *Preliminary Patient Results*

Calcium was extensively present in the majority of these patients, including all three coronary arteries (RCA, LAD and LCX) of four cardiac patients and at least one artery in the remaining patients. Four of the patients also had calcium in their aorta, and these plaques were included separately to achieve a higher overall score. For demonstration detection of calcium plaque in RCA of one the patients using the threshold on Calcium(Iodine) image can be seen in Figure 20. Pixels marked with red are equal or over the threshold (1699 mg/cm^3) and used in calcium scores calculations.

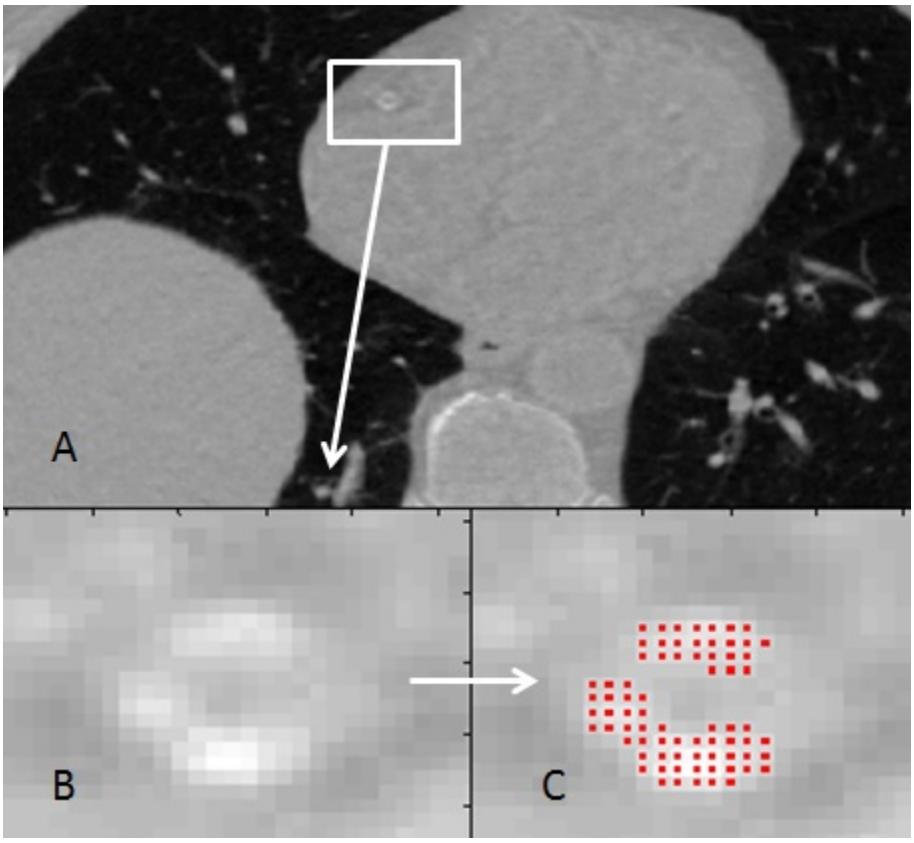

Figure 20. A. Calcium(Iodine) DECT image with iodine contrast administered (virtual non-contrast). RCA is located. B. Enlarged image of RCA. C. Pixels marked with red show the detected calcium plaque in RCA.

Calcium mass and volume scores from contrast enhanced dual energy Calcium(Iodine) images were used to define the correlation with Agatston and volume scores obtained from non-contrast single energy 120kVp images. Figure 21 compares results of measured total calcium burden obtained using DECT with administered iodine contrast to conventional non-contrast Agatston scored values on six patients on 17 vessels. Pearson's correlation coefficient between Agatston and calcium mass score was found to be 0.980. $(p < 0.0001)$

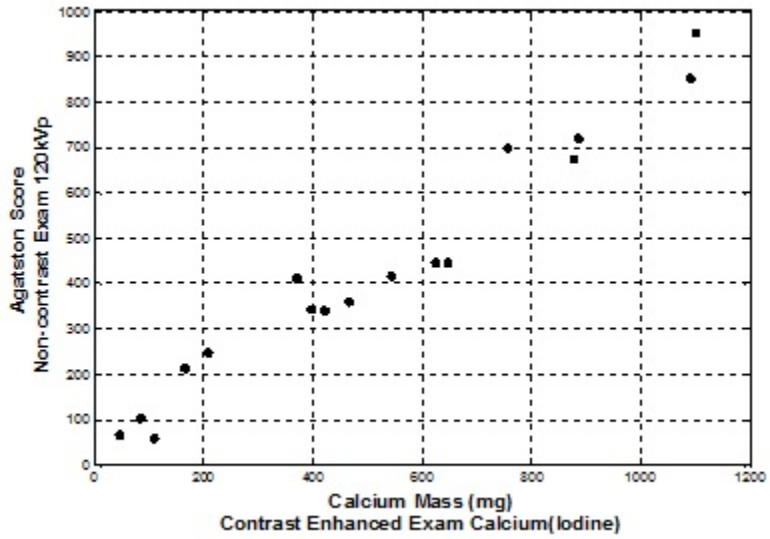

Figure 21. Conventional (non-contrast) Agatston score values for patients/plaques obtained using fast switched DECT. Image data for calcium mass measurements were obtained using the Calcium (Iodine) material basis pair following iodine administration. Pearson correlation = 0.980

In Figure 22, volume scores obtained from non-contrast single energy 120kVp and contrast enhanced dual energy Calcium(Iodine) images are compared on the six patients on the same 17 vessels. Pearson's correlation coefficient between volume scores was found to be 0.982. $(p < 0.0001)$

4. Discussion and Conclusion

The results demonstrate that separation of calcium is possible in Calcium(Iodine) image obtained by contrast enhanced DECT scans. This separation allows the assessment of calcium mass in Calcium(Iodine) images as it relates to conventional Agatston and Volume scores. Since calcium may not be separated from iodine contrast agent, iodine contrast enhanced scans showed wrongly elevated score values with conventional polychromatic images. It should be noted that exact mass density can only be understood with the application of vendor specific calibration factors applied to the mg/cm^3 density values obtained with Calcium(Iodine) images.

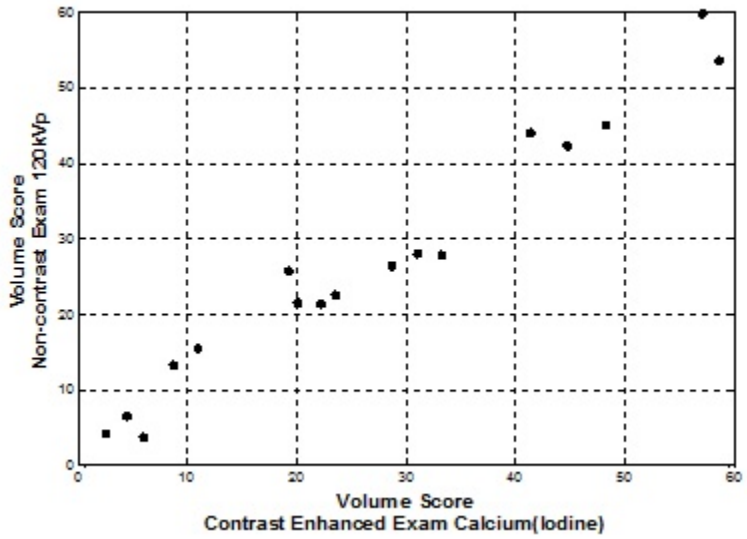

Figure 22. Conventional (non-contrast) Volume score values for same patients/plaques obtained using fast switched DECT. DECT Image data for calcium volume measurements were obtained using the Calcium (Iodine) material basis pair following iodine administration. Pearson correlation = 0.982

As presented, the preliminary patient studies demonstrated a correlation between conventional non-contrast 120kVp Agatston scores and contrast-enhanced Calcium(Iodine)

calcium mass scores. Patient studies also indicate a correlation between non-contrast 120kVp volume scores and contrast-enhanced Calcium(Iodine) volume scores. Both of these correlations indicate that quantification of calcium plaque burden using a contrast enhanced DECT is possible.

Several limitations of this study are relevant.

- Predicator variables of calcium class in logistic regression analysis were collected by recording pixel values from 29 ex-vivo calcium plaque specimens. Using 29 ex-vivo calcium plaque specimens might raise the question whether or not the sample size is enough to cover all possible densities of calcium found in coronary arteries. In this study, rather than finding the minimum pixel value to define calcium burden, we aimed to find the equivalent 130HU threshold for equivalent material density units for Calcium(Iodine) image. The data set had pixels corresponding to 130HU and higher. The maximum pixel value that would cover the calcium plaque was void of interest for this study, since pixels having corresponding 130HU threshold or higher values were counted to score calcium.

- Predicator variables of iodine enhanced blood class in logistic regression analysis were collected by recording pixel values of iodine enhanced blood from six patients. Small number of patients might be a concern at this point; however, the variability of actual patient data having different injection rates with two different contrast agents was part of this assessment. Also the pixels were recorded from different positions of arteries or aorta.

- The available number of patients for the comparison of calcium scores obtained by DECT and conventional CT limits the conclusions that calcium mass scores or volume scores obtained by DECT scans can take the place of Agatston scores or volume scores obtained by non-contrast CT scans for clinical purposes. Strong linear relation between the calcium scores obtained by contrast enhanced DECT and non-contrast CT is observed in Figure 21 and 22. However, this study is preliminary, and more patients who receive both conventional and non-contrast single energy CT scan coupled with contrast enhanced DECT scan need to be included to support this study.

While the proposed approach used Calcium(Iodine) as the basis pair materials, more accurate estimation of calcium burden in dual energy may be possible if the selected calcium pair was brand specific and not elemental iodine. Additionally, multi-material decomposition whereby three or more materials are included in the decomposition analysis may improve the specificity for quantifying calcium. Studies have shown that full contrast material elimination can be possible when water, bone and iodine are selected as the three basis materials when constructing the images [113]. Brand specific material decomposition might allow better elimination of contrast material in the image and more accurate calcium scoring with contrast enhanced DECT.

In this study, one approach for calcium quantification in contrast-enhanced examinations of the coronary arteries was demonstrated. The method involved finding a threshold that would detect calcium plaque and separate it from the iodine enhanced blood. Agatston scores from non-contrast conventional and contrast-enhanced conventional scans did not demonstrate sufficient correlation for calcium quantification on CT coronary angiograms, likely due to the poor separation of calcium and iodine. The significance of this study is

that a radiation dose neutral single DECT exam may provide both the calcium scoring and the arterial imaging for routine cardiac assessment.

CHAPTER 5

NON-CALCIFIED CORONARY ATHEROSCLEROTIC PLAQUE CHARACTERIZATION BY DUAL ENERGY COMPUTED TOMOGRAPHY

1. Introduction

The rupture of unstable and often non-obstructive atherosclerotic coronary plaque is known to be the primary cause of acute coronary syndrome [114]. Vulnerability of atherosclerotic plaque has been related to specific compositional characteristics, especially a large lipid core covered by a thin fibrous cap [114,115]. Complete diagnosis of atherosclerosis requires entire imaging of coronary artery tree, characterization of the plaque including its morphology and major tissue components and remodeling of the vessel. As of today, there is no diagnostic modality that can provide the necessary comprehensive imaging. Current available diagnostic modalities include both invasive and non-invasive imaging techniques. Invasive coronary angiography has been accepted as the routine procedure to coronary occlusions. However, non-obstructive plaques might be missed by invasive angiography until the late stages of the disease due to vessel remodeling [5, 6]. Intravascular ultrasound (IVUS) is now accepted as the reference for detection of non-obstructive plaques [7–9]. However, its invasive nature is associated with considerable procedural risks. Furthermore, its restriction to proximal and medial vessel segments and high costs prevent widespread acceptance of the procedure.

The potential of computed tomography (CT) has made CT a promising noninvasive modality for CHD assessment. CT imaging uses the differences of x-ray attenuation of body tissue to reconstruct the images. It has been shown that contrast enhanced CT imaging allows the visualization of coronary arteries with a reliable assessment of coronary artery stenosis [10, 11]. The recently developed technology of MSCT has the potential to identify and characterize the non-calcified coronary atherosclerotic plaques [17–27]. Whether

differentiation of plaque components by CT would be beneficial to identify patients with an increased likelihood of plaque rupture or erosion potentially leading to acute coronary events is still an active research topic requiring prospective clinical trials. The characterization of non-calcified plaques is challenging due to the substantial overlap of attenuation by CT. Well defined cut-off values to identify the lipid and fibrous plaques in coronary arteries have not yet been established.

Recently, DECT to characterize atherosclerotic plaques has also been studied [28–32]. Additional attenuation data provided by DECT looks appealing to characterize coronary artery plaque. In 2008, Barreto et al. performed a study where coronary atherosclerotic plaque components were classified based on ex-vivo DECT imaging of human coronary arteries with comparison to histology [28]. Both contrast enhanced and non-contrast DECT images of seven coronary arteries were obtained at 80kVp and 140 kVp. Plaques were classified as densely calcified, fibrocalcific, fibrous or lipid-rich. Analysis of non-contrast data at 80 kVp and 140kVp showed significant differences in the attenuation only for densely calcified and fibrocalcific plaques. After contrast injection fibrous plaques also showed significant attenuation differences, whereas lipid-rich plaques did not. In 2010, Zachrisson et al. performed an in vitro study where different soft tissue samples were classified using attenuation values coming from DECT scans at two energies [32]. Postmortem tissue samples commonly present in arterial plaques were collected during autopsy. CT values of the tissue samples were recorded at 140kVp and 80kVp and mean CT values were computed for each voxel. Logistic regression was used to predict tissue types from measured CT values and computed mean CT values. Prediction models showed that combining CT values at two energies improved the classification of different kinds of fat tissue.

The purpose of this study is to explore the use of supervised learning approaches trained on the additional attenuation data provided by DECT for characterization of fibrous and lipid plaques. Training data consisted of organic phantom plaques fabricated from low density polyethylene (LDPE) and high density polyethylene (HDPE) scanned in a fabricated beating heart phantom. The pixel values from energy specific (keV) and material basis pairs images provided by DECT were considered as the input to the supervised learners. We evaluated the performance of approaches by testing both on phantom and patient data.

2. Materials and Methods

2.1. *Phantom Study and Training*

Organic phantom plaques fabricated from low density polyethylene (LDPE) and high density polyethylene (HDPE) were used in this study [112]. Lipid and fibrous plaques were constructed with LDPE having a density of 0.92 g/cc and HDPE having a density of 1.2 g/cc respectively. In Figure 23, fabricated phantom lipid plaque is shown for illustrative purposes. After four of each phantom plaques (fibrous and lipid) were inserted into the beating heart phantom [116], the arteries were filled with 5% iodine (Visipaque 320 mg/mL Iodixanol, GE Healthcare) by volume. DECT acquisitions were performed using prospective ECG triggering. Acquisitions were switched between 80kVp and 140kVp during each projection. Data was transferred to a GE AW workstation with GSI computational tools for providing 1) a range of monochromatic X-ray (40 to 140 keV) images, and 2) material basis pairs images (Water/Iodine, Calcium/Water, Calcium/Iodine) [112]. This way, 17 images were constructed for the same data using different keVs and material basis pairs. Scanned phantom fibrous and lipid plaques provided 177 and 142 voxels from a total of 16 region of interests, respectively. For each voxel, 17 pixel values were recorded from monochromatic

X-ray and material basis pairs images. In Figure 24, recorded pixel values from 40keV, 60keV, 80keV, 100keV, Calcium(Water) and Iodine(Calcium) images of phantom fibrous and lipid plaques are plotted for illustrative purposes. Recorded pixel values from 17 images were used as features to train ANN, SVM and RF models for classification of fibrous and lipid plaques. The features used for ANN and SVM models were scaled to have a mean of 0 and standard deviation of 1. Scaling of the features was not necessary for the RF model since the RF algorithm is scale invariant.

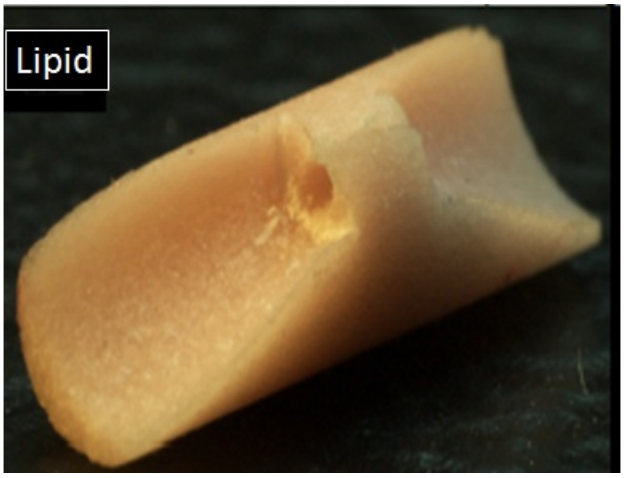

Figure 23. Fabricated phantom lipid plaque [112]

2.2. *Evaluation Measure and Parameter Settings For Selected Algorithms*

During the training process, parameters for the ANN, SVM and RF models were set to be used in testing on patient data. While setting the parameters for the models, k-fold (k=10) cross validation classification error rates were considered to evaluate the performance of the models. By 10-fold cross validation, training data was split into 10 sets of which 9 were used for training and 1 for testing. Error rate was defined as the ratio of misclassification. The parameters providing the minimum error rate were set for the models.

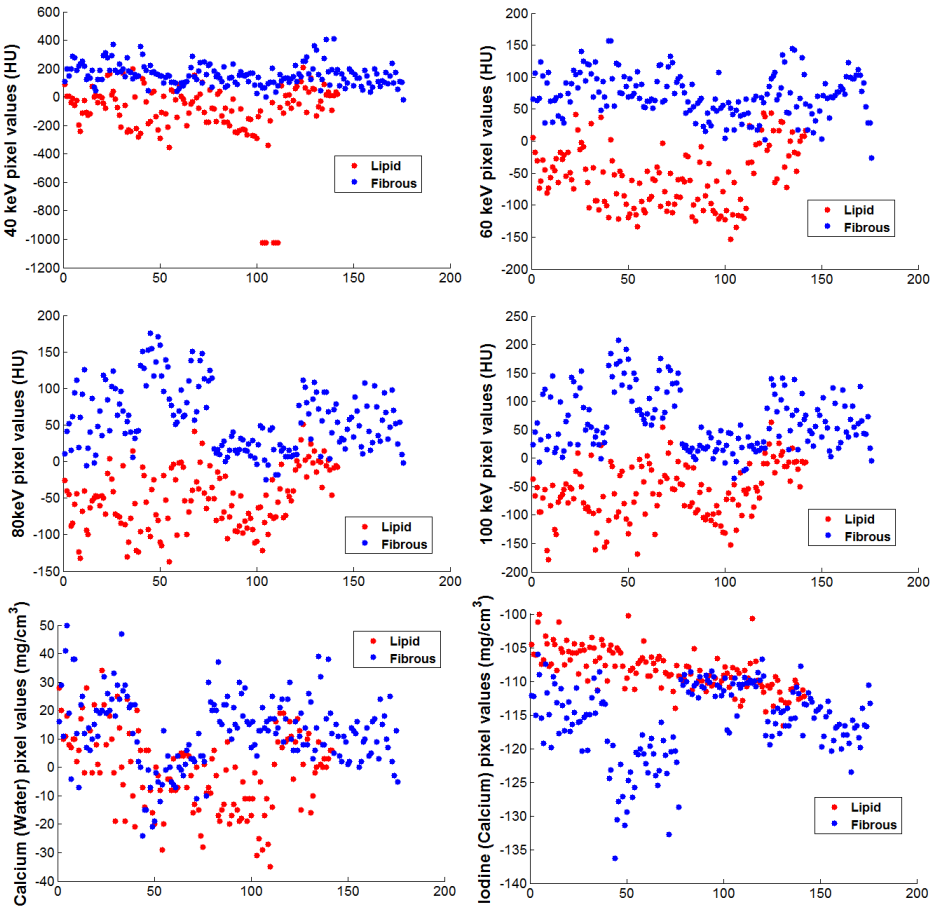

Figure 24. The plots show the recorded pixel values on 40keV, 60keV, 80keV, 100keV, Calcium(Water)and Iodine(Calcium) images of lipid and fibrous phantom plaques on y-axis.

Besides error rates of each model, error rates by majority voting were calculated for each class (fibrous and lipid). Majority voting worked by classifying to the class receiving the largest numbers of votes or predictions by three models (ANN, RF and SVM).

2.2.1. *Support vector machines.* The radial basis function (RBF) was used as the kernel function. Using the kernel function as RBF required the tuning of two parameters: gamma parameter of kernel function, γ and cost parameter, C. Training was performed

with different values of C and γ. The best result was obtained with value of 1 for both C and γ. MatLab computing software (The MathWorks, Natick) was used for SVM classification. The sequential minimal optimization (SMO) method was chosen to find the separating hyperplane.

2.2.2. *Artificial neural networks.* Back-propagation ANN trained with the Levenberg-Marquardt algorithm was used to train the weights and the biases. The best result and fastest convergence was obtained with two hidden layers each with 10 nodes in our preliminary experiments. Sigmoid transfer function was used as the transfer function of input and hidden layers and the linear transfer function was used as the output transfer function. The output layer had two nodes. The goal of the training process was to have zero for the first output node and one for the second output node if the target class was fibrous and one for the first output node and zero for the second output node if the target class was lipid. The performance function was defined as the mean sum of squares of the network errors (MSE). MatLab computing software (The MathWorks, Natick) was used for ANN simulation and training. Training was stopped when the desired MSE was reached.

2.2.3. *Random forests.* The RF model picked four out of 17 features randomly while growing a tree for each node. The only parameter that needed to be set by the user was the number of trees. The number of the trees was determined based on the OOB error and it was set to 500. Less number of trees would have been sufficient but using a large number of trees stabilizes the classification error. Furthermore, there is no penalty for using a large number of trees, other than computational resources. RF classification was performed using random forest package [117] in R software.

2.3. *Patient Study and Testing*

The models trained on phantom plaque data were tested on four images obtained from three patients, who had one or two soft plaques identified in their LADs. The patients, who were enrolled in a fully IRB and HIPAA compliant protocol, were scanned by fast switched DECT with prospective ECG triggering using 80kVp/140kVp, 715mA, 64x0.625 mm detector configuration, 0.35 rotation, and a pitch of 1 in Mayo Clinic Hospital, Phoenix. Axial images were constructed at 75% of the R-to-R interval using a FOV of 25cm and 'standard' kernel with image thickness and increment of 0.625mm. While one of the patients received Visipaque 320 at 4 cm^3/sec, the other two received Omnipaque 350 at 5 cm^3/sec. Data was transferred to a GE AW workstation with GSI computational tools for providing 1) a range of monochromatic X-ray (40 to 140 keV) images, and 2) material basis pairs images (Water/Iodine, Calcium/Water, Calcium/Iodine).

Manually segmented soft plaques on patients' images produced 281 voxels. For each voxel, 17 pixel values corresponding to the same anatomical position were recorded from monochromatic X-ray and material basis pairs images as in phantom study. The features used for ANN and SVM models were scaled to have a mean of 0 and standard deviation of 1. Scaling of the features was not necessary for the RF model since the RF algorithm is scale invariant. Each of the voxels were classified as either being fibrous or lipid based on the trained SVM, ANN and RF models on phantom data.

3. Results

3.1. *Phantom Study and Training*

Cross validation was used to assess the prediction accuracy of the models on phantom data. Average error rates over the 10 replicates of 10-fold cross validation are summarized

in Table 2 for each model. Class predictions were also determined by majority voting approach. The feature importance measure from the RF model showed that pixel values from monochromatic X-ray images in the range of 50 to 110keV and Calcium(Iodine) image composed 80% of the predictive power.

	ANN	**SVM**	**RF**	**Majority**
Fibrous Class Error	6.10%	3.50%	5.08%	3.61%
Lipid Class Error	8.94%	8.52%	6.47%	7.25%
Total Error	7.36%	5.74%	5.70%	5.23%

TABLE 2. Average error rates over the 10 replicates of 10-fold cross validation for phantom data classification.

3.2. *Patient Study and Testing*

The three patients' data used for testing had six soft plaques generating a total of 281 voxels. Each of the voxels were classified as either being lipid or fibrous based on the ANN, RF and SVM models trained on the phantom data. The number of the pixels classified as either being fibrous or lipid on each image by the three classifiers and using majority voting approach can be found in Table 3.

		ANN	**SVM**	**RF**	**Majority**
Patient 1	*Fibrous*	36	39	73	45
	Lipid	109	106	72	100
Patient 2 / IM 1	*Fibrous*	30	39	64	45
	Lipid	46	37	12	31
Patient 2 / IM 2	*Fibrous*	14	18	27	19
	Lipid	26	22	13	21
Patient 3	*Fibrous*	7	9	11	10
	Lipid	13	11	9	10

TABLE 3. Classified pixel numbers as either being fibrous or lipid on each patient image by each method. Note that there were two images from patient 2. Total number of classified pixels was 281.

The monochromatic 70keV axial image zoomed in on the LAD of one of the patients and class predictions of the segmented voxels are shown in Figure 25 for illustrative purposes. The blue color indicates the voxels predicted as fibrous and the red color indicates the voxels predicted as lipid. The class predictions of the majority voting approach are illustrated in the bottom right of Figure 25. In Figure 26, pixel values of predicted fibrous and lipid voxels by three classifiers and majority voting approach on material basis pairs images (Calcium/Iodine) combined with phantom fibrous and lipid plaque data are shown. The boxplots produced using 11 monochromatic X-ray image (40keV-140keV) CT values of fibrous and lipid class predictions by ANN, SVM, RF and majority voting approach are shown in Figures 27 and 28. On each box, central line shows the median, the edges of the box are the 25th and 75th percentiles, whiskers show the most extreme data points which are not considered as outliers, and the outliers are plotted individually.

4. Discussion

4.1. *Our Findings*

The purpose of this study was to determine whether supervised learning approaches can characterize non-calcified atherosclerotic plaque components using pixel values from DECT monochromatic X-ray (40keV-140keV) and material basis pairs images (Water/Iodine, Calcium/Water, Calcium/Iodine) as features since single pixel value might not be informative enough to separate fibrous from lipid. The selected supervised learning approaches were ANN, SVM and RF. Supervised learners were trained on pixel values recorded from fabricated phantom fibrous and lipid plaque images. Recorded phantom plaque pixel values from different image types also showed that single threshold pixel value (HU or mg^3) can not be determined to separate fibrous from lipid, see Figure 24. Super-

vised learning considers the interaction of the pixel values which might be important for precise classification of lipid and fibrous.

Cross validation was used to assess the prediction accuracy of the models on phantom data. Average error rates over the 10 replicates of 10-fold cross validation were found to be 7.36%, 5.74%, 5.70% and 5.23% for ANN, SVM, RF and majority voting approach respectively. The classification accuracies of the three classifiers on phantom data were not significantly different from each other. The RF and SVM provided the best classification results for lipid and fibrous class respectively, see Table 2.

The models trained on phantom plaque data were tested on four images obtained from three patients, who had one or two soft plaques identified by an expert before. Manually segmented soft plaques on patients' images produced 281 voxels which were classified as either being fibrous or lipid. The pixel values of classified voxels recorded from monochromatic X-ray images were used to produce the boxplots, see Figures 27 and 28. Although the distribution of measured fibrous and pixel values showed substantial overlap on images reconstructed at single keV, the mean pixel values of fibrous voxels decreased from low keV to mid keV whereas the mean pixel values of lipid voxels did not show significant difference. Feature importance measure from RF model trained on phantom data confirms this since it revealed that image data at high keV were less predictive compared to mid and low keV. The pixel values of patient and phantom data recorded from Calcium/Iodine basis pairs images were plotted in Figure 26 for illustrative purposes. Using pixel values from two image types helps to create a boundary to separate fibrous from lipid.

4.2. *Comparison with Previous Studies*

Our results were compared with previous studies in terms of the CT density ranges for fibrous and lipid plaques. In 2001, Schroeder et al. performed a study where accuracy in detection of atherosclerotic coronary plaques with MSCT was evaluated by comparing it with the findings of intracoronary ultrasound (ICUS). Reported CT densities was 14$\pm$26 HU (-42 to + 47 HU) and 91$\pm$21 HU (61 to 112 HU) for soft and intermediate plaques respectively [22]. In 2004, again Schroeder et al. performed a study where reliability of differentiating coronary plaque morphology using contrast-enhanced MSCT was evaluated by comparing it with the histopathological findings. Mean CT densities were reported as 42$\pm$22 HU for lipid-rich plaques and 70$\pm$21 HU for intermediate plaques [20]. In 2007, Pohle et al. performed a study where CT attenuation of non-calcified plaques by MDCT was investigated in comparison to IVUS. The mean CT attenuation corresponding to lipid-rich plaque and fibrous plaques were reported as 58$\pm$43 HU (-39 to +167 HU) and 121$\pm$43 HU (60 to 201 HU) respectively [25]. In 2009, Brodoefel et al. performed a study where accuracy of dual-source CT in the characterization of non-calcified plaque was compared with virtual histology intravascular. Pre-defined cut-off CT values were used to measure the plaque volumes. The HU value settings were -150 to 60 HU for lipid plaque and 61 to 149 HU for fibrous plaque. It has been reported that HU based analysis performed an accurate quantification of non-calcified plaque [30]. The effective energy of the standard conventional 120kVp CT imaging has been reported to be about 67keV [97]. In our study, the CT density range for fibrous and lipid plaque was found to be from 29 to 386 HU with a mean of 194 HU and -165 to 267 HU with a mean of -5 HU on monochromatic 70keV patient image data respectively based on majority voting approach. The upper bound of the

HU range was found to be larger than reported HU values for fibrous plaque. The potential reasons may be:

- the manual selection of an internal border between the plaque area and the contrast enhanced vessel lumen. Due to similar attenuation values, contrast enhanced lumen may have been classified as fibrous plaque.
- the influence of near presence of calcification through beam hardening and partial volume effects.
- the different contrast flow rates and iodine concentration. An earlier study has shown that luminal density affects the absolute HU of fibrous plaques [24].

The highest CT value of pixels that were predicted as lipid was 267 HU. The highest CT value coming after 267 HU was 180 HU which correlates with previously reported upper bound of CT density range of lipid plaque. In addition, the lower bound of the HU range was found to be smaller for lipid plaque than some of the reported findings. The potential reason may be the manual segmentation of outer border. This may have caused epicardial fat to be classified as lipid plaque due to similar attenuation values. Attenuation of body fat has been reported to be in the range of -250 to -50 HU [118]. Due to contrast enhanced examinations, attenuation of lipid plaque is increased in coronary arteries.

4.3. *Limitations*

The limitation of this study is that there was no histopathological findings of the patient plaques. Although the findings were within comparable ranges with the previously published data on density measurements, predicted class of plaques need to be confirmed with histopathological findings. The small number of observations is the other limitation

of this study. Investigation with additional patient population may yield different mean CT densities. Reproducibility of the results needs confirmation in further studies.

5. Conclusion

Overlap between CT attenuations measured in lipid and fibrous plaques shows that the mean density or HU range might not be an appropriate measure to characterize plaque composition. Therefore, supervised learning approaches were explored as a more advanced mathematical analysis to use additional information provided by DECT. Pixel values from 11 monochromatic X-ray images and 6 material basis pairs images were provided as features to supervised learning algorithms. This way, the interaction of the pixel values from different image types was taken into consideration. The results demonstrated that trained models on phantom fibrous and lipid data separated lipid from fibrous plaques. The mean CT densities of predicted lipid and fibrous plaques are within comparable ranges with the previously published studies. The clinical relevance of this study requires further investigation in larger patient populations with histopathological findings.

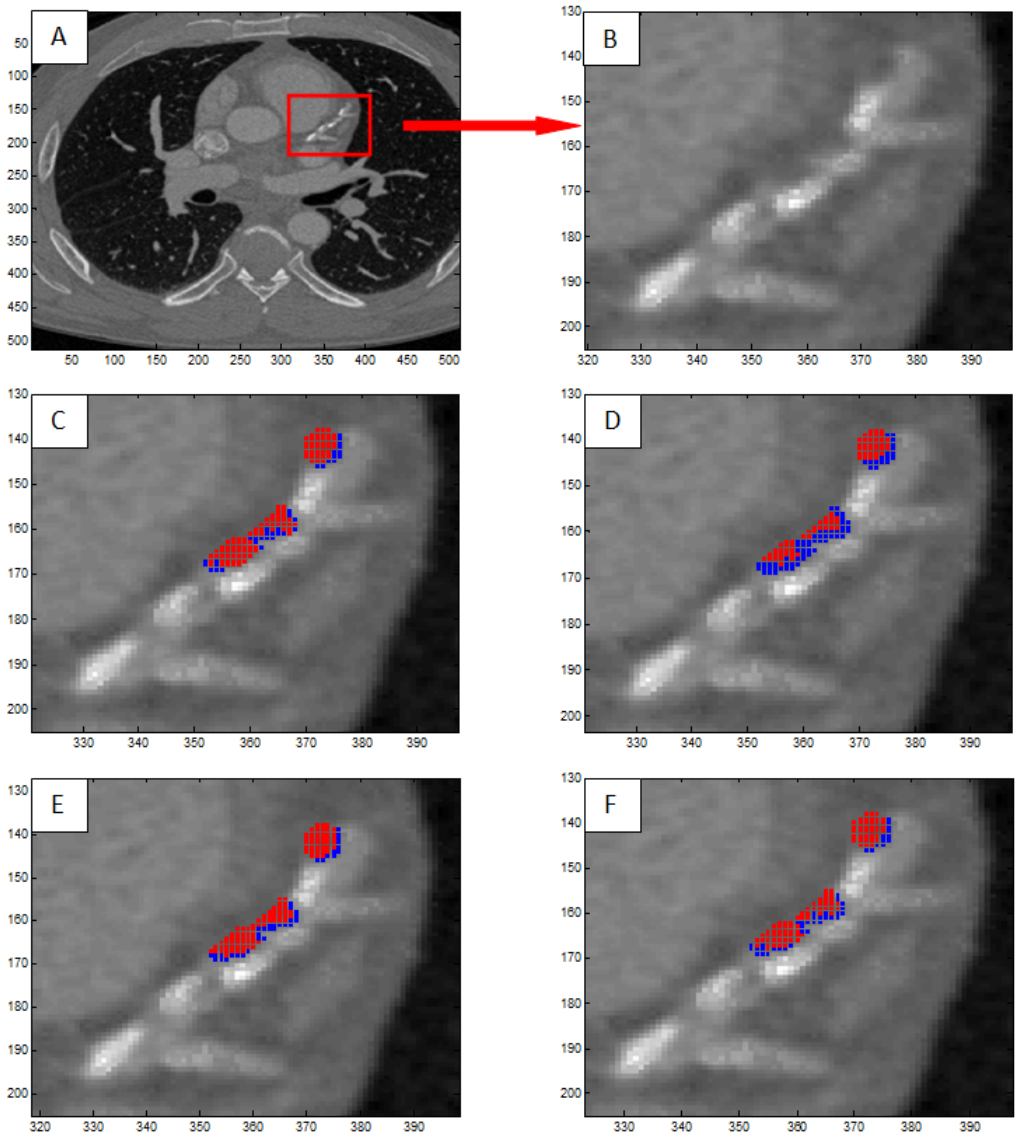

Figure 25. A: Monochromatic 70keV image with iodine contrast administered. LAD is located. B: Enlarged image of LAD. C, D, E, F: Voxels marked with red are predicted as lipid and voxels marked with blue are predicted as fibrous. C, D, E: Classification methods are ANN, RF and SVM respectively. F: Class predictions were determined using majority voting approach that combined three classifier predictions.

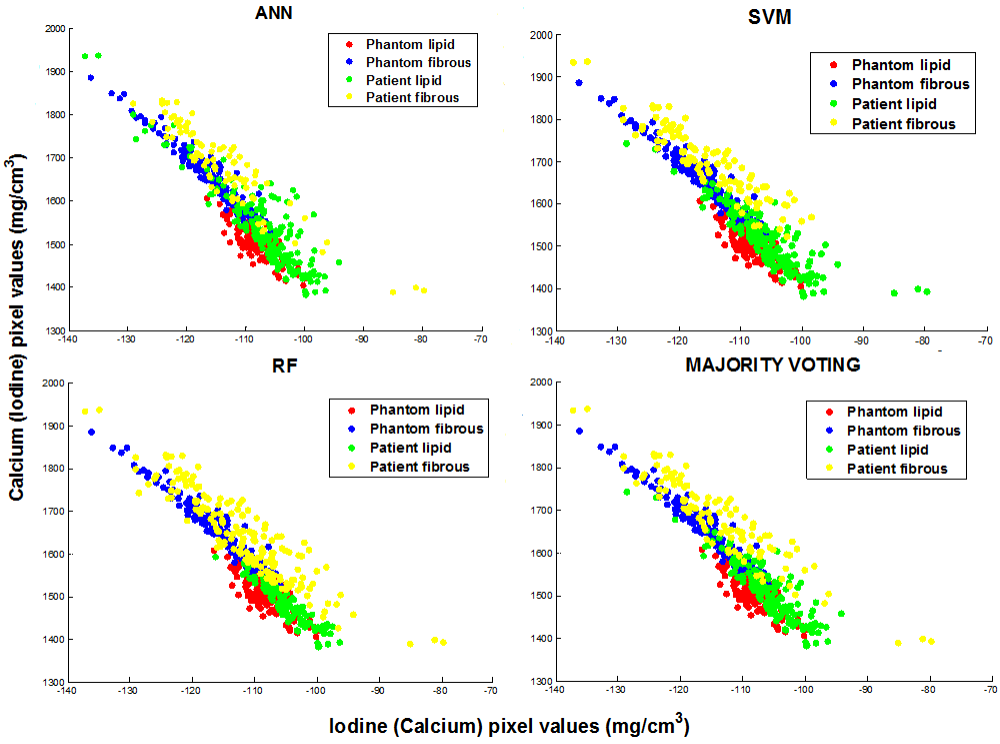

Figure 26. The plots show the predicted fibrous and lipid voxel pixel values on Calcium/Iodine basis pairs images combined with phantom lipid and fibrous plaque data. (y-axis shows the recorded pixel values on Calcium(Iodine) images whereas x-axis shows the recorded pixel values on Iodine(Calcium) images.

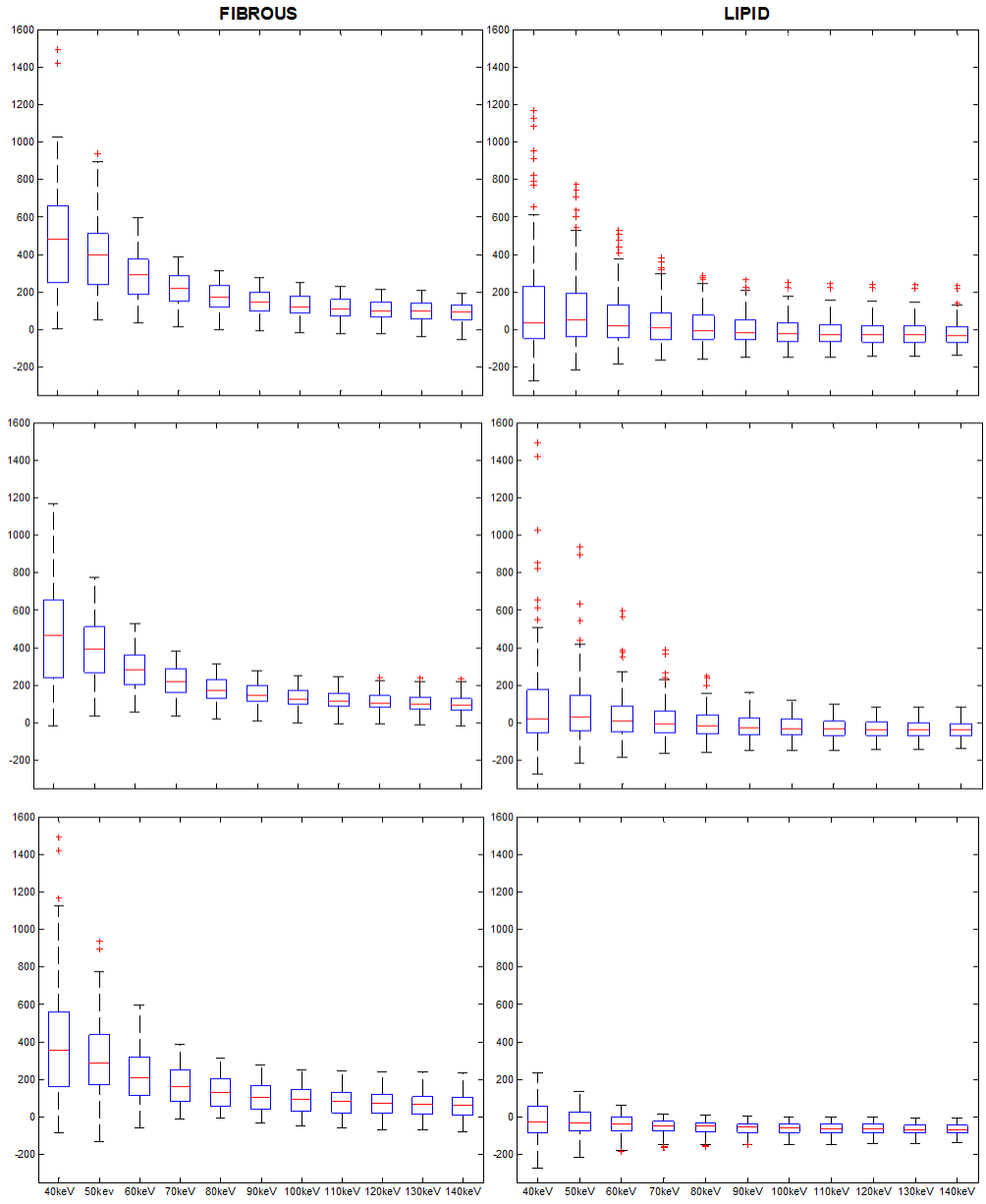

Figure 27. The left column illustrates the boxplots of 11 monochromatic image CT values of predicted fibrous voxels. The right column illustrates the boxplots of 11 monochromatic image CT values of predicted lipid voxels. Classification algorithms are ANN, SVM and RF respectively from top to bottom.

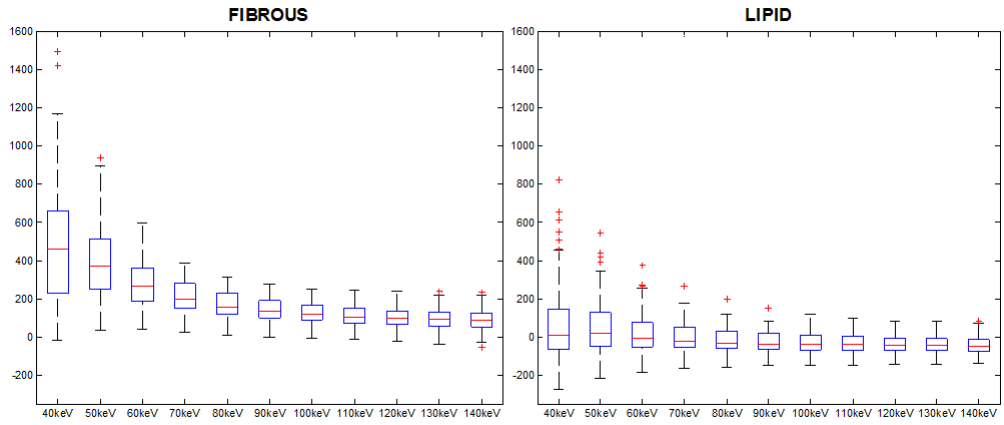

Figure 28. The left figure illustrates the boxplots of 11 monochromatic image CT values of predicted fibrous voxels by majority voting approach. The right figure illustrates the boxplots of 11 monochromatic image CT values of predicted lipid voxels by majority voting approach.

CHAPTER 6

CORONARY ATHEROSCLEROTIC PLAQUE CLASSIFICATION BY DUAL ENERGY COMPUTED TOMOGRAPHY

1. Introduction

Coronary artery disease (CAD) remains the leading cause of death globally [1,2]. Composition of plaque that builds up on the inside of the coronary artery wall plays an important role in the acute clinical events. Early detection and characterization of coronary artery plaques through non-invasive imaging techniques would allow a better risk stratification of the disease and follow-up of patients at risk.

The potential of computed tomography (CT) has made CT a promising non-invasive modality for coronary artery disease assessment. It has been shown that contrast enhanced CT imaging allows the visualization of coronary arteries with a reliable assessment of coronary artery stenosis [10, 11]. The detection of large calcium deposits in coronary arteries is possible due to a larger prevalence of multislice CT (MSCT) and its high correlation with electron beam CT (EBCT) for detection and quantification of coronary calcification [12–16]. The recently developed technology of MSCT has the potential to identify and characterize the non-calcified coronary atherosclerotic plaques [17–27]. Considering that radiologists examine hundreds of images every day, automatic analysis of images from medical imaging modalities is highly desirable in order to increase the productivity of radiologists. In medical image analysis, texture information is important for capturing the content. Gray-level information present in the images is used to capture the content of CT images however characterization of non-calcified plaques and separation of contrast enhanced lumen from calcified plaques are not possible with gray-level information alone due to their overlapping CT density ranges. Textural features are used in medical image clas-

sification and are expected to be homogenous and consistent across multiple slices for the same tissue [119, 120].

The purpose of this study is to achieve automatic classification of coronary artery plaques as lipid, fibrous and calcium on contrast enhanced 70keV monochromatic X-ray images obtained by fast-switched DECT. DECT derived monochromatic X-ray images suffer far less from the blooming artifact. The reason for choosing 70keV monochromatic image was due to the feature importance measure from the random forest model trained to classify fibrous and lipid in Chapter 5. The pixel values from 70keV monochromatic X-ray images had the largest predictive power. This study proposes features extraction and selection strategies for a classification of calcium, fibrous, lipid plaques or contrast enhanced lumen. The features extracted to be used by learning algorithms included pixel and region based features. Pixel based features were the pixel values and four moments (mean, variance, skewness and kurtosis) and entropy evaluated at different neighborhood sizes. Region based features were the texture characteristics derived from co-occurrence matrices. Co-occurrence matrices with three different gray-levels for eight angular directions were calculated for each pixel within different sized neighborhoods centered on that pixel. High dimension of features was reduced by feature selection preprocessing step. The feature importance measures from the random forest (RF) model were used to illustrate the predictive power of 597 features. Nine features out of 597 features composed 80% of the predictive power and were used by learning algorithms. Support vector machines, artificial neural networks and random forests were considered as the learning algorithms because of their known success in classification [102]. Training data was obtained from previously classified patient images in Chapter 5. Prediction accuracy of the three models was assessed

by cross validation applied on the training data and by testing on other patient images of which plaque locations were previously marked.

2. Materials and Methods

The proposed system consisted of three stages: 1)Vessel segmentation; 2)Feature extraction; and 2) Classification. Figure 29 illustrates the overview of the proposed system. First, region of interests were segmented manually. Second, pixel and region based features were extracted from the manually segmented region. While working with the training data, feature extraction stage also involved the selection of important features. Finally, three supervised learning approaches were utilized in order to classify each pixel.

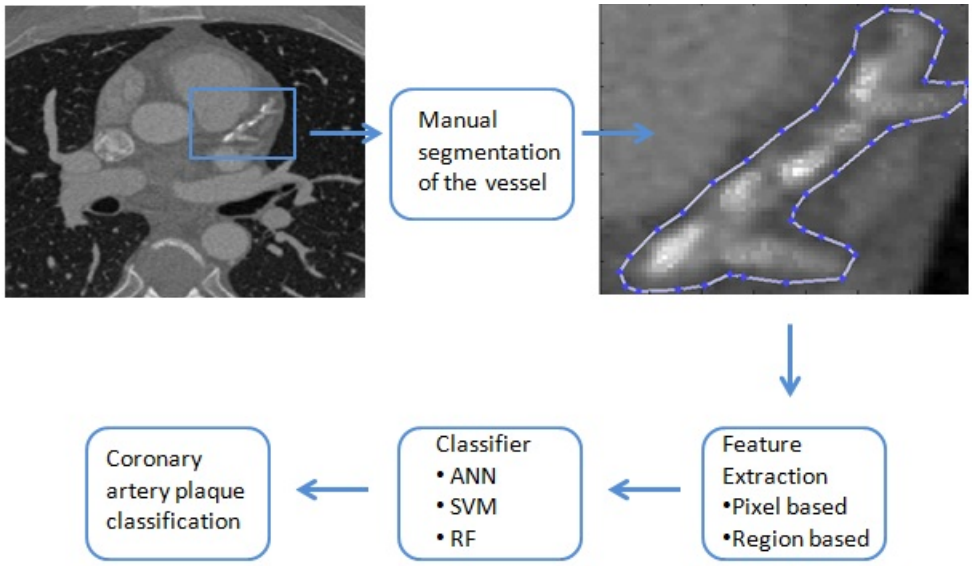

Figure 29. Proposed CAD system for coronary plaque classification

The classified patient data in Chapter 5 was used for training in this study. In addition to previously classified 127 pixels as either being fibrous (54) or lipid (73) on the patient data, 56 pixels of calcium and 53 pixels of contrast mixed lumen were added to the training data.

2.1. *Images Acquisition*

The patients, who were enrolled in a fully HIPAA and IRB compliant protocol, were scanned by fast switched DECT with prospective ECG triggering using 80kVp/140kVp, 715mA, 64x0.625 mm detector configuration, 0.35 rotation, and a pitch of 1. Axial images were constructed at 75% of the R-to-R interval using a FOV of 25cm and 'standard' kernel with image thickness and increment of 2.5mm. While one of the patients received Visipaque 320 at 4 cm^3/sec, the other two received Omnipaque 350 at 5 cm^3/sec. Data was transferred to a GE AW workstation with GSI computational tools for providing monochromatic X-ray (70keV) images. In order to identify the region of interest (ROI) on cardiac images, the coronary arteries were segmented manually by using MatLab computing software (The MathWorks, Natick).

2.2. *Feature Extraction*

For each ROI, pixel based and region based features were extracted comprising 597 dimensional feature vector. Before extracting the features, intensity of the cardiac images were mapped into 256 gray levels (0-255).

2.2.1. *Pixel based feature extraction.* Pixel based features included the pixel values and four moments (mean, variance, skewness and kurtosis) and entropy evaluated at different neighborhood sizes. In order to find the optimal neighborhood size, four moments and entropy were calculated at 3, 5, 7 and 9 neighborhood sizes.

2.2.2. *Region based feature extraction.* The texture characteristics were derived from eight texture features calculated from co-occurrence matrices of the ROI [121]. The idea of co-occurrence matrix is to keep the track of all the pixel-pair counts. By counting all

pixel pairs separated by displacement vector, d with gray level intensities i and j along an angular direction, θ, co-occurrence matrix was created as described in Figure 30. Co-occurrence matrix contains information about how pixel intensities with a certain position in relation to each other occur together.

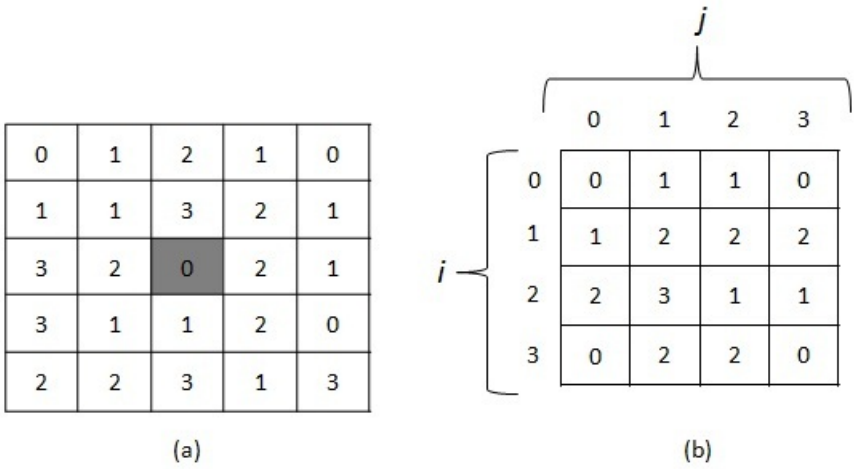

Figure 30. (a) 5X5 neighborhood around the corresponding pixel with 4 gray levels. (b) Co-occurrence matrix at d=1, θ=0°

In this study, co-occurrence matrices were calculated for pixel distance of one and eight angular directions (0°, 45°, 90°, 135°, 180°, 225°, 270° and 315°). The number of distinct gray levels of calculated co-occurrence matrices were 8, 16 and 32. The neighborhood sizes used to calculate the co-occurrence matrix for the corresponding pixel were set to 5, 7 and 9. Once 72 co-occurrence matrices were calculated for each pixel, eight Haralick texture features (energy, contrast, homogeneity, sum average, variance, maximum probability, inverse difference moment, cluster tendency) were calculated by the following equations [121] in which P_{ij} represented the normalized elements of co-occurrence matrices.

Energy measuring the occurrence of repeated pair within the image was calculated as:

$$\sum_{i}^{M}\sum_{j}^{N} P_{ij}^{2} \tag{6.1}$$

Contrast measuring the local contrast within the image was calculated as:

$$\sum_{i}^{M}\sum_{j}^{N} (i-j)^{2} P_{ij} \tag{6.2}$$

Homogeneity measuring the local homogeneity within the image was calculated as:

$$\sum_{i}^{M}\sum_{j}^{N} \frac{P_{ij}}{|i-j|};\ i \neq j \tag{6.3}$$

Sum average measuring the average of the gray-level within the image was calculated as:

$$\frac{1}{2}\sum_{i}^{M}\sum_{j}^{N} (iP_{ij} + jPij) \tag{6.4}$$

Variance measuring the gray-level distribution was calculated as:

$$\frac{1}{2}\sum_{i}^{M}\sum_{j}^{N} ((i-\mu_r)^{2} P_{ij} + (j-\mu_c)^{2} P_{ij}) \tag{6.5}$$

Maximum probability determining the maximum frequency in which all pixel pairs within the image was calculated as:

$$Max_{i,j}^{M,N} P_{ij} \tag{6.6}$$

Inverse difference moment measuring the smoothness of the image was calculated as:

$$\sum_{i}^{M}\sum_{j}^{N} \frac{P_{ij}}{1+(i-j)^{2}} \tag{6.7}$$

Cluster tendency measuring the grouping of pixels that have similar gray-level values was calculated as:

$$\sum_{i}^{M}\sum_{j}^{N} (i-\mu_r+j-\mu_c)^{2} P_{ij} \tag{6.8}$$

where μ_r and μ_c were the means of row and column defined as:

$$\mu_r = \sum_{i}^{M}\sum_{j}^{N} iP_{ij},\ \mu_c = \sum_{i}^{M}\sum_{j}^{N} jP_{ij} \tag{6.9}$$

2.3. *Feature Selection*

In this study high dimension of features that might have potential information were extracted. Feature selection which is a preprocessing step to machine learning was applied to remove irrelevant features and to increase learning accuracy [122]. The feature importance measures from the RF model were used to illustrate the predictive power of 597 features. Nine features out of 597 features composed 80% of the predictive power. These features are shown in Table 4 respectively. Pixel values had the largest predictive power.

	Feature	Neighborhood size	Gray level	Angular direction
1	Pixel value	N/A	N/A	N/A
2	Mean	3	N/A	N/A
3	Mean	5	N/A	N/A
4	Mean	7	N/A	N/A
5	Sum average	7	8	315 °
6	Sum average	7	32	135 °
7	Energy	9	32	0 °
8	Energy	9	32	180 °
9	Sum average	9	32	135 °

TABLE 4. Selected features based on importance measures from RF model respectively. N/A: Not applicable

2.4. *Parameters Settings For Selected Algorithms*

The classification algorithms and the performance evaluation performed in Chapter 5 were followed in this study. Selected nine features by importance measures from the RF model were used to train classifiers. MatLab computing software (The MathWorks, Natick) was used for back-propagation ANN training with the Levenberg-Marquardt algorithm; RF

classification was performed using random forest package [117] in R software; and support vector classifier by Weka [123] was used for SVM classification. The parameters settings for each algorithm providing the minimum 10-fold cross validation error rates are shown in Table 5.

ANN	
Size of hidden layer	*5*
Size of output layer	*4*
Transfer function for hidden layer	*Sigmoid function*
Transfer function for output layer	*Linear function*
Performance function	*Mean sum of squares of the errors*
SVM	
Kernel function	*RBF*
Gamma	*30*
Cost parameter	*10*
RF	
Number of trees	*1000*
Number of features selected at each split	*24*

TABLE 5. Parameters settings for each classification algorithm providing the minimum 10-fold cross validation error rate

3. Results

Cross validation was used to assess the prediction accuracy of the three models on the training data. Assessment of agreement between predictions and actual classes over 10 replicates of 10-fold cross validation are shown in the classification table, see Table 6. Error rates were found to be 0.13%, 1.9% and 1.8% of the total respectively for RF, SVM and ANN trained models.

The three models trained on 236 pixels collected from the patient data were tested on the data collected from three patients. Testing was performed on five images that had calcium and soft (non-calcified) plaques which were marked previously by an expert. ROIs on patient images covered the left main artery (LM), LM bifurcation and LAD. The pixels

RF	***Fibrous***	***Lipid***	***Calcium***	***Contrast***
Fibrous	53.8	0.2	0	0
Lipid	0.1	72.9	0	0
Calcium	0	0	56	0
Contrast	0	0	0	53

SVM	***Fibrous***	***Lipid***	***Calcium***	***Contrast***
Fibrous	51	2.8	0	0.2
Lipid	1.3	71.7	0	0
Calcium	0	0	56	0
Contrast	0.1	0	0	52.9

ANN	***Fibrous***	***Lipid***	***Calcium***	***Contrast***
Fibrous	51.9	2.1	0	0
Lipid	2	71	0	0
Calcium	0	0	56	0
Contrast	0	0.1	0	52.9

TABLE 6. The classification table describing the agreement between the actual and the predicted classes of the pixels based on RF, SVM and ANN trained models on patient data. The sum of rows equal to the recorded lipid, fibrous, calcium plaque or contrast enhanced lumen pixels whereas the sum of columns equal to the predicted classes. Incorrectly classified pixels are 0.13%, 1.9% and 1.8% of the total respectively for RF, SVM and ANN trained models.

found in manually segmented ROIs were classified as either being calcium, fibrous, lipid plaque or contrast enhanced lumen. The monochromatic 70keV patient axial images with their zoomed in on ROIs are illustrated in Figures presented in Appendix A. The total number of pixels classified on each image are presented in Table 7. Table 7 also presents the number of pixels for which there was agreement between the predicted classes by the three classifiers.

The class predictions for which there was agreement between the three classifiers were used to show the detected plaques on images. The Figures 31 - 35 illustrates the ROIs on which the plaques are marked based on expert opinion. The plaques marked with a green circle were predicted as calcium and the plaques marked with a yellow circle were predicted

	P1	P2 / IM1	P2 / IM2	P3 / IM1	P3 / IM2
Total # of pixels classified	1180	1158	684	1098	991
All agreed	960	775	446	1087	965
RF and SVM agreed	1050	866	547	983	779
RF and ANN agreed	1028	874	466	893	751
SVM and ANN agreed	1006	873	540	873	709
Non agreed	16	95	3	11	26

TABLE **7.** First row displays the total number of pixels classified on each image. Second, third, fourth and fifth row display the number of agreement between the predicted classes of the pixels based on the three and the two trained models for each image. Last row displays the number of pixels for which there is no agreement between the predicted classes by three classifiers. P=Patient, IM=Image, the numbers coming after P and IM represent the patient and image ID.

as soft plaques (fibrous or lipid) by the expert. Figures 31 - 35 also illustrates the agreed class predictions by the three classifiers. The red color indicates the pixels predicted as lipid, the blue color indicates the pixels predicted as fibrous and the green color indicates the pixels predicted as calcium. The pixels predicted as contrast enhanced lumen were left blank.

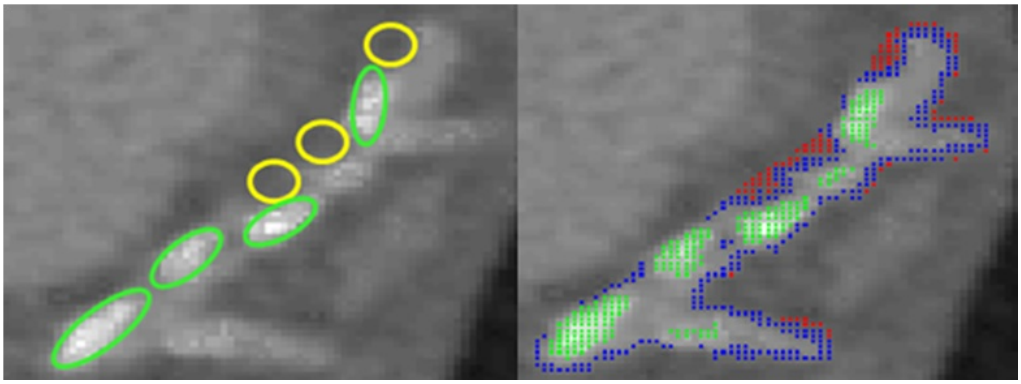

Figure 31. Left : Enlarged LAD image of P1. The plaques marked with a green circle were predicted as calcium and the plaques marked with a yellow circle were predicted as soft plaques (fibrous or lipid) based on expert opinion. Right: Illustration of agreed class predictions by the three classifiers on enlarged LAD image of P1. The red color indicates the pixels predicted as lipid, the blue color indicates the pixels predicted as fibrous and the green color indicates the pixels predicted as calcium. The pixels predicted as contrast enhanced lumen were left blank. P=Patient, the numbers coming after P represent the patient ID.

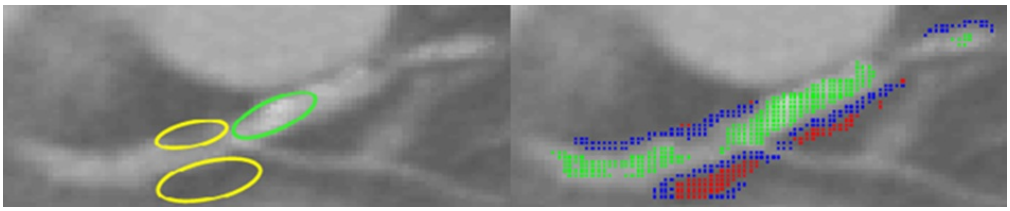

Figure 32. Left : Enlarged LAD image of P2 / IM1. The plaques marked with a green circle were predicted as calcium and the plaques marked with a yellow circle were predicted as soft plaques (fibrous or lipid) based on expert opinion. Right: Illustration of agreed class predictions by the three classifiers on enlarged LAD image of P2 / IM1. The red color indicates the pixels predicted as lipid, the blue color indicates the pixels predicted as fibrous and the green color indicates the pixels predicted as calcium. The pixels predicted as contrast enhanced lumen were left blank. P=Patient, IM=Image, the numbers coming after P and IM represent the patient and image ID.

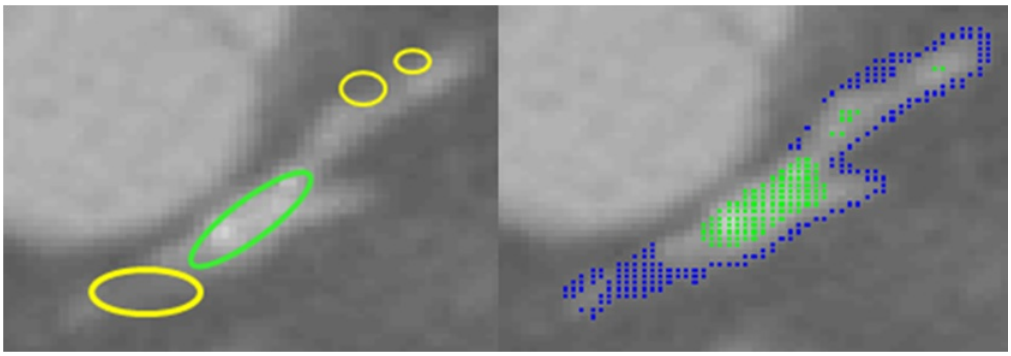

Figure 33. Left : Enlarged LAD image of P2 / IM2. The plaques marked with a green circle were predicted as calcium and the plaques marked with a yellow circle were predicted as soft plaques (fibrous or lipid) based on expert opinion. Right: Illustration of agreed class predictions by the three classifiers on enlarged LAD image of P2 / IM2. The red color indicates the pixels predicted as lipid, the blue color indicates the pixels predicted as fibrous and the green color indicates the pixels predicted as calcium. The pixels predicted as contrast enhanced lumen were left blank. P=Patient, IM=Image, the numbers coming after P and IM represent the patient and image ID.

Classified five images obtained from three patients produced 4233 pixels which were classified as either being calcium, fibrous, lipid plaque or contrast enhanced lumen. Based on agreed class predictions by the three classification algorithms 1092 of them were classified as calcium; 1186 of them were classified as contrast enhanced lumen; 1298 of them

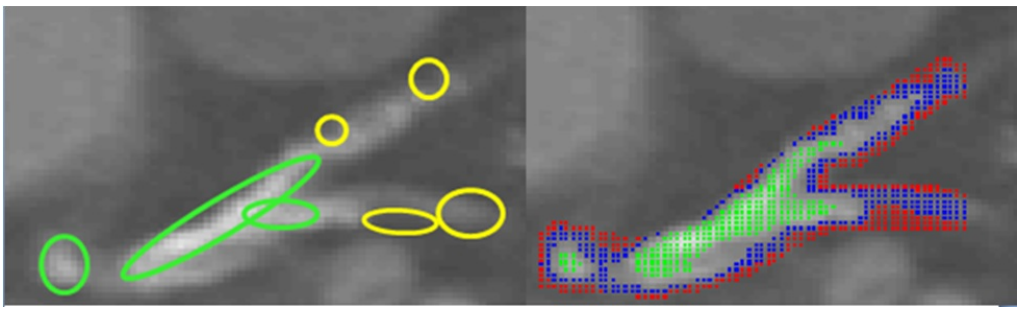

Figure 34. Left : Enlarged LAD image of P3 / IM1. The plaques marked with a green circle were predicted as calcium and the plaques marked with a yellow circle were predicted as soft plaques (fibrous or lipid) based on expert opinion. Right: Illustration of agreed class predictions by the three classifiers on enlarged LAD image of P3 / IM1. The red color indicates the pixels predicted as lipid, the blue color indicates the pixels predicted as fibrous and the green color indicates the pixels predicted as calcium. The pixels predicted as contrast enhanced lumen were left blank. P=Patient, IM=Image, the numbers coming after P and IM represent the patient and image ID.

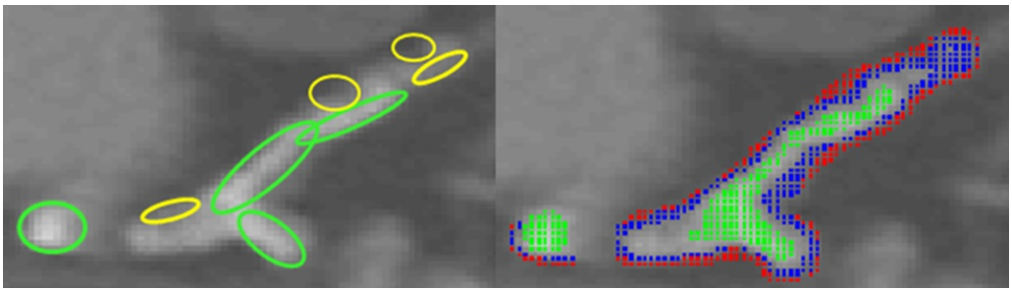

Figure 35. Left : Enlarged LAD image of P3 / IM2. The plaques marked with a green circle were predicted as calcium and the plaques marked with a yellow circle were predicted as soft plaques (fibrous or lipid) based on expert opinion. Right: Illustration of agreed class predictions by the three classifiers on enlarged LAD image of P3 / IM2. The red color indicates the pixels predicted as lipid, the blue color indicates the pixels predicted as fibrous and the green color indicates the pixels predicted as calcium. The pixels predicted as contrast enhanced lumen were left blank. P=Patient, IM=Image, the numbers coming after P and IM represent the patient and image ID.

were classified as fibrous; and 657 of them were classified as lipid. The boxplot produced using 70keV monochromatic image pixel values of four classes (calcium, contrast, fibrous and lipid) is shown in Figure 36. On each box, central line shows the median, the edges of the box are the 25th and 75th percentiles, whiskers show the most extreme data points

which are not considered as outliers, and the outliers are plotted individually. The mean CT density value on 70keV monochromatic image data was found to be 792±275 HU for calcium plaque pixels, 426±171 HU for contrast enhanced lumen pixels, 175±135 HU for fibrous plaque pixels and 9±92 HU for lipid plaque pixels.

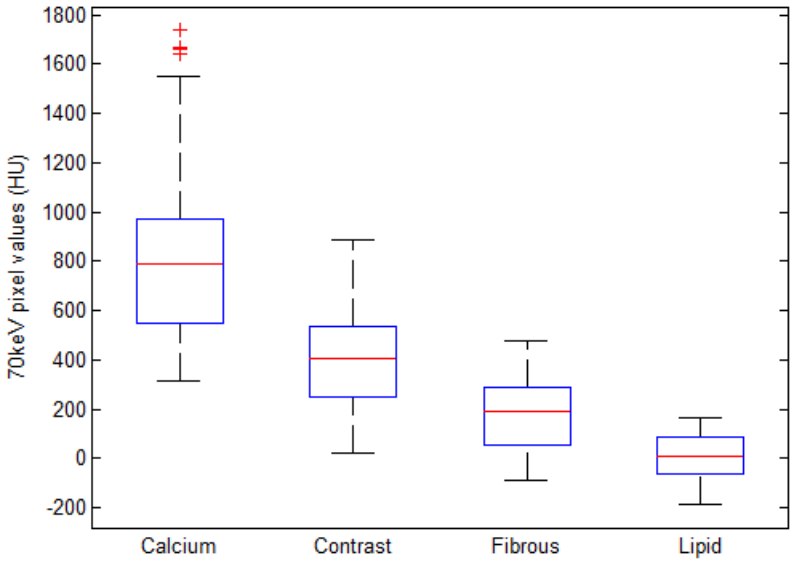

Figure 36. The boxplots of the predicted calcium, fibrous, lipid plaques and contrast enhanced lumen pixel values on 70keV monochromatic images. On each box, central line shows the median, the edges of the box are the 25th and 75th percentiles, whiskers show the most extreme data points which are not considered as outliers, and the outliers are plotted individually.

4. Discussion and Conclusion

Until now, multiple studies have shown significant differences between reported CT density units for lipid-rich, fibrous and calcified plaques. Different CT density unit cut-offs were proposed to characterize plaque composition or to separate contrast enhanced lumen from calcified plaques [22,25,30,31]. Substantial overlap between CT attenuations of tissue components does not make tissue characterization possible based on measurements of their

CT densities alone [25]. Therefore evaluation of composition of coronary artery plaques requires more advanced mathematical analysis of CT attenuation within the plaques.

In this study, supervised learning approaches were proposed for automatic classification of coronary artery plaques. Contrast enhanced 70keV monochromatic X-ray images of coronary arteries obtained by fast-switched DECT were classified as calcium, fibrous, lipid plaque and contrast enhanced lumen. Four moments and entropy evaluated at different neighborhood sizes; and texture characteristics derived from eight texture features calculated from co-occurrence matrices were provided as the input to the RF model. Before extracting the features, intensity of the cardiac images were mapped into 256 gray levels (0-255). High dimension of features was reduced by feature selection using feature importance measures from the RF model. Nine features composing 80% of the predictive power were provided as the input to the ANN, SVM and RF models. The three models were tested on five coronary artery images obtained from three patients. Soft and calcified plaques were marked on images by the expert before testing. Pixels were classified as either being calcium, fibrous, lipid plaque or contrast enhanced plaque based on agreed class predictions by the three methods. Previously marked plaques showed a good agreement with the classification results. The mean CT densities for calcium, fibrous, lipid plaque and contrast enhanced lumen were found to be 792$\pm$275 HU , 175$\pm$135 HU, 9$\pm$92 HU and 426$\pm$171 HU respectively. Our findings were compared with a previous study. In 2008. Brodoefel et al. performed a study where volumes of coronary plaques and lumen were obtained through use of pre-set HU cut-offs by contrast enhanced DECT scans. Calibrated HU ranges for fatty or fibrous plaque, lumen and calcification were -10-69, 70-158, 159-

436, 437+. Using these cut-offs good agreement of plaque volume with IVUS was achieved (*r=0.71, r=0.85*) but correlation of percentage plaque composition was poor [31].

Supervised learning algorithms trained with textural features and CT density values have shown the ability to classify contrast enhanced lumen, calcified and non-calcified plaques. The mean CT densities of predicted plaques and lumen were within comparable ranges with the previously published study however composition of soft plaques needs to be confirmed by histologic findings. The complex morphology of coronary plaques might result in lipid, fibrous and calcified components interlaced within each other, not only side by side. Spatial resolution of CT might not be sufficient to detect such a level complexity. On the other hand, it should be noted that the current study was limited by a small sample size. Investigation with additional patient population may yield different mean CT densities. Clinical relevance of this study requires further investigation with a larger patient population and histological findings.

CHAPTER 7

CONCLUSION AND FUTURE WORK

1. Conclusion

This dissertation proposed feature extraction, feature selection and learning strategies for supervised characterization of coronary atherosclerotic plaques. Overlap between the CT attenuations measured in plaque components and contrast enhanced lumen shows that the mean density or HU range might not be an appropriate measure to characterize plaque composition or separate contrast enhanced lumen from calcified plaques. Therefore, supervised learning approaches were explored as a more advanced mathematical analysis for a more precise classification of plaque components. Additional attenuation data provided by DECT and textural features extracted from monochromatic images were investigated as the inputs to the selected supervised learning approaches.

In my first study, I demonstrated one method for calcium quantification in contrast-enhanced examinations of the coronary arteries. Agatston score and Volume score are both used clinically in the assessment of risk in terms of calcification. They are currently obtained using 120kVp CT acquisitions without iodine contrast. Agatston scores from non-contrast conventional and contrast-enhanced conventional scans did not demonstrate sufficient correlation for calcium quantification on CT coronary angiograms, likely due to the poor separation of calcium and iodine. The purpose of this study was to evaluate a direct measure of calcium burden by using DECT during contrast enhanced coronary imaging, potentially eliminating the need for an extra non-contrast x-ray acquisition. I proposed a measure of calcium plaque burden that is comparable to true non-contrast CAC scoring using DECT material basis pair images. I selected calcium and iodine as basis materials to allow for the creation of 'virtual' non-contrast calcium images in which calcium content is preserved in the image. The method required determination of a threshold CT number to de-

tect the calcium carrying potential risk for adverse coronary events on virtual non-contrast images. Two approaches were investigated to determine the 130 HU threshold (minimum Agatston threshold) for DECT scoring. An in-vitro anthropomorphic phantom with 29 excised patient calcium plaques inserted was used for both a linear and a logistic regression analysis. An IRB approved in-vivo prospective study of six patients was also performed to be used for logistic regression analysis. The threshold found by logistic regression model to define the calcium burden on virtual non-contrast images detected the calcium carrying potential risk for adverse coronary events correctly. DECT calcium mass and volume scores obtained by using the determined threshold correlated with both conventional Agatston and volume scores.

My second study explored the use of additional attenuation data provided by DECT for plaque characterization. I proposed to provide pixel values recorded from DECT monochromatic X-ray and material basis pairs images as features for supervised learners, for a more precise classification of fibrous and lipid coronary plaques. Rupture of unstable atherosclerotic coronary plaque is known to be the cause of acute coronary syndrome. Vulnerability of atherosclerotic plaque has been related to a large lipid core covered by a fibrous cap. Non-invasive assessment of plaque characterization is necessary due to prognostic importance of early stage identification. In this study, the interaction of the pixel values from different image types was taken into consideration, as single pixel value might not be informative enough to separate fibrous from lipid. Organic phantom plaques scanned in a fabricated beating heart phantom were used as ground truth to train the three learners which were selected as ANN, SVM and RF. The results demonstrated that trained supervised learners on additional CT data provided by DECT were able to separate lipid from fibrous plaques. The

models trained on phantom plaque data were tested on patient images which had one or two soft plaques identified by an expert before. The mean CT densities of predicted lipid and fibrous plaques on patient data were within comparable ranges with the previously published studies.

The purpose of my third study was to achieve automatic segmentation of coronary arteries as lipid, fibrous, calcium plaque or contrast enhanced lumen on 70keV monochromatic X-ray images obtained by DECT. Until now, proposed CT density unit cut-offs were not sufficient enough to characterize plaque composition or to separate contrast enhanced lumen from calcified plaques. This study proposed feature extraction and selection strategies for automatic classification of coronary artery plaques. Four moments and entropy evaluated at different neighborhood sizes; and texture characteristics derived from eight texture features calculated from co-occurrence matrices were provided as the input to the RF model. Before extracting the features, intensity of the cardiac images were mapped into 256 gray levels (0-255). High dimension of features (597 features) was reduced by feature selection using feature importance measures from the RF model. Nine features composing 80% of the predictive power were provided as the input to the ANN, SVM and RF models. Training data was obtained from classified patient images in our previous study. Prediction accuracy of the three models was assessed by cross validation applied on the training data and by testing on other patient images of which plaque locations were previously marked. Supervised learning algorithms trained with textural features and CT density values have shown the ability to classify contrast enhanced lumen, calcified and non-calcified plaques. The mean CT densities of predicted plaques and contrast enhanced lumen were within comparable ranges with the previously published studies.

Accurate detection of coronary atherosclerotic plaque composition by CT remains difficult but the results showed that training supervised learners with properly selected features provides promising results for automatic characterization of coronary atherosclerotic plaques. Although mean CT densities of predicted composition of the plaques were within comparable ranges with the previously published studies, confirmation of soft plaque composition requires histopathologic findings which were not available to me during this study. Further refinements regarding reproducibility and ability to predict future coronary events are also required. Although I presented approaches that are effective for non-invasive characterization of coronary atherosclerotic plaques, there is potential to improve proposed approaches which is further discussed in next session.

2. Future Work

The approach presented in Chapters 5 used organic phantom plaques fabricated from LDPE and HDPE scanned by DECT as the ground truth to train the models. These plaques were fabricated based on the density values of lipid-rich and fibrous plaques. Proposed approach may be improved by considering postmortem tissue samples present in arterial plaques collected at autopsy to train the models. Furthermore, the upper bound of the HU range was found to be larger than the reported HU values for fibrous plaque. The potential reason may be the manual selection of the internal border between the plaque and the contrast enhanced lumen. Classification of contrast enhanced lumen as fibrous plaque might have increased the upper bound of the HU range. Including pixel values of contrast enhanced lumen to the training model and defining a third class may provide clear separation of lumen from fibrous plaques.

Our approach presented in Chapter 6 performed segmentation of outer borders of vessels manually. Manual segmentation of outer border might have caused epicardial fat pixels to be included in classification process and due to similar attenuation values, they might have classified as lipid. Classification of epicardial fat as lipid plaque might have resulted in lower mean CT density values. Automatic segmentation of outer border is possible [124] and it may improve classification of lipid plaque.

Finally, variations in contrast concentration and flow rate have a considerable effect on CT densities [24, 28]. Both approaches proposed Chapters in 5 and 6 may be improved by standardization of contrast administration.

REFERENCES

[1] "Cardiovascular disease (cvds)," http://www.who.int/mediacentre/factsheets/fs317/en/index.html, 2008, retrieved: May 21, 2012.

[2] "What is cardiovascular disease?" http://www.cvdf.org/, 2009, retrieved: May 21, 2012.

[3] M. Lipinski, D. Do, A. Morise, and V. Froelicher, "What percent luminal stenosis should be used to define angiographic coronary artery disease for noninvasive test evaluation?" *Annals of Noninvasive Electrocardiology*, vol. 7, no. 2, pp. 98–105, 2002. [Online]. Available: http://dx.doi.org/10.1111/j.1542-474X.2002.tb00149.x

[4] J. Longe and L. Fundukian, *The Gale Encyclopedia of Alternative Medicine*, ser. The Gale Encyclopedia of Alternative Medicine. Gale, 2008, no. v. 1-4. [Online]. Available: http://books.google.com/books?id=XzMLRwAACAAJ

[5] W. Moshage, S. Achenbach, and W. G. Daniel, "Novel approaches to the noninvasive diagnosis of coronaryartery disease," *Nephrology Dialysis Transplantation*, vol. 16, no. 1, pp. 21–28, 2001.

[6] J. A. Schaar, F. Mastik, E. Regar, C. A. den Uil, F. J. Gijsen, J. J. Wentzel, P. W. Serruys, and A. F. W van der Stehen, "Current diagnostic modalities for vulnerable plaque detection," *Current Pharmaceutical Design*, vol. 13, no. 10, pp. 995–1001, 2007.

[7] G. A. Rodriguez-Granillo, H. M. Garca-Garca, M. Valgimigli, S. Vaina, C. van Mieghem, R. J. van Geuns, M. van der Ent, E. Regar, P. de Jaegere, W. van der Giessen, P. de Feyter, and P. W. Serruys, "Global characterization of coronary plaque rupture phenotype using three-vessel intravascular ultrasound radiofrequency data analysis," *European Heart Journal*, vol. 27, no. 16, pp. 1921–1927, 2006.

[8] A. Nair, B. D. Kuban, E. M. Tuzcu, P. Schoenhagen, S. E. Nissen, and D. G. Vince, "Coronary plaque classification with intravascular ultrasound radiofrequency data analysis," *Circulation*, vol. 106, no. 17, pp. 2200–2206, 2002.

[9] J. Ge, F. Chirillo, J. Schwedtmann, G. Grge, M. Haude, D. Baumgart, V. Shah, C. von Birgelen, S. Sack, H. Boudoulas, and R. Erbel, "Screening of ruptured plaques in patients with coronary artery disease by intravascular ultrasound," *Heart*, vol. 81, no. 6, pp. 621–627, 1999.

[10] D. Ropers, U. Baum, K. Pohle, K. Anders, S. Ulzheimer, B. Ohnesorge, C. Schlundt, W. Bautz, W. G. Daniel, and S. Achenbach, "Detection of coronary artery stenoses with thin-slice multi-detector row spiral computed tomography and multiplanar reconstruction," *Circulation*, vol. 107, no. 5, pp. 664–666, 2003.

[11] M. H. K. Hoffmann, H. Shi, B. L. Schmitz, F. T. Schmid, M. Lieberknecht, R. Schulze, B. Ludwig, U. Kroschel, N. Jahnke, W. Haerer, H.-J. Brambs, and A. J. Aschoff, "Noninvasive coronary angiography with multislice computed tomography," *JAMA: The Journal of the American Medical Association*, vol. 293, no. 20, pp. 2471–2478, 2005.

[12] G. Mhlenbruch, J. E. Wildberger, R. Koos, M. Das, T. G. Flohr, M. Niethammer, C. Wei, R. W. Gnther, and A. H. Mahnken, "Coronary calcium scoring using 16-row multislice computed tomography: Nonenhanced versus contrast- enhanced stuides in vitro and in vivo," *Investigative Radiology*, vol. 40, pp. 148–154, 2005.

[13] C. R. Becker, T. Kleffel, A. Crispin, A. Knez, J. Young, U. J. Schoepf, R. Haberl, and M. F. Reiser, "Coronary artery calcium measurement," *American Journal of Roentgenology*, vol. 176, no. 5, pp. 1295–1298, 2001.

[14] C. Hong, C. R. Becker, U. J. Schoepf, B. Ohnesorge, R. Bruening, and M. F. Reiser, "Coronary artery calcium: absolute quantification in nonenhanced and contrast-enhanced multi-detector row CT studies." *Radiology*, vol. 223, no. 2, pp. 474–480, 2002.

[15] J. Groen, M. Greuter, R. Vliegenthart, C. Suess, B. Schmidt, F. Zijlstra, and M. Oudkerk, "Calcium scoring using 64-slice MDCT, dual source CT and EBT: a comparative phantom study," *The International Journal of Cardiovascular Imaging (formerly Cardiac Imaging)*, vol. 24, pp. 547–556, 2008.

[16] S. S. Halliburton, A. E. Stillman, and R. D. White, "Noninvasive quantification of coronary artery calcification: methods and prognostic value." *Cleveland Clinic Journal of Medicine*, vol. 69, pp. S6–S11, 2002.

[17] F. R. Joshi, A. C. Lindsay, D. R. Obaid, E. Falk, and J. H. Rudd, "Non-invasive imaging of atherosclerosis," *European Heart Journal Cardiovascular Imaging*, vol. 13, no. 3, pp. 205–218, 2012.

[18] J. E. van Velzen, J. D. Schuijf, F. R. de Graaf, G. Nucifora, G. Pundziute, J. W. Jukema, M. J. Schalij, L. J. Kroft, A. de Roos, J. H. C. Reiber, E. E. van der Wall, and J. J. Bax, "Plaque type and composition as evaluated non-invasively by MSCT angiography and invasively by vh ivus in relation to the degree of stenosis," *Heart*, vol. 95, no. 24, pp. 1990–1996, 2009.

[19] S. Voros, S. Rinehart, Z. Qian, P. Joshi, G. Vazquez, C. Fischer, P. Belur, E. Hulten, and T. C. Villines, "Coronary atherosclerosis imaging by coronary CT angiography: Current status, correlation with intravascular interrogation and meta-analysis," *J Am Coll Cardiol Img*, vol. 4, no. 5, pp. 537–548, 2011.

[20] S. Schroeder, A. Kuettner, M. Leitritz, J. Janzen, A. F. Kopp, C. Herdeg, M. Heuschmid, C. Burgstahler, A. Baumbach, M. Wehrmann, and et al., "Reliability of differentiating human coronary plaque morphology using contrast-enhanced multislice spiral computed tomography: a comparison with histology." *Journal Of Computer Assisted Tomography*, vol. 28, no. 4, pp. 449–454, 2004.

[21] T. Kitagawa, H. Yamamoto, J. Horiguchi, N. Ohhashi, F. Tadehara, T. Shokawa, Y. Dohi, E. Kunita, H. Utsunomiya, N. Kohno, and Y. Kihara, "Characterization of noncalcified coronary plaques and identification of culprit lesions in patients with acute coronary syndrome by 64-slice computed tomography," *J Am Coll Cardiol Img*, vol. 2, no. 2, pp. 153–160, 2009.

[22] S. Schroeder, A. F. Kopp, A. Baumbach, C. Meisner, A. Kuettner, C. Georg, B. Ohnesorge, C. Herdeg, C. D. Claussen, and K. R. Karsch, "Noninvasive detection and evaluation of atherosclerotic coronary plaques with multislice computed tomography," *Journal of the American College of Cardiology*, vol. 37, no. 5, pp. 1430–1435, 2001.

[23] S. Achenbach, F. Moselewski, D. Ropers, M. Ferencik, U. Hoffmann, B. MacNeill, K. Pohle, U. Baum, K. Anders, I.-k. Jang, W. G. Daniel, and T. J. Brady, "Detection of calcified and noncalcified coronary atherosclerotic plaque by contrast-enhanced, submillimeter multidetector spiral computed tomography," *Circulation*, vol. 109, no. 1, pp. 14–17, January 6/13, 2004.

[24] M. G. Dalager, M. Bottcher, A. Gratien, J. Thygesen, E. M. Pedersen, L. Dejbjerg, O. Gotzsche, and H. E. Botker, "Impact of luminal density on plaque classification by CT coronary angiography," *The International Journal of Cardiovascular Imaging*, vol. 27, pp. 593–600, 2011.

[25] K. Pohle, S. Achenbach, B. MacNeill, D. Ropers, M. Ferencik, F. Moselewski, U. Hoffmann, T. J. Brady, I. kyung Jang, and W. G. Daniel, "Characterization of

non-calcified coronary atherosclerotic plaque by multi-detector row CT: Comparison to ivus," *Atherosclerosis*, vol. 190, no. 1, pp. 174–180, 2007.

[26] K. Nikolaou, S. Sagmeister, A. Knez, E. Klotz, B. Wintersperger, C. Becker, and M. Reiser, "Multidetector-row computed tomography of the coronary arteries: predictive value and quantitative assessment of non-calcified vessel-wall changes," *European Radiology*, vol. 13, pp. 2505–2512, 2003.

[27] J. Hausleiter, T. Meyer, M. Hadamitzky, A. Kastrati, S. Martinoff, and A. Schomig, "Prevalence of noncalcified coronary plaques by 64-slice computed tomography in patients with an intermediate risk for significant coronary artery disease," *J Am Coll Cardiol*, vol. 48, no. 2, pp. 312–318, 2006.

[28] M. Barreto, P. Schoenhagen, A. Nair, S. Amatangelo, M. Milite, N. A. Obuchowski, M. L. Lieber, and S. S. Halliburton, "Potential of dual-energy computed tomography to characterize atherosclerotic plaque: ex vivo assessment of human coronary arteries in comparison to histology," *Journal of Cardiovascular Computed Tomography*, vol. 2, no. 4, pp. 234–242, 2008.

[29] H. Brodoefel, C. Burgstahler, M. Heuschmid, A. Reimann, F. Khosa, A. Kopp, S. Schroeder, C. D. Claussen, and M. E. Clouse, "Accuracy of dual-source CT in the characterisation of non-calcified plaque: use of a colour-coded analysis compared with virtual histology intravascular ultrasound," *British Journal of Radiology*, vol. 82, no. 982, pp. 805–812, 2009.

[30] H. Brodoefel, C. Burgstahler, A. Sabir, C.-S. Yam, F. Khosa, C. D. Claussen, and M. E. Clouse, "Coronary plaque quantification by voxel analysis: Dual-source MDCT angiography versus intravascular sonography," *American Journal of Roentgenology*, vol. 192, no. 3, pp. W84–W89, 2009.

[31] H. Brodoefel, A. Reimann, M. Heuschmid, I. Tsiflikas, A. Kopp, S. Schroeder, C. Claussen, M. Clouse, and C. Burgstahler, "Characterization of coronary atherosclerosis by dual-source computed tomography and hu-based color mapping: a pilot study," *European Radiology*, vol. 18, pp. 2466–2474, 2008.

[32] H. Zachrisson, E. Engström, J. Engvall, L. Wigström, Ö. Smedby, and A. Persson, "Soft tissue discrimination ex vivo by dual energy computed tomography," *European Journal of Radiology*, vol. 75, no. 2, pp. e124–e128, 2010.

[33] *Artery*. Encyclopaedia Britannica Online: Academic Edition, 2012, retrieved: May 25, 2012. [Online]. Available: http://www.britannica.com/EBchecked/topic/36874/artery

[34] *Atherosclerosis*. Encyclopaedia Britannica Online: Academic Edition, 2012, retrieved: May 22, 2012. [Online]. Available: http://www.britannica.com/EBchecked/topic/40908/atherosclerosis

[35] *Cardiovascular Disease*. Encyclopaedia Britannica Online: Academic Edition, 2012, retrieved: May 23, 2012. [Online]. Available: http://www.britannica.com.ezproxy1.lib.asu.edu/EBchecked/topic/720793/cardiovascular-disease.

[36] "The coronary arteries," http://www.texasheart.org/hic/anatomy/coroanat.cfm, 2011, retrieved: May 23, 2012.

[37] A. S. Go, D. Mozaffarian, V. L. Roger, E. J. Benjamin, J. D. Berry, W. B. Borden, D. M. Bravata, S. Dai, E. S. Ford, C. S. Fox, S. Franco, H. J. Fullerton, C. Gillespie, S. M. Hailpern, J. A. Heit, V. J. Howard, M. D. Huffman, B. M. Kissela, S. J. Kittner, D. T. Lackland, J. H. Lichtman, L. D. Lisabeth, D. Magid, G. M. Marcus, A. Marelli, D. B. Matchar, D. K. McGuire, E. R. Mohler, C. S. Moy, M. E. Mussolino, G. Nichol, N. P. Paynter, P. J. Schreiner, P. D. Sorlie, J. Stein, T. N. Turan, S. S. Virani, N. D. Wong, D. Woo, and M. B. Turner, "Heart disease and stroke statistics–2013 update a report from the american heart association." *Circulation*, vol. 127, no. 1, pp. 6–245, 2013.

[38] P. de Feyter, P. W. Serruys, K. Nieman, N. Mollet, F. Cademartiri, R. J. van Geuns, C. Slager, A. van der Steen, R. Krams, J. Schaar, P. Wielopolski, P. Pattynama, A. Arampatzis, A. van der Lugt, E. Regar, J. Ligthart, and P. Smits, "Imaging of coronary atherosclerosis and identification of the vulnerable plaque," *Netherlands Heart Journal*, vol. 11, no. 9, 2003.

[39] W. C. Little, M. Constantinescu, R. J. Applegate, M. A. Kutcher, M. T. Burrows, F. R. Kahl, and W. P. Santamore, "Can coronary angiography predict the site of a subsequent myocardial infarction in patients with mild-to-moderate coronary artery disease?" *Circulation*, vol. 78, pp. 1157–1166, 1988.

[40] M. Naghavi, M. Madjid, M. Khan, R. Mohammadi, J. Willerson, and S. Casscells, "New developments in the detection of vulnerable plaque," *Current Atherosclerosis Reports*, vol. 3, pp. 125–135, 2001, 10.1007/s11883-001-0048-1.

[41] Y. Uchida, F. Nakamura, T. Tomaru, T. Morita, T. Oshima, T. Sasaki, S. Morizuki, and J. Hirose, "Prediction of acute coronary syndromes by percutaneous coronary angioscopy in patients with stable angina," *American Heart Journal*, vol. 130, no. 2, pp. 195–203, 1995.

[42] B. D. MacNeill, H. C. Lowe, M. Takano, V. Fuster, and I.-K. Jang, "Intravascular modalities for detection of vulnerable plaque," *Arteriosclerosis, Thrombosis, and Vascular Biology*, vol. 23, no. 8, pp. 1333–1342, 2003.

[43] F. Prati, E. Regar, G. S. Mintz, E. Arbustini, C. Di Mario, I.-K. Jang, T. Akasaka, M. Costa, G. Guagliumi, E. Grube, Y. Ozaki, F. Pinto, P. W. Serruys, and for the Expert's OCT Review Document, "Expert review document on methodology, terminology, and clinical applications of optical coherence tomography: physical principles, methodology of image acquisition, and clinical application for assessment of coronary arteries and atherosclerosis," vol. 31, 2009.

[44] C. von Birgelen, W. Klinkhart, G. S. Mintz, A. Papatheodorou, J. Herrmann, D. Baumgart, M. Haude, H. Wieneke, J. Ge, and R. Erbel, "Plaque distribution and vascular remodeling of ruptured and nonruptured coronary plaques in the same vessel: an intravascular ultrasound study in vivo," *Journal of the American College of Cardiology*, vol. 37, no. 7, pp. 1864–1870, 2001.

[45] C. L. de Korte, G. Pasterkamp, A. F. W. van der Steen, H. A. Woutman, and N. Bom, "Characterization of plaque components with intravascular ultrasound elastography in human femoral and coronary arteries in vitro," *Circulation*, vol. 102, no. 6, pp. 617–623, 2000.

[46] W. Casscells, W. Vaughn, H. McAllister, J. Willerson, W. Casscells, J. Willerson, W. Casscells, B. Hathorn, M. David, W. Vaughn, H. McAllister, J. Willerson, T. Krabach, and G. Bearman, "Thermal detection of cellular infiltrates in living atherosclerotic plaques: possible implications for plaque rupture and thrombosis," *The Lancet*, vol. 347, no. 9013, pp. 1447–1449, 1996.

[47] P. R. Moreno, R. A. Lodder, K. R. Purushothaman, W. E. Charash, W. N. OConnor, and J. E. Muller, "Detection of lipid pool, thin fibrous cap, and inflammatory cells in human aortic atherosclerotic plaques by near-infrared spectroscopy," *Circulation*, vol. 105, no. 8, pp. 923–927, 2002.

[48] R. L. Wilensky, H. K. Song, and V. A. Ferrari, "Role of magnetic resonance and intravascular magnetic resonance in the detection of vulnerable plaques," *J Am Coll Cardiol*, vol. 47, no. 8, pp. C48–56, 2006.

[49] S. A. Schmitz, S. E. Coupland, R. Gust, S. Winterhalter, S. Wagner, M. Kresse, W. Semmler, and K. J. Wolf, "Superparamagnetic iron oxide-enhanced MRI of atherosclerotic plaques in watanabe hereditable hyperlipidemic rabbits," *Investigative Radiology*, vol. 35, no. 8, pp. 460–471, 2000.

[50] C. Yuan, W. S. Kerwin, M. S. Ferguson, N. Polissar, S. Zhang, J. Cai, and T. S. Hatsukami, "Contrast-enhanced high resolution MRI for atherosclerotic carotid artery tissue characterization," *Journal of Magnetic Resonance Imaging*, vol. 15, no. 1, pp. 62–67, 2002.

[51] M. V. McConnell, M. Aikawa, S. E. Maier, P. Ganz, P. Libby, and R. T. Lee, "Mri of rabbit atherosclerosis in response to dietary cholesterol lowering," *Arteriosclerosis, Thrombosis, and Vascular Biology*, vol. 19, no. 8, pp. 1956–1959, 1999.

[52] G. Helft, S. G. Worthley, V. Fuster, Z. A. Fayad, A. G. Zaman, R. Corti, J. T. Fallon, and J. J. Badimon, "Progression and regression of atherosclerotic lesions," *Circulation*, vol. 105, no. 8, pp. 993–998, 2002.

[53] Z. A. Fayad, V. Fuster, J. T. Fallon, T. Jayasundera, S. G. Worthley, G. Helft, J. G. Aguinaldo, J. J. Badimon, and S. K. Sharma, "Noninvasive in vivo human coronary artery lumen and wall imaging using black-blood magnetic resonance imaging," *Circulation*, vol. 102, no. 5, pp. 506–510, 2000.

[54] Y. He, Z. Zhang, Q. Dai, Y. Zhou, Y. Yang, W. Yu, J. An, L. Jin, R. Jerecic, C. Yuan, and D. Li, "Accuracy of MRI to identify the coronary artery plaque: A comparative study with intravascular ultrasound," *Journal of Magnetic Resonance Imaging*, vol. 35, no. 1, pp. 72–78, 2012.

[55] D. Constantini, "Molecular imaging of atherosclerosis," *Journal of Magnetic Resonance Imaging*, vol. 8, no. 2, 2010.

[56] J. R. Davies, J. H. Rudd, and P. L. Weissberg, "Molecular and metabolic imaging of atherosclerosis," *Journal of Nuclear Medicine*, vol. 45, no. 11, pp. 1898–1907, 2004.

[57] J. Rudd, E. Warburton, T. Fryer, H. Jones, J. Clark, N. Antoun, P. Johnstrm, A. Davenport, P. Kirkpatrick, B. Arch, J. Pickard, and P. Weissberg, "Imaging atherosclerotic plaque inflammation with [18F]-fluorodeoxyglucose positron emission tomography," *Circulation*, vol. 105, no. 23, pp. 2708–2711, 2002.

[58] M. J. Lipton, C. B. Higgins, D. Farmer, and D. P. Boyd, "Cardiac imaging with a high-speed cine-CT scanner: preliminary results." *Radiology*, vol. 152, no. 3, pp. 579–582, 1984.

[59] U. Flohr, T.G.and Schoepf and B. Ohnesorge, "Chasing the heart - new developments for cardiac CT. thorac imaging." *Thorac Imaging*, vol. 22, pp. 4–16, 2007.

[60] P. Sprawls, *Physical principles of medical imaging*. Aspen Publishers, 1993. [Online]. Available: http://books.google.com/books?id=8IRrAAAAMAAJ

[61] J. Bushberg, *The Essential Physics of Medical Imaging*. Lippincott Williams & Wilkins, 2002. [Online]. Available: http://books.google.com/books?id=jTAwGTYYiusC

[62] J. A. Seibert and J. M. Boone, "X-ray imaging physics for nuclear medicine technologists. part 2: X-ray interactions and image formation," *Journal of Nuclear Medicine Technology*, vol. 33, no. 1, pp. 3–18, 2005.

[63] J. Hsieh and S. (Society), *Computed Tomography: Principles, Design, Artifacts, and Recent Advances*, ser. Press Monograph. SPIE, 2009. [Online]. Available: http://books.google.com/books?id=QutQPgAACAAJ

[64] A. C. Kak and M. Slaney, "Principles of computerized tomographic imaging," *Engineering*, vol. 33, no. 1, p. 327, 1988. [Online]. Available: http://www.osti.gov/energycitations/product.biblio.jsp?osti_id=5813672

[65] W. Kalender, *Computed Tomography*. John Wiley & Sons, 2011. [Online]. Available: http://books.google.com/books?id=gfLWmRjoyPMC

[66] P. Sprawls, "Aapm tutorial. CT image detail and noise." *Radiographics*, vol. 12, no. 5, pp. 1041–1046, 1992.

[67] J. F. Barrett and N. Keat, "Artifacts in CT: Recognition and avoidance1," *Radiographics*, vol. 24, no. 6, pp. 1679–1691, 2004.

[68] W. P. Shuman, K. R. Branch, J. M. May, L. M. Mitsumori, D. W. Lockhart, T. J. Dubinsky, B. H. Warren, and J. H. Caldwell, "Prospective versus retrospective ecg gating for 64-detector CT of the coronary arteries: Comparison of image quality and patient radiation dose1," *Radiology*, vol. 248, no. 2, pp. 431–437, August 2008.

[69] L. W. Goldman, "Principles of CT: Multislice CT," *Journal of Nuclear Medicine Technology*, vol. 36, no. 2, pp. 57–68, June 2008.

[70] A. Macovski, R. Alvarez, J.-H. Chan, J. Stonestrom, and L. Zatz, "Energy dependent reconstruction in x-ray computerized tomography," *Computers in Biology and Medicine*, vol. 6, no. 4, pp. 325–336, 1976.

[71] R. E. Alvarez and A. Macovski, "Energy-selective reconstructions in x-ray computerised tomography," *Physics in Medicine and Biology*, vol. 21, no. 5, p. 733, 1976.

[72] D. J. Hawkes, D. F. Jackson, and R. P. Parker, "Tissue analysis by dual-energy computed tomography," *British Journal of Radiology*, vol. 59, no. 702, pp. 537–542, 1986.

[73] G. Di Chiro, R. A. Brooks, R. M. Kessler, G. S. Johnston, A. E. Jones, J. R. Herdt, and W. T. Sheridan, "Tissue signatures with dual-energy computed tomography," *Radiology*, vol. 131, no. 2, pp. 521–523, 1979.

[74] E. Marshall, W.and Hall and R. M. A. C. D. Doost-Hoseini, A.and Alvarez, "An implementation of dual energy CT scanning," *Journal of Computer Assisted Tomography*, vol. 8, pp. 745–749, 1984.

[75] C. E. Cann, G. Gamsu, F. A. Birnberg, and W. R. Webb, "Quantification of calcium in solitary pulmonary nodules using single- and dual-energy ct." *Radiology*, vol. 145, no. 2, pp. 493–496, 1982. [Online]. Available: http://www.ncbi.nlm.nih.gov/pubmed/7134457

[76] H. Goldberg, C. Cann, A. Moss, M. Ohto, A. Brito, and M. Federle, "Noninvasive quantification of liver iron in dogs with hemochromatosis using dual-energy CT scanning," *Investigative Radiology*, vol. 17, pp. 375–380, 1982.

[77] E. L. Nickoloff, F. Feldman, and J. V. Atherton, "Bone mineral assessment: new dual-energy CT approach." *Radiology*, vol. 168, no. 1, pp. 223–228, 1988.

[78] C. E. Cann, "Quantitative CT for determination of bone mineral density: a review." *Radiology*, vol. 166, no. 2, pp. 509–522, 1988.

[79] T. Flohr, C. McCollough, H. Bruder, M. Petersilka, K. Gruber, C. Suess, M. Grasruck, K. Stierstorfer, B. Krauss, R. Raupach, A. Primak, A. Kttner, S. Achenbach, C. Becker, A. Kopp, and B. Ohnesorge, "First performance evaluation of a dual-source CT (DSCT) system," *European Radiology*, vol. 16, pp. 256–268, 2006.

[80] Y. Zou and M. D. Silver, "Analysis of fast kVp-switching in dual energy CT using a pre-reconstruction decomposition technique," *Proceedings of SPIE*, vol. 6913, Apr 2008.

[81] X. Wu, D. A. Langan, D. Xu, T. M. Benson, J. D. Pack, A. M. Schmitz, E. J. Tkaczyk, J. Leverentz, and P. Licato, "Monochromatic CT image representation via fast switching dual kVp," *Proceedings of SPIE*, vol. 7258, Feb 2009.

[82] D. Xu, D. A. Langan, X. Wu, J. D. Pack, T. M. Benson, J. E. Tkaczky, and A. M. Schmitz, "Dual energy CT via fast kVp switching spectrum estimation," *Proceedings of SPIE*, vol. 7258, Feb 2009.

[83] V. Raptopoulos, A. Karellas, J. Bernstein, F. R. Reale, C. Constantinou, and J. K. Zawacki, "Noninvasive quantification of liver iron in dogs with hemochromatosis using dual-energy CT scanning," *American Journal of Roentgenology*, vol. 157, no. 4, pp. 721–5, 1991.

[84] E. Robinson, J. Babb, H. Chandarana, and M. Macari, "Dual source dual energy MDCT: comparison of 80 kvp and weighted average 120 kvp data for conspicuity of hypo-vascular liver metastases." *Investigative Radiology*, vol. 45, no. 7, pp. 413–418, 2010.

[85] C. Thomas, O. Patschan, D. Ketelsen, I. Tsiflikas, A. Reimann, H. Brodoefel, M. Buchgeister, U. Nagele, A. Stenzl, C. Claussen, A. Kopp, M. Heuschmid, and H.-P. Schlemmer, "Dual-energy CT for the characterization of urinary calculi: In vitro and in vivo evaluation of a low-dose scanning protocol," *European Radiology*, vol. 19, pp. 1553–1559, 2009.

[86] N. Takahashi, R. P. Hartman, T. J. Vrtiska, A. Kawashima, A. N. Primak, O. P. Dzyubak, J. N. Mandrekar, J. G. Fletcher, and C. H. McCollough, "Dual-energy CT iodine-subtraction virtual unenhanced technique to detect urinary stones in an iodine-filled collecting system: A phantom study," *American Journal of Roentgenology*, vol. 190, no. 5, pp. 1169–1173, 2008. [Online]. Available: http://www.ajronline.org/content/190/5/1169.abstract

[87] D. T. Boll, N. A. Patil, E. K. Paulson, E. M. Merkle, W. N. Simmons, S. A. Pierre, and G. M. Preminger, "Renal stone assessment with dual-energy multidetector CT and advanced postprocessing techniques: Improved characterization of renal stone compositionpilot study1," *Radiology*, vol. 250, no. 3, pp. 813–820, March 2009.

[88] C. Fink, T. R. Johnson, H. J. Michaely, D. Morhard, C. Becker, M. Reiser, and K. Nikolaou, "Dual-energy CT angiography of the lung in patients with suspected pulmonary embolism: initial results." *RoFo Fortschritte auf dem Gebiete der Rontgenstrahlen und der Nuklearmedizin*, vol. 180, no. 10, pp. 879–883, 2008.

[89] R. Krissak, T. Henzler, M. Reichert, B. Krauss, and C. Schoenberg, Stefan. O.and Fink, "Enhanced visualization of lung vessels for diagnosis of pulmonary embolism using dual energy CT angiography," *Investigative Radiology*, vol. 45, pp. 341–346, 2010.

[90] E. J. Chae, J.-W. Song, J. B. Seo, B. Krauss, Y. M. Jang, and K.-S. Song, "Clinical utility of dual-energy CT in the evaluation of solitary pulmonary nodules: Initial experience1," *Radiology*, vol. 249, no. 2, pp. 671–681, November 2008.

[91] B. Ruzsics, H. Lee, P. Zwerner, M. Gebregziabher, P. Costello, and U. Schoepf, "Dual-energy CT of the heart for diagnosing coronary artery stenosis and myocardial ischemia-initial experience," *European Radiology*, vol. 18, pp. 2414–2424, 2008.

[92] B. Ruzsics, F. Schwarz, U. J. Schoepf, Y. S. Lee, G. Bastarrika, S. A. Chiaramida, P. Costello, and P. L. Zwerner, "Comparison of dual-energy computed tomography of the heart with single photon emission computed tomography for assessment of coronary artery stenosis and of the myocardial blood supply," *The American Journal of Cardiology*, vol. 104, no. 3, pp. 318–326, 2009.

[93] Y. Tanami, E. Ikeda, M. Jinzaki, K. Satoh, Y. Nishiwaki, M. Yamada, Y. Okada, and S. Kuribayashi, "Computed tomographic attenuation value of coronary atherosclerotic plaques with different tube voltage: an ex vivo study." *Journal of Computed Assisted Tomography.*, vol. 34, pp. 58–63, 2010.

[94] B. C. Meyer, T. Werncke, W. Hopfenmller, H. J. Raatschen, K.-J. Wolf, and T. Albrecht, "Dual energy CT of peripheral arteries: effect of automatic bone and plaque removal on image quality and grading of stenoses." *European Journal of Radiology*, vol. 68, no. 3, pp. 414–422, 2008.

[95] P. Stolzmann, T. Frauenfelder, T. Pfammatter, N. Peter, H. Scheffel, M. Lachat, B. Schmidt, B. Marincek, H. Alkadhi, and T. Schertler, "Endoleaks after endovascular abdominal aortic aneurysm repair: Detection with dual-energy dual-source CT," *Radiology*, vol. 249, no. 2, pp. 682–691, November 2008.

[96] M. Karcaaltincaba and A. Aktas, "Dual-energy CT revisited with multidetector CT: review of principles and clinical applications." *Diagnostic and interventional radiology Ankara Turkey*, vol. 17, no. 3, pp. 181–194, 2011. [Online]. Available: http://www.ncbi.nlm.nih.gov/pubmed/20945292

[97] K. K. Park, "A new approach for the enhancement of dual-energy computed tomography images," *PhD Thesis - Arizona State University*, 2011.

[98] L. Ritschl, F. Bergner, C. Fleischmann, and M. Kachelrie, "Water calibration for CT scanners with tube voltage modulation," *Physics in Medicine and Biology*, vol. 55, no. 14, p. 4107, 2010.

[99] X. Wu, D. A. Langan, D. Xu, T. M. Benson, J. D. Pack, A. M. Schmitz, E. J. Tkaczyk, J. Leverentz, and P. Licato, "Monochromatic CT image representation via fast switching dual kvp," *Proceedings of SPIE*, vol. 7258, Feb 2009.

[100] L. A. Lehmann, R. E. Alvarez, A. Macovski, W. R. Brody, N. J. Pelc, S. J. Riederer, and A. L. Hall, "Generalized image combinations in dual KVP digital radiography." *Medical physics*, vol. 8, no. 5, pp. 659–667, 1981.

[101] D. J. Walter, "Accuracy and precision of dual energy CT imaging for the quantification of tissue fat content," *Proceedings of SPIE*, vol. 6142, pp. 61 421G–61 421G–12, 2006.

[102] T. Hastie, R. Tibshirani, and J. Friedman, *The Elements of Statistical Learning: Data Mining, Inference, and Prediction*, corrected ed., 2009.

[103] L. Breiman, "Random forests," *Machine Learning*, vol. 45, pp. 5–32, 2001.

[104] A. Schmermund, S. Mohlenkamp, and R. Erbel, "Coronary artery calcium and its relationship to coronary artery disease," *Cardiol Clin*, vol. 21, pp. 521–534, 2003.

[105] J. A. Rumberger, D. B. Simons, L. A. Fitzpatrick, P. F. Sheedy, and R. S. Schwartz, "Coronary artery calcium area by electron-beam computed tomography and coronary atherosclerotic plaque area: A histopathologic correlative study," *Circulation*, vol. 92, no. 8, pp. 2157–2162, 1995.

[106] T. Flohr and B. Ohnesorge, "Imaging of the heart with computed tomography," *Basic Research in Cardiology*, vol. 103, pp. 161–173, 2008.

[107] T. Gerber, B. Kantor, and E. Williamson, *Computed Tomography of the Cardiovascular System*. Informa Healthcare, 2007.

[108] A. S. Agatston, W. R. Janowitz, F. J. Hildner, N. R. Zusmer, M. V. Jr., and R. Detrano, "Quantification of coronary artery calcium using ultrafast computed tomography," *Journal of the American College of Cardiology*, vol. 15, no. 4, pp. 827–832, 1990. [Online]. Available: http://www.sciencedirect.com/science/article/pii/073510979090282T

[109] S. Ulzheimer and W. Kalender, "Assessment of calcium scoring performance in cardiac computed tomography," *European Radiology*, vol. 13, pp. 484–497, 2003. [Online]. Available: http://dx.doi.org/10.1007/s00330-002-1746-y

[110] M. Ferencik, A. Ferullo, S. Achenbach, S. Abbara, R. C. Chan, S. L. Booth, T. J. Brady, and U. Hoffmann, "Coronary calcium quantification using various calibration phantoms and scoring thresholds." *Invest Radiol*, vol. 38, no. 9, pp. 559–66, 2003.

[111] C. Hong, T. K. Pilgram, F. Zhu, and K. T. Bae, "Is coronary artery calcium mass related to agatston score?1," *Academic Radiology*, vol. 11, no. 3, pp. 286–292, 2004.

[112] W. Pavlicek, P. Panse, A. Hara, T. Boltz, R. Paden, D. Yamak, P. Licato, N. Chandra, D. Okerlund, S. Dutta, R. Bhotika, and D. Langan, "Initial use of fast switched dual energy CT for coronary artery disease," *Proceedings of SPIE*, vol. 7622, March 2010.

[113] C. A. Clavijo and N. J. Pelc, "Image-quality optimization for dual energy computed tomography (DECT) three-material decomposition," *Revista Ingenieria Bimedica*, vol. 3, no. 5, pp. 33–42, 2009.

[114] R. Virmani, F. D. Kolodgie, A. P. Burke, A. Farb, and S. M. Schwartz, "Lessons from sudden coronary death: a comprehensive morphological classification scheme for atherosclerotic lesions," *Arteriosclerosis, Thrombosis, and Vascular Biology*, vol. 20, no. 5, pp. 1262–1275, 2000.

[115] R. Virmani, A. P. Burke, A. Farb, and F. D. Kolodgie, "Pathology of the unstable plaque." *Prog Cardiovasc Dis*, vol. 44, no. 5, pp. 349–56, 2002.

[116] H. Boltz, W. Pavlicek, R. Paden, M. Renno, A. Jensen, and M. Akay, "An anthropomorphic beating heart phantom for cardiac x-ray CT imaging evaluation," *Journal of Applied Clinical Medical Physics*, vol. 11, no. 1, 2010.

[117] A. Liaw and M. Wiener, "Classification and regression by randomforest," *R News*, vol. 2, no. 3, pp. 18–22, 2002. [Online]. Available: http://CRAN.R-project.org/doc/Rnews/

[118] R. Taguchi, J. Takasu, Y. Itani, R. Yamamoto, K. Yokoyama, S. Watanabe, and Y. Masuda, "Pericardial fat accumulation in men as a risk factor for coronary artery disease," *Atherosclerosis*, vol. 157, no. 1, pp. 203–209, 2001. [Online]. Available: http://www.sciencedirect.com/science/article/pii/S0021915000007097

[119] M. Kalinin, D. Raicu, J. Furst, and D. Channin, "A classification approach for anatomical regions segmentation," in *Image Processing, 2005. ICIP 2005. IEEE International Conference on*, vol. 2, sept. 2005, pp. II–1262–5.

[120] M. Gletsos, S. Mougiakakou, G. Matsopoulos, K. Nikita, A. Nikita, and D. Kelekis, "A computer-aided diagnostic system to characterize CT focal liver lesions: design and optimization of a neural network classifier," *Information Technology in Biomedicine, IEEE Transactions on*, vol. 7, no. 3, pp. 153–162, sept. 2003.

[121] R. M. Haralick, K. Shanmugam, and I. Dinstein, "Textural features for image classification," *Systems, Man and Cybernetics, IEEE Transactions on*, vol. SMC-3, no. 6, pp. 610–621, nov. 1973.

[122] L. Yu and H. Liu, "Feature selection for high-dimensional data: A fast correlation-based filter solution," 2003, pp. 856–863.

[123] I. H. Witten, E. Frank, L. Trigg, M. Hall, G. Holmes, and S. J. Cunningham, "Weka: Practical machine learning tools and techniques with java implementations," 1999.

[124] Y. Yang, "Image segmentation and shapte analysis of blood vessels with applications to coronary atheroslerosis coronary atherosclerosis," *PhD Thesis - Georgia Institute of Technology*, 2007.

APPENDIX A

PATIENT IMAGES

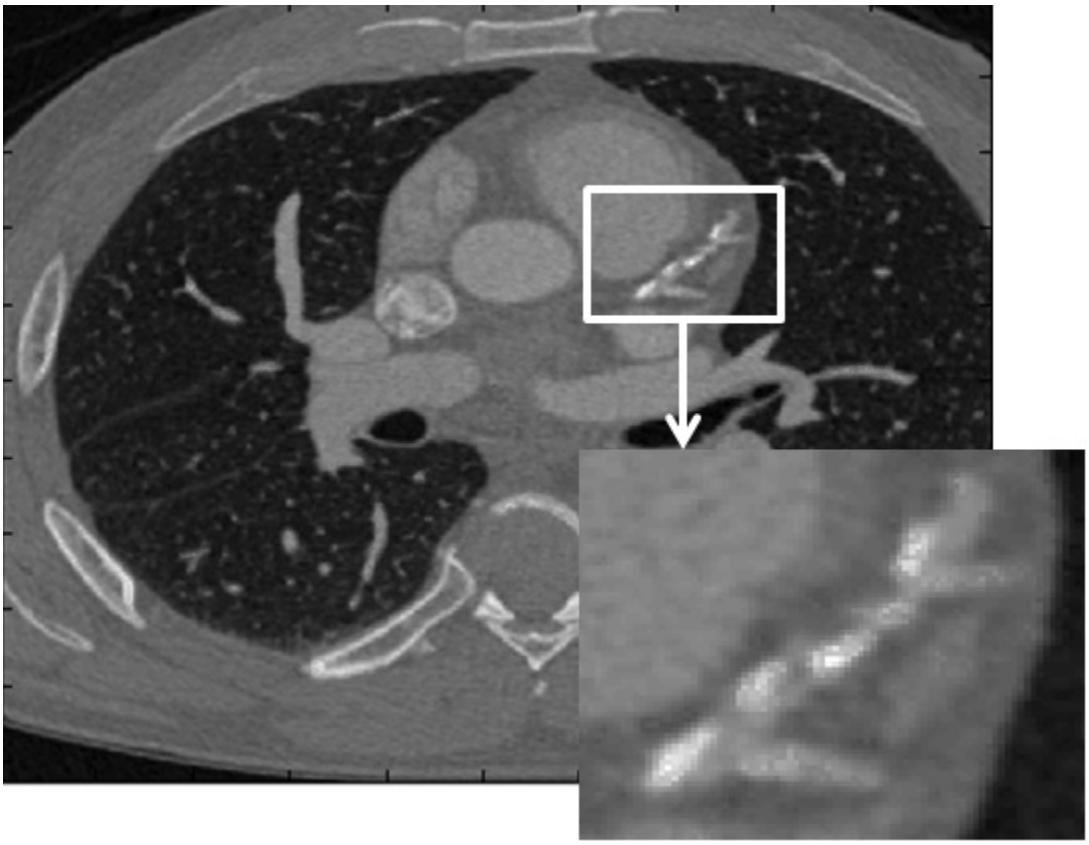

Figure 37. The monochromatic 70keV image of P1 with its enlarged image of LAD. P=Patient, the numbers coming after P represents the patient ID.

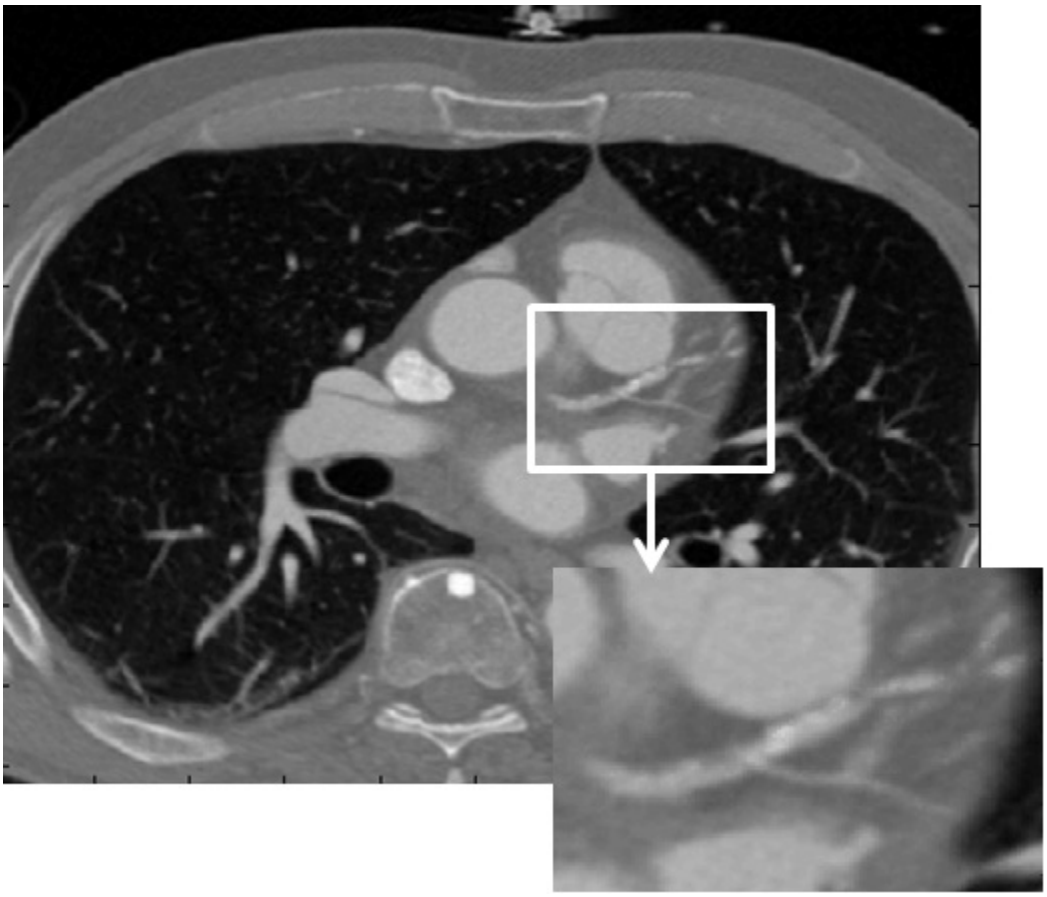

Figure 38. The monochromatic 70keV image of P2 / IM1 with its enlarged image of LAD. P=Patient, IM=Image, the numbers coming after P and IM represents the patient and image ID.

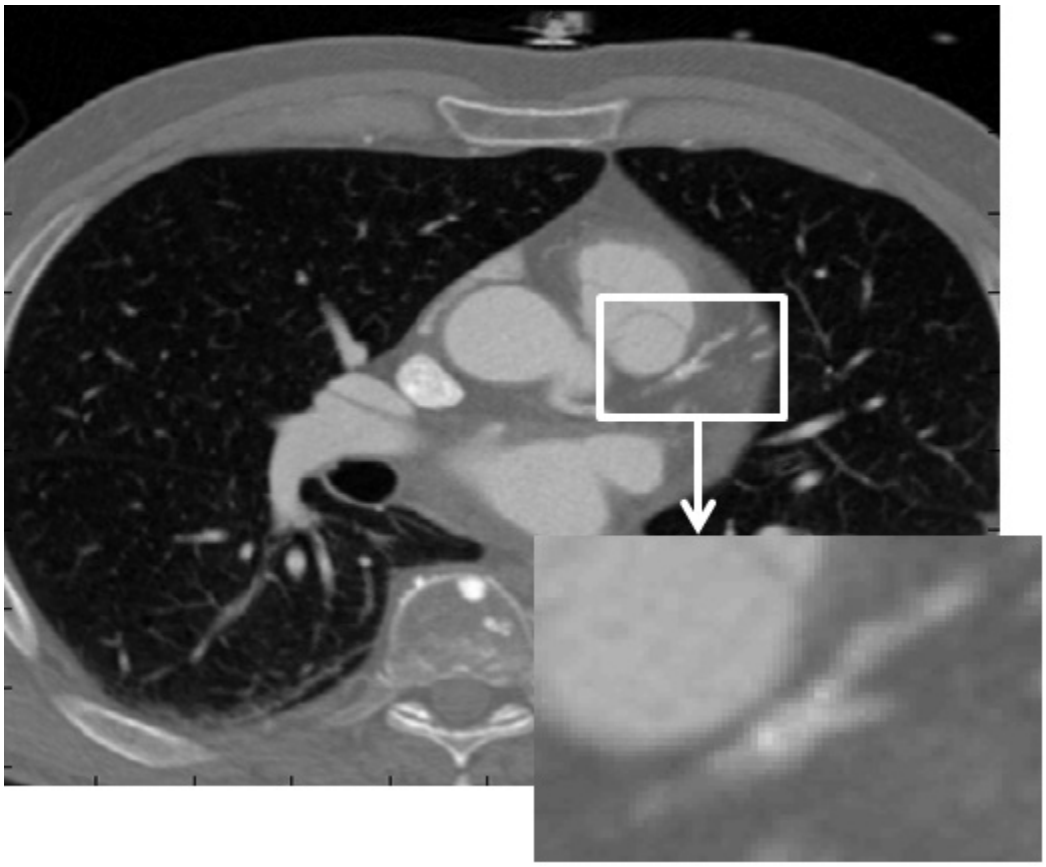

Figure 39. The monochromatic 70keV image of P2 / IM2 with its enlarged image of LAD. P=Patient, IM=Image, the numbers coming after P and IM represents the patient and image ID.

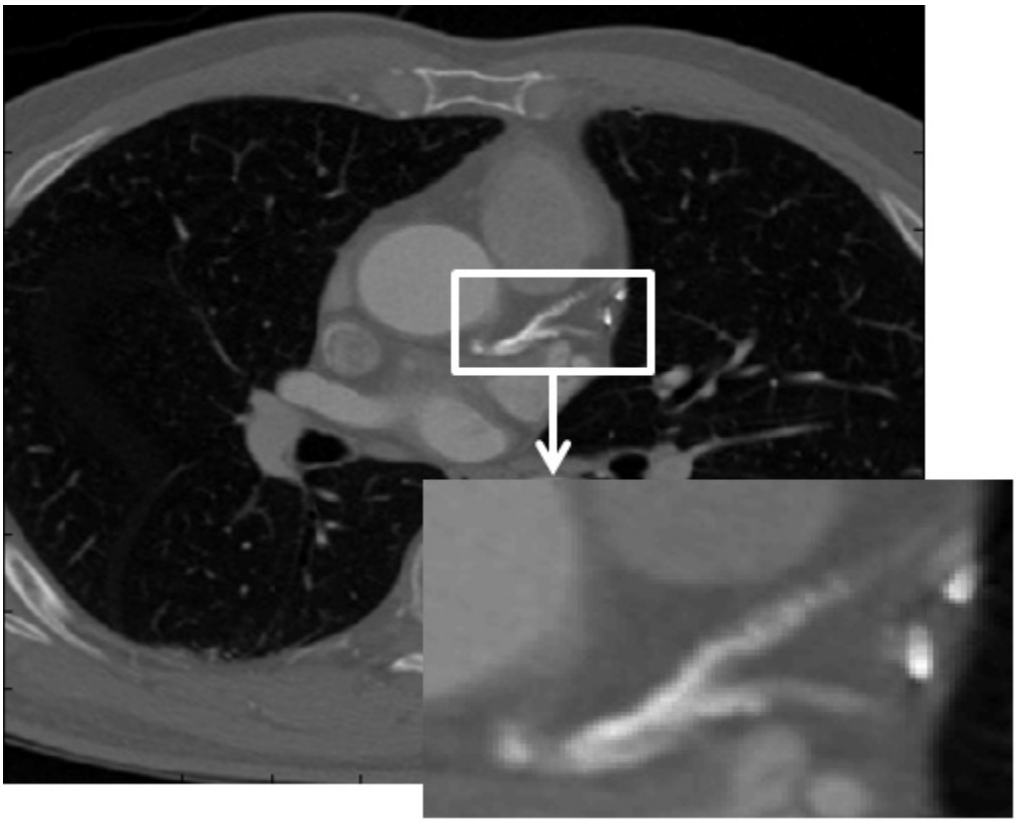

Figure 40. The monochromatic 70keV image of P3 / IM1 with its enlarged image of LAD. P=Patient, IM=Image, the numbers coming after P and IM represents the patient and image ID.

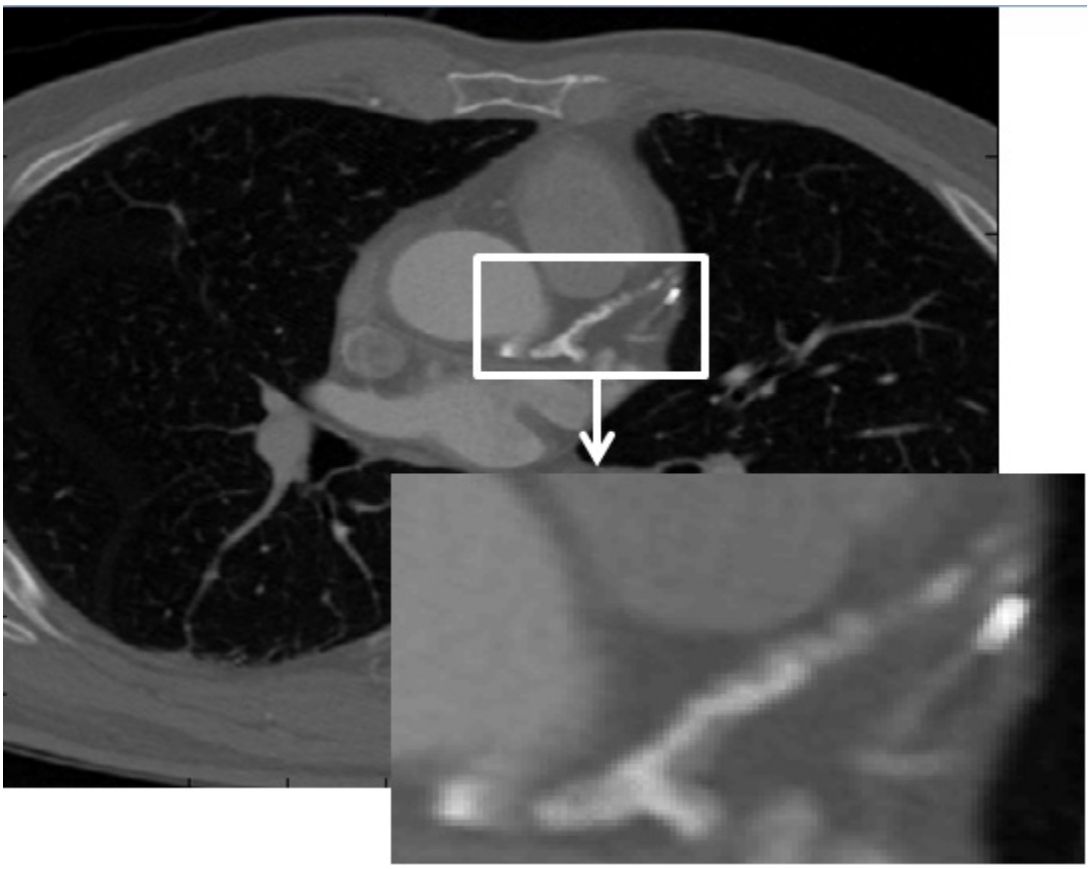

Figure 41. The monochromatic 70keV image of P3 / IM2 with its enlarged image of LAD. P=Patient, IM=Image, the numbers coming after P and IM represents the patient and image ID.